UQAC
Université du Québec
à Chicoutimi

A THESIS SUBMITTED IN PARTIAL FULFILMENT OF

THE REQUIREMENTS FOR THE DEGREE

OF

DOCTOR OF PHYLOSOPHY

IN ELECTRICAL ENGINEERING

By

FANGHUI YIN

Modeling and Experimental Investigation of the Effects of Electric Field and Corona Discharge on Ice Accreted on High-Voltage Conductors

Modélisation et étude expérimentale des effets du champ électrique et des décharges de couronne sur l'accumulation de glace sur les conducteurs haute tension

Québec, Canada

December, 2016

ABSTRACT

Atmospheric icing affects a wide variety of man-made structures in many countries. It is generally well known to occur in countries like Japan, Canada, Iceland, Russia as well as China. When the power transmission lines are subject to icing, huge corona loss due to corona discharge or rupture of transmission lines may be caused because of the ice load. In the worst-case scenario, it would lead to power outage and collapse of tower.

The objective of this study is to investigate the effects of electric field and corona discharge on ice accreted on high-voltage conductor. The research was approached by two methods, experiments and simulations. To achieve this objective, experiments were carried out by means of a corona cage in a climate room at CIGELE laboratories, University of Quebec in Chicoutimi (UQAC) and the simulations were performed by a finite element software. Rime and glaze were considered in the present study as they are thought to be the most adverse conditions for power transmission lines.

The experimental results showed that the electric field has a significant influence on ice formation. Under both rime and glaze ice conditions, the weight of ice accreted on the surface of the conductor increased with electric field strength up to 20 kV_{rms}/cm and then decreased as it is increased further. Without voltage applied on the conductor, about half of the total weight of glaze ice can be contributed by the icicle accretion. In the presence of electric field, the weight percentage of icicles could be lowered to 14%. When the water film was freezed right after they reached the bottom of the conductor, the icicle spacing was independent of electric field. If developed water pedants were formed before they were freezed, the icicle spacing decreased with an increase of electric field. Due to the repulsion force of the pendant drops at the icicle tip, the presence of electric field can result in an angle between adjacent icicles accreted on the conductor. This angle increased with an increase of conductor surface electric field.

The corona loss was mainly contributed by the fundamental component. The contribution of other harmonic components on corona loss can be neglected, except for the harmonic component which was already significant in the applied voltage. The power factor of the 3rd harmonics can be used to determine whether the

conductor is running below or above its corona onset voltage. If it was close to 0.5, the conductor was running near its corona onset voltage. If it was higher than 0.5, it can be expected that the conductor was operated beyond its corona onset voltage. According to the simulated results, it was found that when the electric field is no higher than 20 kV_{rms}/cm, the ice accretion model works well. However, with the electric field increased further, the results diverged because of the generation of corona wind.

RÉSUMÉ

Le givrage atmosphérique affecte un éventail de structures dans beaucoup de pays, tels que le Japon, le Canada, l'Islande, la Russie et également la Chine. Les lignes de transport de l'énergie électrique soumises aux accumulations de glace peuvent subir d'importantes pertes d'énergie à la suite de décharges couronne ou de rupture des conducteurs. Dans le pire des cas, ceci peut dégénérer en coupures de courant et dans l'effondrement de pylônes.

L'objectif poursuivi par ce travail est l'étude des effets du champ électrique et des décharges couronne sur la glace accumulée sur les conducteurs à haute tension. Deux approches ont été utilisées dans cette recherche : l'approche expérimentale et la simulation numérique. Pour atteindre cet objectif, des expériences pratiques ont été effectuées en utilisant une configuration cylindrique montée dans une chambre climatique aux laboratoires de la CIGELE à l'université du Québec à Chicoutimi (UQAC). Quant aux simulations numériques, elles ont été réalisées par la méthode des éléments finis. Le givre lourd et le verglas ont été utilisés dans cette étude, car ces types de glace sont considérés comme les plus dangereuses pour les lignes de transport d'énergie électrique.

Les résultats expérimentaux ont montré que le champ électrique a un effet significatif sur la formation de la glace. Dans des conditions de givre ou de verglas, le poids de la glace accumulée à la surface du conducteur augmente avec l'intensité du champ électrique jusqu'à 20 kV_{rms}/cm, pour ensuite diminuer si cette intensité augmente davantage. En l'absence de tension appliquée au conducteur, environ la moitié du poids total de verglas est attribuable à l'accumulation de glaçons. En présence d'un champ électrique, le pourcentage en poids des glaçons peut diminuer jusqu'à 14%. Lorsque le film d'eau gèle immédiatement après avoir atteint la surface inférieure du conducteur, l'espacement entre les glaçons devient indépendant du champ électrique. À cause de la force de répulsion des gouttes d'eau en suspension au bout des glaçons, la présence d'un champ électrique peut résulter en la formation d'un angle entre les glaçons adjacents accumulés sur le conducteur. Cet angle augmente avec l'accroissement du champ électrique à la surface du conducteur.

La perte en énergie due à l'effet couronne provient principalement de la composante fondamentale. La contribution des autres composantes harmoniques sur la perte couronne est négligeable, sauf pour la composante harmonique, qui était déjà significative dans la tension appliquée. Le facteur de puissance relatif à la 3^{e} harmonique peut être utilisé pour déterminer si le conducteur est alimenté par une tension électrique plus basse ou plus élevé que la tension de seuil de l'effet couronne. Si le facteur de puissance est de 0.5, le conducteur est sous une tension près de la tension de seuil de l'effet couronne. S'il est supérieur à 0.5, on peut supposer que la conducteur est alimenté par une tension plus élevé que la tension de seuil de l'effet couronne. En se basant sur les résultats de la simulation, il a été observé que lorsque le champ électrique à surface du conducteur ne dépasse pas 20 kV_{rms}/cm, le modèle d'accumulation de glace fonctionne adéquatement. Toutefois, si le champ électrique augmente davantage, les résultats divergent à cause de la génération de vent électrique.

TABLE OF CONTENTS

LIST OF SYMBOLS

SYMBOL	CONCETP	DIMENSIONS
a	Droplet radius	m
C_d	Drag Coefficient	
C_g	Geometric capacitance	F
C_n	Non-linear capacitance	F
C_{sc}	Stokes-Cunningham slip correction factor	
CL	Corona loss	W/m
D	Diameter of the conductor	m
e	Eccentricity	
E_c	Corona onset gradient	kV/cm
$E_{surface}$	Conductor surface gradient	
f	Frequency	Hz
F_d	Drag	N
F_{DEP}	Dielectrophoretic force	N
G_c	Leakage conductance	S
h	Heat transfer coefficient	$W/(m^2 \cdot K)$
i	current	A
I_P	Phase current	A
m	Conductor surface roughness	
p	Dipole moment	$(C \cdot m)$
P	Power per meter	W/m
P_{RL}	Power of resistive loss	W
r_c	Conductor radius	m
r_{sc}	Sub-conductor radius	m
R	Radius of the outer cylinder	m
R_P	Phase resistance	Ω

R_e	Reynolds number	
SD	Standard deviation	
THD	Total harmonic distortion	
u	Votlage	V
v	Velocity	m/s
V	Voltage	V
V_o	Corona onset votlage	V
w	Liquid water content	g/m^3

Greek Symbols

ε	Dielectric constant	F/m
δ	Relative air density	
σ_{20}	Water conductivity	$\mu S/cm$
γ	Surface tension	N/m
η	Fluid viscosity	$Pa{\cdot}s$
ρ	Density	kg/m^3
τ	Relaxation time	s
φ	Bent angle of icicles	
Φ	Angle between adjacent icicles	
σ	Charge density	C/m^2
λ	Mean free path	m
β	Local collision efficiency	

LIST OF TABLES

LIST OF FIGURES

ACKNOWLEDGMENTS

This work was carried out within the framework of the NSERC/Hydro-UQAC Industrial Chair on Atmospheric Icing of Power Network Equipment (CIGELE), the Canada Research Chair on Atmospheric Icing Engineering of Power Networks (INGIVRE) at Université du Québec à Chicoutimi (UQAC), and also in collaboration with the National Basic Research Program of China (973 Program: 2009CB724501/502/503).

I would like to express my deepest gratitude and admiration to my supervisor, Prof. Masoud Farzaneh, for granting me the invaluable chance to pursue my Ph. D study, his supervision, encouragement, support, and especially patience during the entire research. Without his patience and continuous help, this research would not have been possible.

I want to deliver my sincere gratitude and respect to my co-supervisor Prof. Xingliang Jiang, for not only his guidance, valuable advices, but also human qualities and supports.

Special thanks go to Prof. William. A. Chisholm from Kinectrics for his insightful comments and constructive suggestions during my doctoral examination process. Many thanks also go to Prof. Issouf Fofana, Prof. Gelareh Momen, and Prof. Shamsodin Taheri for their constructive criticism which contributed to improve the quality of this thesis.

I would like to extend my thanks to Claude Damours, Pierre Camirand, and Xavier Bouchard at CIGELE Laboratory for their technical support and to Denis Masson for his help with administrative tasks.

Finally, I would like to take this opportunity to thank my son, Mingzhe Yin, for his unconditional love during these years.

CHAPTER 1

INTRODUCTION

CHAPITRE 1

INTRODUCTION

1.1 Definition of the problem

The study of ice and snow accretion on structures is of great interest to engineers and scientists. In cold regions, atmospheric icing affects a wide variety of man-made structures in many countries [1][2], including overhead transmission lines, telecommunication towers, and wind turbines. These structures are installed across mountains, making ice events more likely to happen.

Wet snow accretion, as reported by Colbeck et al [3], is known to be particularly troublesome since a large mass accumulation can occur in only a few hours. Snow accretion on overhead transmission lines and wires may thus be considered as a serious problem posing tremendous threats to existing power installations. As extra-high voltage (EHV, in the range of 230 kV and 800 kV [4]) and ultra-high voltage (UHV, referring to above ± 800 kV for DC and 1000 kV for AC [5]) power transmission lines are running not far away from their disruptive critical voltages, in unfavorable icing conditions, it can be expected that these lines will operate for considerable periods in the presence of corona discharges [6]. The existence of corona discharge can cause audible noise (AN), radio frequency interference (RFI), and corona loss (CL) which should be minimized for economic reasons [7][8]. In addition to corona losses induced by ice accretion, subsequent ice shedding tends to cause power outages and severe damage to power network structures, thereby leading to many serviceability, safety, and mechanical reliability issues. Many countries such as Canada, the United States, the United Kingdom, France, Germany, Norway, Iceland, and Japan experience wet snowfalls which affect the related overhead transmission networks.

The damage caused by a single wet snowstorm can necessitate the expenditure of sums on the order of 100 million dollars. Past records show that the occurrence of wet snow accretion is relatively more common and may be equally as catastrophic in Japan, Canada, United Kingdom, Iceland, Russia

and China every year. Two records of these ice storms were most destructive. One is the North American Ice Storm of 1998 which was a massive combination of five smaller successive ice storms which combined to strike a relatively narrow swath of land from eastern Ontario to southern Quebec to Nova Scotia in Canada, and bordering areas from northern New York to central Maine in the United States, in January 1998 [9]. It caused massive damage to trees and electrical infrastructure all over the area, leading to widespread long-term power outages. As a result, over 4 million people in Ontario, Quebec and New Brunswick were deprived of power. More than 1,000 power transmission towers were destroyed and 30,000 utility poles fell for an estimated loss of $5.4 billion dollars [6]. The other one is the 2008 Chinese Ice Storm, which struck the most populated and economically developed region of China and was even more damaging than the 1998 North American Ice Storm. There were 13 provincial grids (approximately 43% of the total power at the provincial level) affected, and the users of nearly 570 counties were subject to power outages. According to statistics released by the Ministry of Civil Affairs of China, the ice storm led to 107 deaths and the direct economic losses alone were about $22 billion and the indirect losses could be even greater [10].

Corona loss is one of the most important issues associated with EHV and UHV power transmission systems [11-13]. This problem is of great significance in Canada [14], especially in Quebec, Newfoundland, etc. which have as many as 80 snowy days a year with an annual average snowfall more than 300 centimeters based on weather data collected from 1981 to 2010. The influence of ice accretion on corona discharge has been investigated since the beginning of high voltage transmission. Initially, losses of energy were of primary interest and, as early as 1912, F. W. Peek stated that the effect of snow was greater than that of any other weather condition [15]. After that, many attempts were made to find some quantitative relations atmospheric conditions and corona losses. However, most of them were carried out on test lines and operating lines, with the atmospheric condition varying. In the present study, the corona investigation was performed in a climate room, with all ambient parameters constant during the tests.

Presently, there are mainly three methods to investigate the CL on the conductor, namely the corona cage [16-18], outdoor test lines [11, 19-20] and operating lines [21-24]. However, in the last two cases, the losses measured are composed of several components such as insulator loss, CL from conductor surface and some loss in the earth. It is very difficult to separate these losses from one another.

Ice accumulation coupled with the wind-on-ice load may lead to the failure of structures and their function. Typical outcomes are endangering for human life in aircraft or marine icing incidents, and in the loss of industrial resources due to faults on an overhead transmission line grid system. Regarding the latter, structural damage can be extensive, running up to millions of dollars and, moreover, the effects of power outages are known to be severe in both human and industrial terms. Thus, much progress has been made in understanding the physical process involved during ice accretion on structures. Three main methods of investigation are the following ones [2]:

1) Continuous field measurement of ice load and wind-on-ice load, allied with the simultaneous measurements of meteorological variables;

2) Simulations using icing wind tunnels for un-energized icing or corona cage for energized icing;

3) Construction of mathematical/computational icing models.

From the viewpoint of engineering design, the generation of an ice load database, with corresponding historical weather database, is of major importance. Furthermore, such databases are essential in the validation of experimental and theoretical simulations of the icing process. Obviously, this approach involves high cost in the installation of measurement sites, for a geographical location, and in the manning of such sites by icing engineers and meteorologists. The study of ice simulation employing an icing wind tunnel or corona cage has the advantage that the effects of changes in the flow and thermal conditions on the accretion process can be readily assessed and analyzed. A disadvantage

of this method is that due to the many physical and meteorological variables and the flow and thermal parameters controlling an accretion process, it is difficult to achieve a one-to-one correspondence between the icing wind tunnel/corona cage and field conditions. The third method involving theoretical models, based on the known physics of the accretion process, has obvious advantages especially when implemented in the form of mathematical models. In this project, an attempt will be made to develop the theory of ice accretion in a systematic way, based on principles of fluid mechanics, mass transfer, and electric field using mathematical and numerical techniques.

1.2 Research objectives

The main goal of this research work is to investigate the effect of electric field strength and corona discharge on ice accreted on high-voltage conductor. To achieve this aim, the research is approached by two methods, experiments and simulations. The specific objectives of this research are listed as follows.

1.2.1 Experiments

- Investigating the effect of electric field strength on ice formation. Due to the Joule heat, the ice appearance will be affected by the existence of electric field. Moreover, as ice load is an important factor when designing the power transmission line, ice weight, icicle spacing, icicle length, and angle between adjacent icicles should also be investigated.

- Investigating the effect of electric field strength on corona characteristics under icing conditions. To get detailed information about the influence of electric field on corona characteristics, the corona loss, corona onset voltage, harmonic distortion, leakage conductance, and capacitance of an energized conductor under icing conditions should be studied.

1.2.2 Simulations

- Developing an applicable time-dependent numerical ice model for simulating the rime accretion process on fixed conductors under energized conditions. Many simulation models of ice accretion have been developed. However, all of these models deal with un-energized conditions. In reality, the transmission lines exposed to icing are subjected to electric field. Therefore, to investigate the ice accretion on transmission lines, it is appropriate to improve the existing numerical model by considering the influence of electric field.

- Establishing a numerical technique for model application. Icing is a very complex phenomenon for which an analytical solution is not available. Also, the governing equations for modeling its behavior are non-linear and not easy to solve. Therefore, developing a technique which can deal with the non-linear equations is crucial.

- Validating the simulation results with the experimental data. A good measurement of the reliability of the model would be a good agreement of its predicted results with the experimental data. For this reason, the developed model and the numerical results obtained from it should be validated by experimental data.

1.3 Methodology

To achieve the above objectives, experiments and simulations were carried out at CIGELE laboratories, University of Quebec in Chicoutimi (UQAC). The methodologies for them are described as follows:

1) Experiments

- As icing is a very complex process and its formation can be greatly influenced by the variation of environmental parameters, it is very important that the weather parameters are kept constant during the whole ice accretion process. Thus, the experiments were performed in a delicate climate room which is designed especially for atmospheric research. To apply an electric field on the conductor, a corona cage was adopted. One major advantage of using a corona cage is that the close distance between the tested conductor and grounded meshed cylinder can replicate the surface electric field of a practical transmission line at a much lower applied voltage. With careful control, the measurements carried out in the CIGELE climate room were found to be repeatable.

2) Simulations

For simplicity, simulation will be carried out on a smooth conductor. Numerical modeling of atmospheric ice accretion is based on the following steps:

- Airflow computation. As the wind velocity investigated in this paper is less than Mach 0.3, the airflow can be assumed to be incompressible.
- Droplet trajectory calculation. The trajectory of water droplets will be modeled based on the balance between aerodynamic force, gravity, buoyancy force and dielectrophoretic force.
- Local collision efficiency. After the water droplet trajectory is calculated, the local collision efficiency can be obtained.
- Updating the ice layer. With the local collision efficiency known, the mass accreted in each section on the surface of the ice conductor can be computed. In each iteration, the ice layer is updated.

1.4 Statement of the originality of the thesis

To the best of our knowledge, no systematic study has been done on the influence of electric field strength on corona discharge of ice accreted conductor. Also, previous ice accretion simulations were only focused on the conductor without high-voltage applied, in which the corona electric force were not considered. The main original contributions of this PhD project are summarized as follows:

1) The effect of electric field strength on ice formation was investigated.

2) A detailed analysis of electric field strength on corona characteristics was carried out.

3) A time-dependent numerical ice accretion simulation including the effect of electric field strength was developed.

1.5 Thesis outline

The structure of this dissertation is as follows:

Chapter 1 introduces the problem of ice accretion on power network, the necessity, research objectives, methodology, and originality of the present research.

Chapter 2 reviews the literature related to corona loss measurement. Moreover, a survey of numerical modelling for predicting the ice accretion is introduced.

Chapter 3 describes the experimental facilities and the test procedures for performing the experiments in the laboratory.

Chapter 4 presents the influence of electric field strength on ice formation. Laboratory results show that electric field strength has significant influence on ice appearance, ice weight, icicle spacing, icicle length, and also angle between adjacent icicles.

Chapter 5 focuses on the dynamic corona characteristics of an energized conductor during the ice accretion process.

Chapter 6 deals with the rime accretion simulation and its experimental validation in laboratory.

Chapter 7 provides general conclusions derived from the results and discussion covered in the previous chapters. Several recommendations for the future work are also presented.

CHAPTER 2

REVIEW OF LITERATURE

CHAPITRE 2

REVIEW OF LITERATURE

2.1 Types of atmospheric icing accretion

Atmospheric icing is a generic term for all types of accretion of frozen water substance [1] [25]. Various processes where water in various forms in the atmosphere freezes and adheres to objects exposed to the air. In general, the atmospheric icing accretion can be classified in the following types.

(1) Precipitation icing

(2) In-cloud icing

(3) Hoar frost

2.1.1 Precipitation icing

Precipitation icing occurs in several forms such as freezing rain (glaze or rime), wet snow and dry snow depending on how the precipitation is influenced by variations in temperature near the ground and up to a few hundred meters above ground. Such icing is experienced any place where precipitation, in combination with freezing temperatures, occurs. Different types of precipitation icing are described below:

Glaze: Glaze has a density higher than 900 kg/m^3 [26]. Glaze grows in a clear, smooth structure with no air bubbles, as shown in Figure 2-1. It is usually formed from freezing precipitation, rain or drizzle, or from clouds with large liquid water content and large drop size. The freezing rate of droplets is less than the impingement rate, which causes part of the drop to splash or flow around the conductor

before freezing. While glaze contains no air bubbles as such, in strong wind situations it grows in irregular shapes incorporating pockets of air.

Figure 2-1: Glaze on a conductor in the experiment

Figure 2-2: Soft rime on a conductor in the experiment

Rime: Rime has a density of 300 - 900 kg/m^3[27]. It is usually classified as soft rime or hard rime:

Soft rime has a density of less than 600 kg/m^3. Figure 2-2 shows soft rime on a conductor in the experiments. It is a white ice deposition that forms when the water droplets in light freezing fog or mist freeze to the outer surfaces of objects, with calm or light wind. The fog freezes usually to the windward

side of tree branches, wires, or any other solid objects. Soft rime is similar in appearance to hoar frost; but whereas rime is formed by vapor first condensing to liquid droplets (of fog, mist or cloud) and then attaching to a surface, hoar frost is formed by direct deposition from water vapor to solid ice. Soft rime grows in a triangular or pennant shape pointed into the wind. The granular structure results from the rate of freezing of individual drops, each drop freezing completely before another one impinges on the surface. They are fragile and can be easily shaken off objects. Factors that favor soft rime are small drop size, slow accretion of liquid water, high degree of super-cooling, and fast dissipation of latent heat of fusion.

Hard rime has a density ranging from 600 to 900 kg/m^3 and tends to grow in a layered structure with clear ice mixed with ice containing air bubbles [28]. In this case the freezing rate of the droplets is equal to the impingement rate. It is a white ice that forms when the water droplets in fog freeze to the outer surfaces of objects. It is often seen on trees at mountains and ridges in winter, when low hanging clouds cause freezing fog. This fog freezes to the windward (wind-facing) side of tree branches, buildings, or any other solid objects, usually with high wind velocities and air temperatures between -2 and -8 °C (28.4 and 17.6 °F). Hard rime formations are difficult to shake off; they have a comb-like appearance, unlike soft rime, which looks feathery or spiky, or clear ice, which looks homogeneous and transparent. Figure 2-3 shows hard rime accreted on a conductor.

Figure 2-3: Hard rime on a conductor in the experiment

Both rime types are less dense than glaze and cling less tenaciously, therefore damage due to rime is generally minor compared to glaze.

Wet snow: Wet snow has a density of 300 - 800 kg/m^3. It is usually defined as snow which falls at temperatures equal to or above -5 ℃. Under these conditions, the snow is sticky enough to adhere to surfaces easily and accumulate rapidly. Wet snow tends to build on tops and windward surfaces of structures and in cylindrical layers around conductors [1]. At temperatures below about -2 ℃, snow particles are usually too dry to adhere to surfaces in appreciable quantities. If the temperature falls below 0 ℃ after the accretion of wet snow, the accumulation freezes into a dense hard layer with strong adhesion. Transmission line problems have occurred due to wet snow events.

Dry snow: Dry snow accretes at subfreezing temperatures [29-30]. This type of accretion appears only when wind speed is very low i.e. below 2 m/s. The density of dry snow is, in general, very low, not exceeding 100 kg/m^3. Hence the accreted masses are, in most cases, much lower than the loads the power lines are designed for.

2.1.2 In-cloud icing

In-cloud icing occurs only within clouds consisting of super-cooled droplets, which are droplets that remain liquid at a temperature below 0 ℃ [31]. It is a process by which super-cooled water droplets in a cloud or fog freeze immediately upon impact on objects in the airflow, i.e. overhead lines in mountains above the cloud base. For the structures situated at mountain summits, exposure to super-cooled clouds or fog usually results in soft rime (300 - 600 kg/m^3), however, precipitations resulting in hard rime (600 - 900 kg/m^3) also occur and are most frequent in early winter. Sometimes very large in-cloud icing occurs on overhead lines.

2.1.3 Hoar frost

Hoar frost: Hoar frost has a density of less than 300 kg/m^3. Figure 2-4 shows hoar frost that grows on pine needle tips [32]. Hoar frost is generally a deposit of interlocking ice crystals formed by direct sublimation of water vapor in the air onto objects. It forms when air with a dew point below freezing is brought to saturation by cooling. Hoar frost is featherlike in appearance and builds occasionally to large diameters with very little weight. Normally, hoar frost does not constitute a significant loading problem, however, it is a very good collector of super-cooled fog or cloud droplets and at subfreezing temperatures with light winds, fog conditions gradually become soft rime of significant volume and weight. Furthermore, its presence on the overhead transmission lines can still cause very significant energy losses due to corona discharge [33].

Figure 2-4: Surface hoar plates on pine needle tips

Of all the above-mentioned types of ice accretion, rime and glaze are most dangerous to the power system. Therefore, the present paper deals only with rime and glaze ice accretion.

2.2 Corona loss

2.2.1 Electric power system

Modern electric power systems are the result of over a hundred years of development in which the technical and economic feasibility of transmitting large blocks of power over long distances played an important role [34]. The first public power station was put into service in 1882 in London (Holborn). Soon a number of other public supplies for electricity followed in other developed countries. By 1890, the art in the development of an AC generator and transformer had been perfected to the point when AC supply was becoming common, displacing the earlier DC system. The first major AC power station was commissioned in 1890 at Deptford, supplying power to central London over a distance of 28 miles at 10 kV. Prior to this, electric power was generated and used locally in either a laboratory or industrial setting. Thomos Edison is generally regarded as the one sowing the seeds of modern power system by conceiving the Pearl Street station in New York [35], in which the generator was used to supply a number of his newly-invented incandescent lamps.

An important problem facing the early power systems was the efficiency of power distribution using metallic wires, usually copper, over distances of even a few kilometers [36]. In fact, the occurrence of heavy power losses in the resistance of the distribution wires at low voltages made these systems uneconomical, as the need for larger quantities of power and longer distances increased. For given quantity of power, the use of a higher transmission voltage results in a lower current in the conductors and therefore in lower power losses and higher efficiency.

High voltage transmission gave rise, not only the economic feasibility of transmitting large blocks of power over long distances, but also resulted in the development of large power networks in which geographically separated generating stations and load centers are interconnected [37]. Improved economy and reliability were the main factors pushing the evolution of large interconnected power system.

The rapidly increasing transmission voltage level in recent decades is a result of the growing demand for electrical energy, coupled with the development of large hydroelectric power stations at sites far remote from centres of industrial activity and the need to transmit the energy over long distances to the centres. Figure 2-5 lists some of the major AC transmission systems in chronological order of their installations [34].

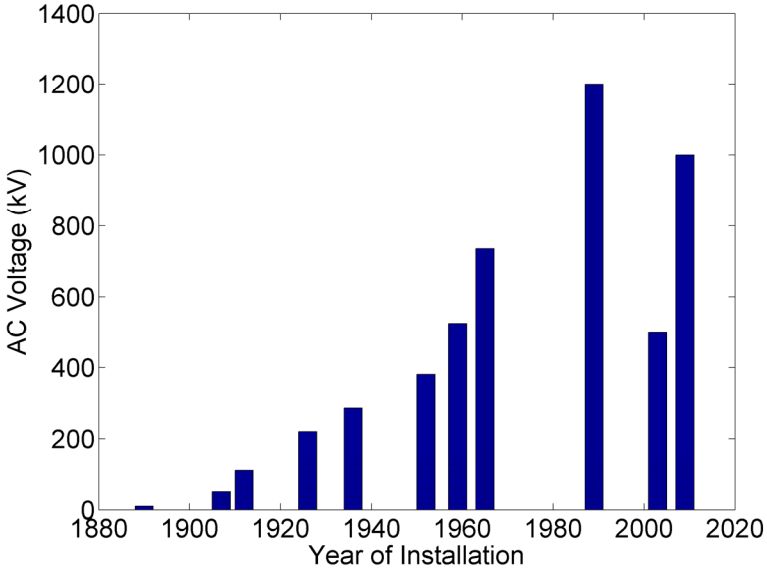

1 1890 10 kV Deptford
2 1907 50 kV Stadtwerke München
3 1912 110 kV Lauchhammer − Riesa
4 1926 220 kV N. Pennsylvania
5 1936 287 kV Boulder Dam
6 1952 380 kV Harspränget − Hallsberg
7 1959 525 kV USSR
8 1965 735 kV Manicouagan – Montreal
9 1989 1200 kV Soviet Union
10 2003 500 kV Three Gorges (China)
11 2009 1000 kV Jindongnan-Nanyang-Jingmen (China)

Figure 2-5: Major AC systems in chronological order of their installations.

Corona losses upon transmission lines may reach values worthy of serious consideration of the designing and operating electrical engineer at or above potentials of 100 kV between wires [38], depending upon the size and spacing of wires, the weather conditions and the elevation of the line above sea level. Power loss due to corona atmospheric icing is very complicated and occurs in a variety of forms as a result of the interplay of numerous physical processes.

2.2.2 Conductor corona onset gradient

Atmospheric air is probably the most important insulating material used on high voltage transmission lines [39-40]. At sufficient high levels of conductor surface electric fields, complex ionization processes take place in the air surrounding high voltage transmission line conductors, resulting in discharge phenomena known as corona.

Onset voltage is defined as the initiation of a self-sustaining discharge near the conductor, and occurs when the conductor surface electric field strength exceeds a critical value [41-42]. The corona onset gradient is a function of the conductor diameter and its surface condition as well as of the ambient temperature and pressure [39] [43-47]. The corona onset gradient of cylindrical conductors has been studied experimental and empirical formulas have been developed for alternating and direct applied voltages. In general, the corona onset gradient E_c of a cylindrical conductor is given as [48]

$$E_c = mE_0\delta(1+\frac{K}{\sqrt{\delta r_c}}) \tag{2.1}$$

where E_0 and K are empirical constants depending on the nature of the applied voltage, δ is the relative air density factor. These values for AC, according to Peek, are $E_0 = 21.1$ kV_{rms}/cm and $K = 0.308$ for the case of concentric cylindrical geometry.

The empirical formula described above was derived from laboratory experiments on smooth conductors with diameters much smaller than those used on practical transmission lines. The diameter of the out cylinder was also small in these laboratory studies. However, it was found that this formula can be extrapolated to practical conductor sizes.

Conductor surface irregularity factor m is equal to 1 for ideally smooth and clean conductors [49]. Even microscopic imperfections on the conductor surface tend to reduce the value of m below 1 [50]. Practical transmission line conductors are generally of stranded construction, comprised of several layers of small diameter cylindrical strands. Experimental results have shown that the value of m may

vary between 0.75 and 0.85 for stranded conductors, depending on the ratio of strand to conductor diameter. Under the rain and icing conditions, the value of *m* may be reduced by the water drops, icing treeing, and icicles.

2.2.3 Conductor corona loss predication

The corona performance of a transmission line, as defined by the resulting effects such as corona loss (CL), radio interference (RI), and Audible noise (AN) [6], depends mainly on two sets of factors: a) line design; b) ambient weather conditions [39-40]. The line design factors of interest are the type and dimensions of the conductor, phase spacing in the case of AC lines and pole spacing for DC lines, and the height above ground of the conductors. The most important factor that influences the generation of corona, however, is the electric field distribution in the vicinity of the conductor surface [38]. The second set of factors, namely the ambient weather conditions, influence the corona performance in two ways: first, the temperature, pressure, and relative humidity of the ambient air affect the basic ionization processes involved in corona discharge; and second, any precipitation such as rain or snow deposited on the conductor surface distorts the electric field in the vicinity.

The design of transmission lines for acceptable corona performance generally results in the conductors or conductor bundles operating at conductor surface electric field strengths that are close to their corona onset gradient under normal fair weather conditions [51-52]. As a result of normal design considerations, the occurrence of corona discharges, at the nominal operating voltage and in fair weather, are limited. Under foul weather conditions, such as rain or icing, there is an intensive corona discharge, nearly uniform distributed, along the conductor [6].

Corona losses under heavy rain or icing conditions of practical transmission lines may reach the same order of magnitude as the I^2R loss at full load on the line. In fair weather, corona loss are generally two or three orders of magnitude lower than those under heavy rain or glaze ice conditions. Under other weather conditions, such as fog, light rain, or snow, corona losses are somewhat lower than

those under heavy rain or glaze ice conditions, but much higher compared to fair weather losses [16] [15][22-23][53-54]. From a practical point of view, therefore, the corona loss under fair weather are negligible.

Form the point of view of transmission line design, the most useful corona loss parameter is the mean annual corona P_{ma}, which can be defined as [55]

$$P_{ma} = \frac{1}{T_a} \sum_{i=1}^{n} P_i T_i \tag{2.2}$$

where i ranges from 1 to N is the different weather categories for which the corona loss P_i is known, T_i is the time duration in hours of the i^{th} weather category in a year, and $T_a = 8760$, is the total number of hours in a year.

To determine p_{ma} for a transmission line located in a given region, two sets of information should be given:

1) The generated corona loss for the actual conductor used, as a function of the conductor surface electric field strength under different categories of weather conditions.

2) The annual weather patterns occurring in the region where the line is located.

The first can be obtained through tests on the conductor or from empirical formulas and the second may be got from the nearby meteorological station.

Corona loss formulae were initiated by F.W. Peek Jr. in 1912 derived empirically from most difficult and painstaking experimental work [54]. Since then, a number of formulae have been derived by others, both from experiments and theoretical analysis [47] [56-58].

In 1961, Nigol put forward a corona loss equation for single and bundled conductors. The basic form is express as [20]

$$P = Kfr^2 \frac{\Delta\rho}{2\pi} E_e^2 \ln \frac{E_e}{E_0} \tag{2.3}$$

where P is the corona loss per conductor, in kW/mile, K is a dimensionless conditional constant for the given weather and conductor surface conditions, f is the frequency, r is the radius of the conductor, E_e is the effective surface electric field strength, in kV_{rms}/cm, E_0 is the critical surface electric field strength for given weather and conductor surface conditions, in kV_{rms}/cm, and $\Delta\rho$ is the angular portion of conductor surface in corona, in radians. For a single conductor at normal phase spacings, the value E_e is almost constant over the conductor surface and is equal to the maximum surface electric field strength E_m. Because of this, corona on single conductor is assumed to cover the entire surface, and the angle $\Delta\rho$ is equal to 2π. Therefore, the above equation for single conductor becomes

$$P = Kfr^2 E_e^2 \ln \frac{E_e}{E_0} \tag{2.4}$$

For bundled conductors with non-uniform surface electric field strength, both the effective surface electric field strength and the portion of conductor surface in corona must be evaluated before the corona loss can be calculated.

Extending over the yeas 1967 and 1968, Clade carried out more than 20, 000 measurements using a corona cage [53]. The measured values were reduced to normalized values and then been plotted into a universal chart. After that, the corona loss on UHV lines under rain can be predicated with conductor surface state coefficients.

2.3 Measurement methods for corona performance

Theoretical considerations are necessary to provide a basic understanding of corona phenomena occurring on transmission line conductors and of the resulting corona effects [38]. However, the very complex nature of corona phenomena, combined with the large number of factors influencing corona

effects, making experimental studies essential for evaluating the corona performance of transmission lines. Good experimental data is a basic requirement for the development of accurate empirical and semi-empirical methods of calculation. The choice of instrumentation and measurement techniques, for the various parameters defining corona performance of a transmission line, plays an important role in planning and carrying out the experimental studies [38][59]. Different test methods, ranging from test in laboratory corona cage to measurements on operating transmission lines, may be used for obtaining the necessary data. In the early studies, it is economically impractical to construct long test lines and replace conductors of varying dimensions frequently for corona tests. Usually, the UHV test bases and similar research institutes obtain data from corona tests on short test lines and then convert them to equivalent data for long three-phase lines.

The main objective of experimental corona studies on conductors are: 1) to understand the physical mechanisms involved in corona discharge as well as the resulting corona effects, and 2) to generate experimental data that can be used to develop prediction methods for the corona performance of transmission lines. The principal corona test methods used and the aspects of corona performance that can be studied by each of them are described as follows

2.3.1 Laboratory corona cage

To understand the physics of corona discharges, laboratory studies have been carried out using a variety of electrode geometries, such as point-plane, sphere-plane, concentric-spherical etc. [7][40][61-65]. Most of the laboratory studies of corona on cylindrical conductors have been made, however, using what is commonly known as a "corona cage" configuration. In fact, the empirical formulas for determining corona onset on smooth and stranded conductors were obtained mainly from corona cage tests [48].

A corona cage usually has two layers as shown in Figure 2-6. The out layer is the shielding cage and the inner layer is used for the measurement of corona with a round or square cross-section. During

the test, test conductors are usually placed at the center of a corona cage. Because the conductors are placed near the corona cage, surface fields with strength comparable with those on an UHV transmission line conductor can be produced when a lower test voltage is applied to the conductor [41]. In general, high voltage is applied to the conductor, with the inner cage maintained at zero potential by connecting it to ground through a small measuring impedance. In special cases involving measurement of fast-rising corona current pulses, the situation may be reversed by applying high voltage to the cage and keeping the conductor at ground potential.

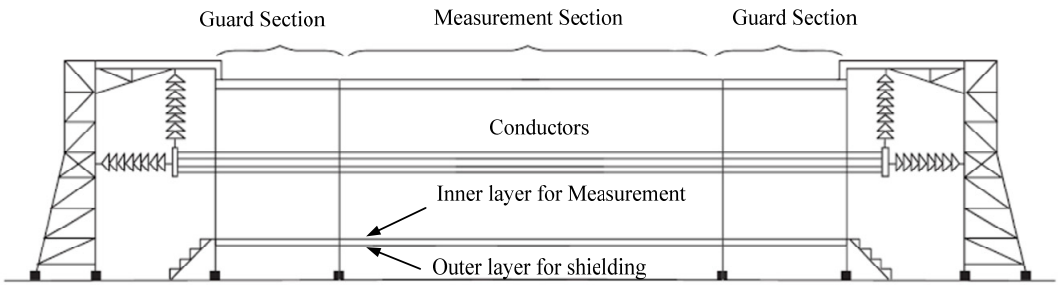

Figure 2-6: Schematic diagram of a corona cage.

For a corona cage of finite length, the electric field distribution in the longitudinal direction is uniform over the central section of the conductor and becomes non-uniform at both ends. By adding guard sections, the central section of the corona cage can be selected to obtain a fairly uniform electric field distribution along the length of the conductor. The central section of the corona cage is then used for the corona measurements by connecting it to ground through appropriate measuring impedance, while the two guard sections are connected directly to ground.

The main advantage of the corona cage test setup is that the conductor surface electric field distribution can be determined quickly and accurately from a knowledge of the voltage applied and the dimension of the test configuration. For round cross-section corona cage, the uniformly distributed conductor surface gradient E_c in kV/cm can be calculated quite accurately as [43]

$$E_{surface} = \frac{U_{app}}{r_c \ln(R/r_c)} \tag{2.5}$$

where U_{app} (kV) is the voltage applied to the conductor, r_c is the conductor radius in cm, and R is the radius of the cage in cm. Different values of the conductor surface electric field strengths are obtained by varying the voltage applied.

Figure 2-7: An indoor corona cage at Tsinghua University.

The main criterion for the design of a corona cage test setup, for use either in a laboratory or outdoors, is to have an adequate margin between the breakdown and corona onset voltages. For the conductor to be tested, the cage diameter should be small enough to obtain corona onset at a sufficiently low voltage [66]. At the mean time, the air gap between the conductor and the cage should be large enough so that the breakdown voltage is higher than the corona onset voltage. Figure 2-7 shows an indoor corona cage at Tsinghua University [67].

2.3.2 Outdoor corona cage

To test conductor configuration generally used on transmission lines, the corona cages have to be much larger than those of laboratory cages, which is the main reason why they are built outdoors. Outdoor corona cages also permit experimental data to be obtained under some natural weather conditions.

Figure 2-8: Outdoor corona cage at Wuhan Bureau of China Electric Power Research Institute.

An outdoor test corona cage arrangement consists essentially of conductor configurations placed at the center of a wire-mesh enclosure of either circular or square cross section [17]. The square cross section is usually preferred because of difficulties in fabricating cylindrical cage enclosures of large diameter. In some cases, the cage enclosure may simply consist of two vertical fences, with the ground acting as the lower panel and the top left open. As in the case of laboratory cages, outdoor corona cages are often built with an insulated central measuring section and two guard end sections. Outdoor cages have frequently been used mainly to determine the corona performance under heavy rain conditions, by equipping them with means for producing artificial rain, or at different altitudes [68-70]. Figure 2-8 shows an outdoor corona cage developed by Wuhan bureau of China Electric Power Research

Institute. It has the following features: (a) it incorporates a hybrid electronic current transformer that allows the safe and reliable measurement of the current through conductors in the corona cage; (b) by using an outdoor high-accuracy capacitive voltage divider, it is possible to accurately measure the voltage; and (c) the voltage signals are transmitted through coaxial cable and the current signals are transmitted through optical fiber. Based on the accurate voltage and current signals extracted, the system can measure the corona loss of conductors with the aid of the digital signal processing and virtual instrumentation technologies.

Figure 2-9: Outdoor corona cage at UHV DC Testing Site in Beijing.

In regions where snow accumulation on the ground in winter may be a problem. It is necessary to place the cage enclosure at a certain height above ground. If the cage length is more than about ten meters, the cage enclosure is made to follow the catenary shape of the conductor, so that the conductor is located at the center of the cage all along its length. Figure 2-9 shows the outdoor corona cage at UHV DC Testing Site in Beijing with a catenary shape, used for single pole and dual pole tests with maximum testing voltage up to ±1200kV [71]. It is the biggest outdoor cage so far, with a dimension of 70 m× 22m × 15 m (L×W×H).

2.3.3 Outdoor test lines

Although outdoor test cages provide a comparatively rapid and inexpensive means for evaluating the corona performance of conductor configurations, mainly in heavy rain, they cannot be used to obtain the all-weather statistical corona performance. Such statistical data in fair weather as well as foul weather can be obtained only from outdoor lines.

Figure 2-10: Outdoor test line at UHV AC test base of China Electric Power Research Institute.

Outdoor test lines are essentially short sections of full-scale transmission lines [19]. For AC corona studies, either single-phase or three-phase test lines may be used. Three phase test lines accurately reproduce the electric field conditions of normal transmission lines [60]. For this reason, most of the corona studies for the purpose of providing design data for transmission lines at new higher voltage level have been carried out on three-phase test lines [11][13][38][60]. In 1963, Laforest presented the corona loss and radio noise investigation from a EHV project at a heavily instrumented lest line with 4.3 miles of under fair and foul weather. Insulator loss and the dependence of corona loss on load current were also discussed [72]. Figure 2-10 shows an outdoor test line at UHV AC test base of China Electric Power Research Institute, used for AC corona studies with 8 towers and a length of 1084 m [73]. Corona loss tests were carried out at UHV AC test line under light, moderate, and heavy rain. The results show that

when it starts to rain, the corona loss increases rapidly. After the rain stops, the corona loss gradually decreases with the drying of conductors. Its attenuation time depends on the field strength on the conductor surface, wind speed, and air humidity. The corona loss increases with increasing rainfall intensity and is similar to a saturation curve. When the rainfall intensity is low, the corona loss increases rapidly with increasing rainfall intensity. As the rainfall intensity increases further, the corona loss increases at a reduced rate. When the rainfall intensity increases to a certain level, the corona loss will gradually become saturated.

2.3.4 Operating lines

Corona performance measured on operating AC transmission lines are very useful for developing methods to predict and check the validity of empirical methods. Svenska Kraftnät, the Swedish National Transmission System Operator, developed a corona losses supervision in the load dispatching system [74]. The supervision is used during foul weather conditions to decrease corona losses by a reduction of voltage level. The measurement of CL, however, is possible mainly in the corona cage and on test lines and is difficult on operating lines. On the operating lines carrying normal load, the joule losses in the conductor due to the load current are generally so high that it is difficult to get an accurate estimate of corona losses from measurement. Some measurements have been made on an unload transmission line. However, the interpretation of these measurements is difficult since the line, across long distance, may be subjected to different weather conditions along its length [23] [75-76].

2.4 Development of numerical modelling for ice accretion

Atmospheric icing is very complicated and occurs in a variety of forms as a result of the interplay of numerous physical processes [77]. Meteorological variables play a key role in determining the amount and type of ice accretion, especially the air temperature, wind speed and hydrometeor phase, morphology, mass flux and size distribution. The Ice Storm of 1998 illustrates the limitations of relying on direct icing measurements for determining ice loads for structural design. The Ice Storm caused

unexpected damage in the only region of the world where regular icing measurements have been made for a long time using a dense observation network [78].

The limited value of icing measurements arises from the rarity of icing events and their complex dependence on combinations of atmospheric and geographical factors. Consequently, icing events occur sporadically and they are highly variable in space. They may not follow a probability distribution that is readily derivable from measured icing data. Moreover, such data do not exist at all in many areas of the world. Furthermore, for tall structures, ice data is required high above the ground, and such data cannot usually be collected until the structure has been erected. Then it may be too late, as illustrated by frequent power line failures and the 140 ice-induced distribution tower collapses during the last 40 years in the United States alone [79].

As Ice accretion is one of class of problems known to applied mathematicians as “moving interface problems” [80]. One of the challenges presented by these problems is how to deal with the time-dependence imposed by the changing geometry of the growing interface. Currently, numerous publications about icing phenomenon can be found in the literature and certain studies may be as back as the 1940s [25]. Since then, the phenomenon has been subjected to extensive investigation prompted by the requirements of engineering practices in a number of northern countries [81-91]. These studies were made with the aim of compiling ice-load and wind-on-ice load databases in order to understand the various complex forms of wet-snow and ice accretion, to develop and to confirm the validity of icing models, and to introduce probabilistic design load approaches [2].

Numerical study of atmospheric ice accretion on structures includes the computation of mass flux of icing particles as well as determination of the icing conditions as in Jones's model and Makkonen's model [82][84][88]. This can be numerically simulated by means of integrated thermo-fluid dynamic models. For all of them, the goal was to predict bulk ice accretion properties such as ice load. They did not consider details of the icing process. On a cylindrical object, the icing intensity I, i.e., the

rate of increase in the mass of ice divided by the part of the surface area of the ice deposit that faces the wind ($g \cdot cm^{-2} \cdot h^{-1}$) can be calculated by [84]

$$I = \frac{2}{\pi} Envw \tag{2.6}$$

where E is the collection efficiency, namely the ratio of the mass flow of the impinging water droplets to the mass flow that would be captured by the surface if the water droplets were not deflected by the air stream, n is the freezing fraction, i.e., the ratio of the icing intensity to the mass flow of the impinging water droplets, v is the wind speed and w the liquid water content in the air. The values of I, E, and n in the equation are the overall values for the accreted object. In this simplified model, the ice was assumed to keep a circular form during the whole ice accretion process.

Others were more focused on ice shape prediction so as to estimate the dynamic wind-on-ice loads together with static ice loads [86] [89] [90]. More importance was assigned to the ice shape prediction, since it is easy to estimate the ice-load from the predicted ice shape simply by integrating the product of ice density and the area of any element over ice accretion. Also, knowing the ice shape makes it possible to investigate the dynamic force exerted on iced objects and in the case of cable icing, it is possible to obtain the overall loads sustained by its supports by means of carrying out integration along its span. New models were developed which endeavored to account for the physical details of the icing process. These models required personal computers for their implementation. Nevertheless, numerous assumptions and simplifications were still made to keep the computational problem tractable. Unlike Makkonen's model which assumed that the accretion was symmetrically distributed about the cylinder as indicated by (2.6), Oleskiwand developed a fully time-dependent model [89]. However, this model was strictly valid only for rime ice accretion and under de-energized condition.

With the advent of ever increasing computational power, some new numerical models are put forward which are by far the most complete in terms of accounting for the physical processes of icing. Others adopt a radically different approach to icing simulation. Although all of these models are fundamentally similar to the models by Lozowski and Makkonen [84][89], they endeavored to represent physical processes explicitly, their physical verisimilitude and computational procedures have generally

been substantially enhanced. A number of the models are three-dimensional and time-dependent, in the sense of accounting for the feedback between the growing ice accretion and the multi-phase flow around it. Ping Fu developed a simulation of time-dependent ice accretion model on cylindrical objects but two-dimensional [25]. Aliaga developed a three-dimensional simulation and removes the quasi-steady approximation by coupling the air and droplet flow with the icing model in an unsteady manner [90]. Typically, these models use modern CFD methods to solve for the airflow, and either Lagrangian or Eulerian techniques to solve for the local collision efficiency. Ping Fu computed a potential airflow, with separation, using the boundary element method, and couples it with an integral boundary layer model, to determine the heat transfer distribution over the ice accretion. To avoid the great complexity brought by electrical phenomena, then influence of electric field was disregarded in the model.

As the laboratory results shown by Farzaneh [92-94], the electric field has a great influence on ice shape, weight and morphology and that electrical phenomena and related processes such as polarization, ice treeing, ionic wind, droplet charging, electronic and ion bombardments of ice were identified as the main factors influencing the icing process. Since transmission lines are subjected to high electric field, it is practical to further improve the ice accretion model by taking into account the influence of electric field.

2.5 Conclusion

This chapter has introduced types of atmospheric icing accretion, including precipitation icing, in-cloud icing, and hoar frost. The evolution of high voltage transmission was introduced and also the factors that may influence the corona loss. Four methods to measure the corona loss are introduced, especially the indoor corona cage. At last, the development of numerical models for ice accretion is described.

CHAPTER 3

EXPERIMENTAL FACILITIES AND TEST PROCEDURES

CHAPTER 3

EXPERIMENTAL FACILITIES AND TEST PROCEDURES

3.1 Experimental facilities

3.1.1 Climate room

Figure 3-1: Climate room with corona cage

The experimental investigations were carried out in an 8.3m×5.8m×3.85m (length×width×height) climate room which was specially designed for this study, as shown in Figure 3-1. The climate room consisted of a cooling system, water spraying system, and wind controlling system. The high voltage was supplied through a 700 kVA/350 kV transformer with a short-circuit impedance of 4.2%. The cooling system can regulate the air temperature in the climate room down to -30 ℃ by a proportional integral and differential system (PID) with a precision of ± 0.2 ℃. In Figure 3-2, a system of oscillating nozzles was mounted on a pressure-fed water spraying system to produce the spray. Each oscillating nozzle consisted of an air and fluid caps as displayed in Figure 3-3. Water and air flows were channeled to the fluid cap under pressure and then mixed internally in the nozzles to produce a completely atomized spray. Two kinds of fluid caps were used in the experiments to produce different

sizes of water droplets for rime, glaze ice or rain. The climate room was equipped with a wind generator system. The wind generated by the fan pass through a diffusing honeycomb screen to yield a uniform wind velocity ranging from 0 to 10 m/s.

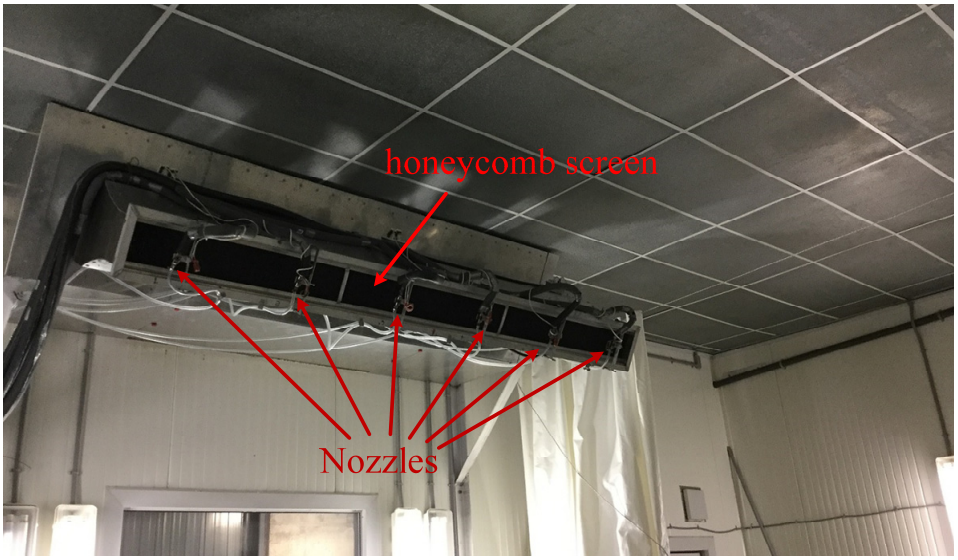

Figure 3-2: Spraying system

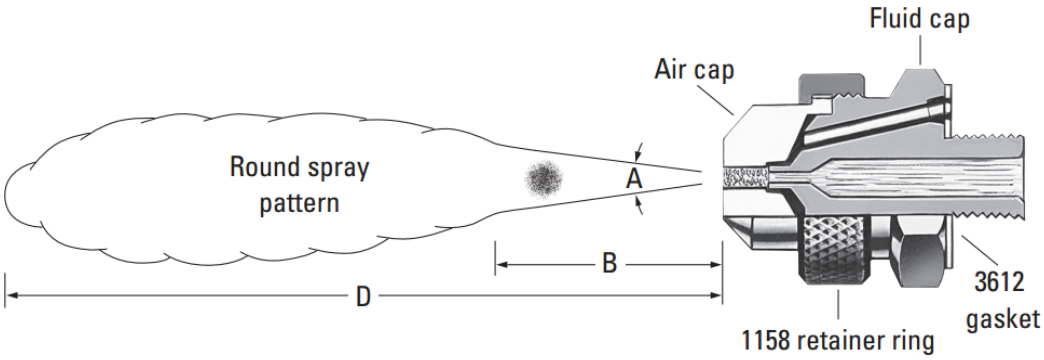

Figure 3-3: Schematic diagram of spray nozzle for ice accretion.

3.1.2 Corona cage

The schematic diagram of test circuit is displayed in Figure 3-4. A smooth aluminum tube with a diameter of 32 mm was placed concentrically inside another metallic mesh cylinder which had a diameter of 1 m. The aluminum tube was supported and fixed by two post insulators. For an indoor

corona cage of finite length, the surface electric field of the test conductor is uniform over the central section but becomes non-uniform at both ends. If guard sections had not been used at both ends of the cage, the cage length would have needed to be at least three to five times longer to obtain a uniform surface field distribution along the central section of the conductor. As the dimensions of the climate room was limited, two guard sections, each with a length of 0.3 m, were added at both ends to reduce the necessary cage length. The central measurement section in Figure 3-4 had a length of 2 m. As the measurement section was used for corona measurement, it was insulated with the guard sections. The measurement section was grounded through a non-inductive shunt resistance R_s (10 Ω) which was in series with the corona cage while the two guard sections were connected directly to ground. As the electric field at the right end of the bare conductor was very high even with low applied voltage, a corona sphere was mounted there to prevent corona discharge at that end.

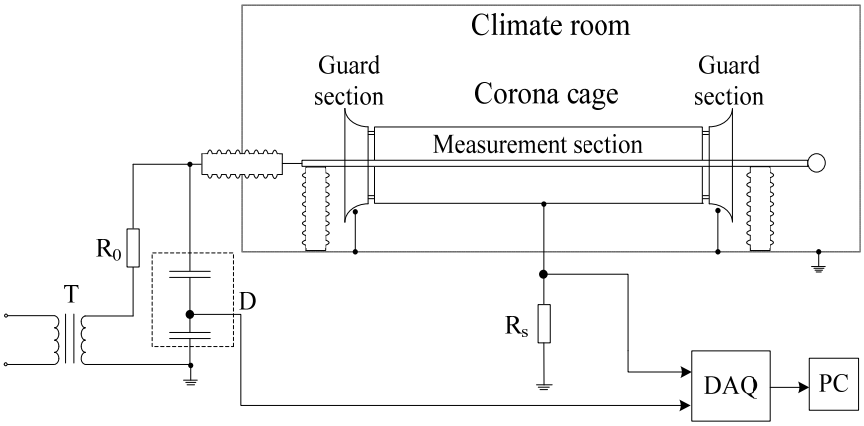

Figure 3-4: Schematic diagram of test circuit.

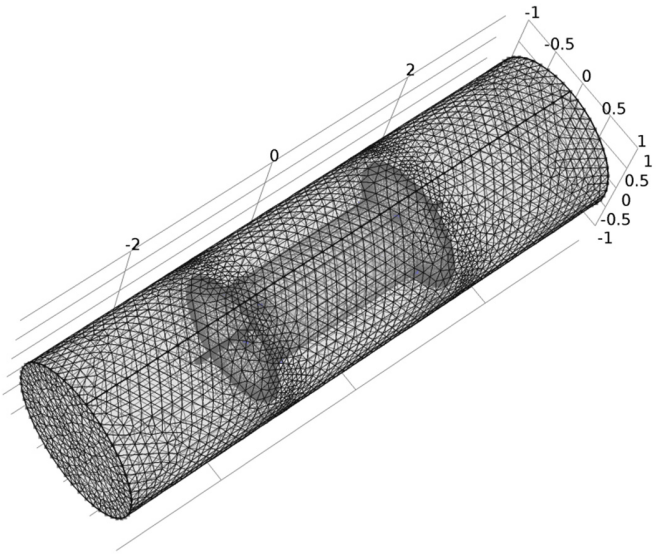

Figure 3-5: Laboratory corona cage.

To verify the effectiveness of guard sections at making the conductor surface electric field uniform in the longitudinal direction, a 3-D model with actual dimension was designed to simulate the electric field distribution, as shown in Figure 3-5. For this model, a voltage of 137.7 kV was applied to the inner conductor. The simulated results of the surface electric field along the conductor, for a voltage of 137.7 kV applied to the inner conductor, are shown in Figure 3-6. For an infinitely long corona cage with the same configuration and applied voltage, the calculated theoretical conductor surface electric field value is about 25 kV/cm. From Figure 3-6, it can be seen that the simulated electric field at the conductor surface is fairly uniform over the whole measurement section (from -1 m to 1 m) when two guard sections are installed and is almost identical with the theoretical value when the corona cage has an infinite length.

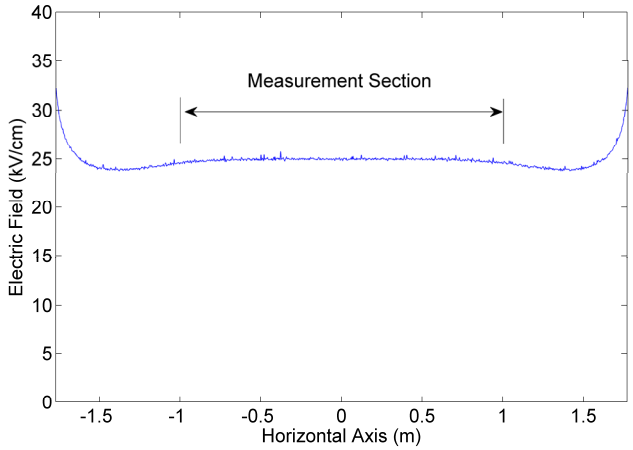

Figure 3-6: The simulated conductor surface electric field distribution along the conductor.

3.1.3 Data acquisition and processing system

Under AC voltages beyond the corona onset voltage, the electric field at the conductor surface varies with time, both in intensity and polarity, and thus various corona pulses can be observed in the same applied voltage cycle. These include Hermstein glow, positive onset streamers, and burst pulses in the positive half cycle and Trichel pulses in the negative half cycle. However, as described in [38], it is the creation and movement of positive and negative ions that is mainly responsible for the generation of CL. Electrons created in corona discharges have a very short lifetime and the corona pulses produced by their rapid movement do not contribute significantly to CL. Assuming that a corona pulse has a duration time t_{cp} and much longer relative time intervals T_{cp} (the repetition rate $f_{cp}=1/T_{cp}$), then its "effective time" component contributing to CL can be calculated by t_{cp}:f_{cp} per second. Taking the Trichel pulses as an example, they are normally regular with very short rise time (as short as 1.3 ns) and very short durations (tens of ns) separated by much longer time intervals (tens of μs) [95]. Therefore, the "effective time" component of Trichel pulses is about 0.001. Thus, although the Trichel pulses have relatively higher magnitudes, their contributions to CL can be neglected. The insignificance of corona pulses on CL was also confirmed by Lv [17]. In Lv's study, CL was measured with different sampling rates from 10 KSamples/s up to 120 MSamples/s. The results showed that the measured CLs were almost identical

with different sampling rates. As the corona pulses have little influence on corona loss, their contribution is not discussed in this study.

In previous studies, there are several methods commonly used to measure the corona loss such as Schering Bridge and dynamometer wattmeter [53]. The Schering Bridge circuit is the one that is used widely in high voltage laboratories. In the modern version of this circuit, the detector and the low voltage arms are incorporated into a single instrument. The instrument is self-adjusting and reads the corona loss and the capacitance of the test objects simultaneously. However, the bridge only measures the corona losses at one frequency, usually the fundamental. If there are many other frequencies also contributing to the corona loss, the choice of bridge may cause an error with respect to the total corona loss. The dynamometer wattmeter is an integrated instrument which sums all the fundamental corona loss and harmonic corona loss together. It cannot distinguish the fundamental or each harmonic corona loss from the total corona loss. Furthermore, most dynamometer wattmeters are subject to large errors at low power factors.

To analyze the corona harmonics, it is necessary to measure separately the component of corona loss associated with each frequency present in the system. With the advancement of technology, the voltage and corona current signals can be sampled continuously at very high precision and speed. Following this initial data recording, these sampled data can then be used for harmonics analysis in the post processing by data analysis software. In the present study, the instantaneous voltage and current were registered through a voltage and corona current acquisition system. Both the voltage and corona current were sampled at a rate of 100 kSamples/s simultaneously by a NI PCI-6251 data acquisition (DAQ) board which has a sampling rate up to 1 M samples/s, as shown in Figure 3-7. The sampled values were transmitted via coaxial cables for noise reduction and were then stored electronically by LabVIEW. Before the measurement, the sampling system was corrected by DC power sources.

Figure 3-7: Data acquisition board NI PCI-6251

With the instantaneous voltage and current known, the corresponding CL can be calculated. To eliminate the offset error which is the erroneous value of current (or voltage) read by the measurement system when the actual current (or voltage) is zero, a fast Fourier transform (FFT) method was applied before the calculation of CL.

As current and voltage signals were sampled in discrete time, the average CL in n cycles can be calculated as

$$P = \frac{1}{nN} \sum_{i=1}^{nN} U_i I_i \tag{3.1}$$

where N is the total number of data sampled in one cycle, U_i and I_i are the i_{th} sampled values in the calculated cycles.

3.2 Test procedure

Environmental parameters probably have one of the most influences on corona performance as they can change the conductor surface condition and affect the corona discharge accordingly. To study and measure these parameters accurately, a microprocessor-based versatile instrument, OMEGA HHF710, as shown in Figure 3-8, was used. This device deals with relative humidity, temperature, and

air velocity measurements in a highly versatile way. After ice accretion, the ice weight was measured by a balance APX-1502 with precision of 0.01 g, as shown in Figure 3-9.

Figure 3-8: OMEGA HHF710

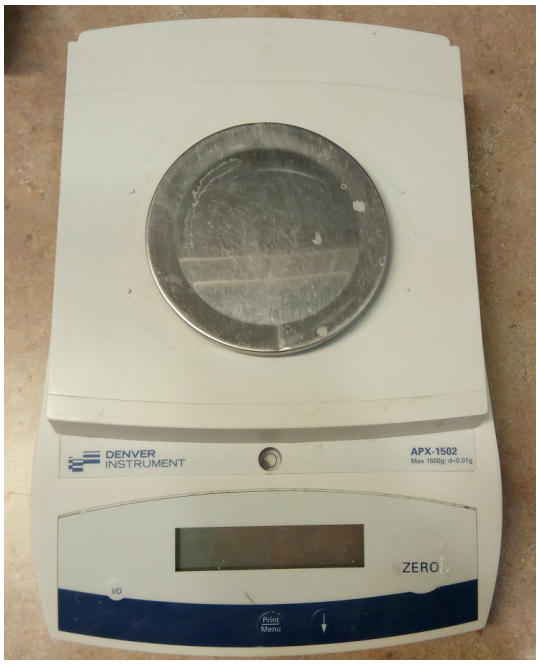

Figure 3-9: Balance APX-1502

The water conductivity was measured by Yokogawa SC72, an accurate, portable, and easy-to-use conductivity handheld meter, as shown in Figure 3-10. The measured freezing water conductivity was corrected to 50 μS/cm at 20 ℃ by the following equation [96]

$$\sigma_t = \frac{\sigma_{20}}{k_t} \tag{3.2}$$

where σ_{20} is 50 μS/cm, σ_t is the measured water conductivity at the water temperature, and k_t is the temperature coefficient. The coefficient k_t at different temperatures is listed in Table 3-1 [96]. Based on the values in Table 3-1, the relation between coefficient k_t and temperature t can be fitted by

$$k_t = p_1 \times p_2^t + p_3 \tag{3.3}$$

where p_1=1.28704, p_2=0.96128, and p_3=0.41571. The relative error between the calculated values by (3.3) and the values in Table 3-1 is less than 0.11%.

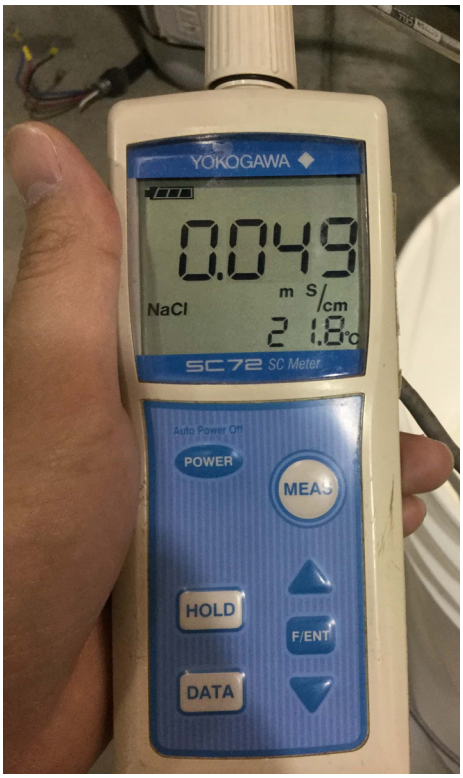

Figure 3-10: Balance APX-1502

Table 3-1: Temperature Coefficient at Different Temperatures

t (℃)	1	2	3	4	5
k_t	1.6511	1.6046	1.5596	1.5158	1.4734
t (℃)	6	7	8	9	10
k_t	1.4323	1.3926	1.3544	1.3174	1.2817
t (℃)	11	12	13	14	15
k_t	1.2487	1.2167	1.1860	1.1561	1.1274
t (℃)	16	17	18	19	20
k_t	1.0997	1.0732	1.0477	1.0233	1.0000
t (℃)	21	22	23	24	25
k_t	0.9776	0.9559	0.9350	0.9149	0.8954
t (℃)	26	27	28	29	30
k_t	0.8768	0.8588	0.8416	0.8252	0.8095

All the environmental parameters are listed in Table 3-2. Two kinds of ice were accreted, glaze ice and rime.

Table 3-2: Environmental Parameters

	Glaze ice	**Rime ice**
Ambient air temperature (℃)	-8	-15
Relative humidity (%)	≥ 90	≥ 90
Water droplet size (μm)	59	38
Freezing water conductivity σ20 (μS/cm)	50	50
Wind velocity (m/s)	2, 3	2, 3, 4
Precipitation rate (mm/h)	8, 15	15

To study the corona characteristics at different electric field strengths, the applied voltage was varied. However, one of the problems induced by changing the voltage is the loss stabilization, especially for fair condition, as shown in Figure 3-11. With increasing voltage, corona loss reached a temporary maximum at the new voltage level and then stabilized at a lower value after a while. With decreasing voltage, a temporary minimum corona loss was obtained before it stabilized at a higher value. Although the final values were almost identical for the same voltage, the stabilization time ΔT_2 was much shorter than ΔT_1. This stabilization time was even negligible in rain weather. To minimize the discrepancy brought by the stabilization process, the decreasing method was chosen in this study.

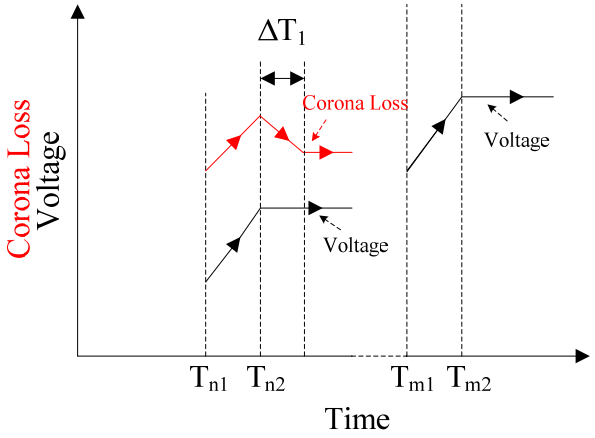

(a) With increasing voltage

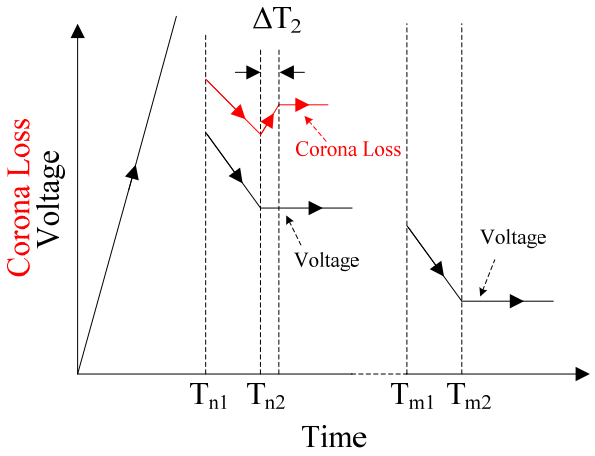

(b) With decreasing voltage

Figure 3-11: Stabilization process of two different methods

For EHV transmission lines, the conductor surface electric field can be as high as 22 kV/cm for single conductor configuration. When bundled conductors are employed, the conductor could be decreased to 11 kV/cm [15][33]. Even for the UHV transmission lines, the conductor surface electric field is normally less than 25 kV/cm [97]. Therefore, six surface electric field strength levels, ranging from 0 kV/cm to 25 kV/cm, were investigated in the present study. For an inner smooth conductor and an outer metallic mesh cylinder constructed in a coaxial cylindrical configuration, the electric field at the surface of conductor $E_{surface}$ (kV/cm) can be calculated, using Equation (2.1). Given the radii of the

smooth conductor and meshed cylinder 1.6 cm and 50 cm respectively in this study, the voltages corresponding to different electric strength levels are shown in Table 3-3. As the actual electric field strength changes during the ice accretion, unless otherwise mentioned, the values of the conductor surface electric field (CSEF) are the surface field strengths of the conductor before ice is accreted on its surface.

Table 3-3: Surface Field Strength and Corresponding Voltage for the Tested Corona Cage Configuration

CSEF	5 kV/cm	10 kV/cm	15 kV/cm	20 kV/cm	25 kV/cm
Voltage (kV)	27.5	55.1	82.6	110.1	137.7

The test procedures under glaze and rime ice conditions are described as follows [94]:

Step 1: In order to deposit the proper icing type, the climate room is first cooled down to a pre-set temperature set by PID. After the pre-set temperature is obtained, one hour is allowed for temperature stabilization.

Step 2: A proper voltage, as indicated in Table 3-3, is applied to the conductor to generate the desired surface electric field strength. Immediately after that, the voltage and corona current acquisition system is switched on.

Step 3: The water spraying system and fans are turned on simultaneously to generate the anticipated precipitation intensity and wind velocity. For each ice accretion, the conductor is subjected to a constant electric field strength during the whole process. Each ice accretion process lasts 40 minutes.

Step 4: After ice accretion, applied voltage is raised to a high level above the corona onset voltage and then reduced to zero at a rate of 2 kV/s to get a corona loss curve against different applied voltages.

Step 5: The ice was removed from the conductor and weighted. For glaze ice accretion, the icicles were removed first and then the ice on the conductor surface.

As corona characteristics are very sensitive to environmental conditions, it is very important that the environmental parameters are kept constant during the whole ice accretion process. With careful control, the measurements carried out in the climate room were found to be repeatable.

CHAPTER 4

THE INFLUENCE OF ELECTRIC FIELD STRENGTH ON ICE FORMATION

CHAPTER 4

THE INFLUENCE OF ELECTRIC FIELD STRENGTH ON ICE FORMATION

This chapter investigate the influence of electric field strength on ice appearance, ice weight, icicle spacing, icicle length, and angle between adjacent icicles. The following results are based on the experimental tests when the water conductivity was 50 μS/cm. The liquid water content was 2.1 g/m^3 at wind velocity of 2 m/s and 1.4 g/m^3 at wind velocity of 3 m/s.

4.1 The influence of electric field strength on ice appearance

Figures 4-1 and 4-2 show the visual appearances of rime and glaze ice accreted at different electric strength levels. When there is no voltage applied, the rime is full of small protuberances on the conductor surface and the glaze on the conductor surface is very smooth. For rime accretion, there is an increasing belt of water film on the windward side of the conductor with an increase in electric field strength because of Joule heat as shown from pictures (b) to (f) of Figure 4-1. For glaze ice accretion, as can be seen in pictures (e) and (f) of Figure 4-2, surface roughness increases obviously when the electric field is higher than 15 kV$_{rms}$/cm.

(a) 0 kV$_{rms}$/cm (b) 5 kV$_{rms}$/cm (c) 10 kV$_{rms}$/cm

(d) 15 kV_{rms}/cm (e) 20 kV_{rms}/cm (f) 25 kV_{rms}/cm

Figure 4-1: Accreted rimes at different electric fields.

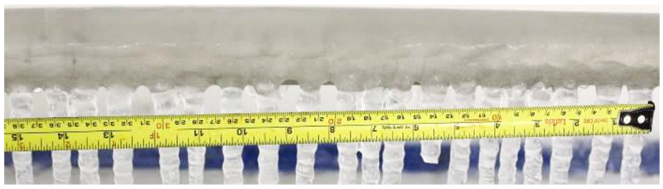

(a) 0 kV_{rms}/cm

(b) 5 kV_{rms}/cm

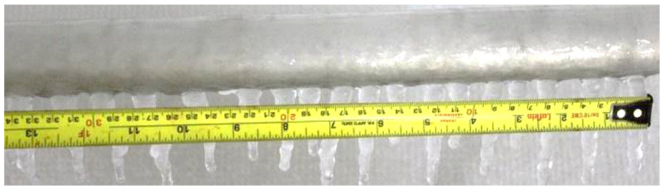

(c) 10 kVrms/cm

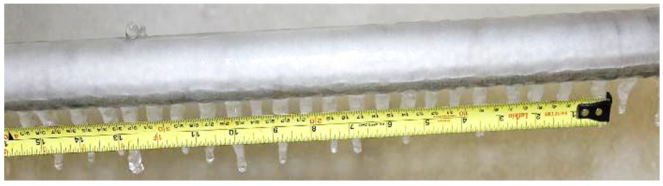

(d) 15 kVrms/cm

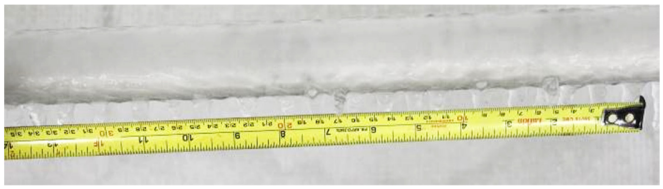

(e) 20 kV_{rms}/cm

(f) 25 kV_{rms}/cm
Figure 4-2: Icicles formed at different electric fields.

4.2 The influence of electric field strength on ice weight

Each ice test was repeated three times. The weights of rime and glaze ice accretion after the icing process are listed in Tables 4-1 and 4-2 and plotted in Figures 4-3 and 4-4. It can be seen from Figure 4-3 that the weight of rime first increases with electric field strength up to 20 kV_{rms}/cm and then decreases when the electric field strength is increased further. For glaze ice accretion, the glaze ice is separated into conductor surface ice weight and icicle weight. It can be seen from Figure 4-4 that the conductor surface weight has the same trend as that of rime accretion when electric field strength increases. Glaze on the conductor surface reaches a maximum weight of 5.35 g/cm at 20 kV_{rms}/cm and then decreases to 4.60 g/cm when the electric field strength is increased to 25 kV_{rms}/cm. The decrease of rime weight for rime accretion and conductor surface glaze ice weight for glaze accretion when the electric field strength is higher than 20 kV_{rms}/cm is caused by the generation of ionic wind, which repelling the approaching water droplets and decreasing the collision efficiency accordingly. The total glaze ice weight is also shown in Figure 4-4. Although the presence of electric field causes the water droplets to be attracted to the conductor by the polarization effect, the total weight for various electric field strengths is still less than that when there is no voltage applied, due to Joule heat. It should also be noted that the percentage of icicle weight varies with electric field. In Table 4-2, icicle weight accounts

for 51.4% of the total weight without the presence of electric field. However, when the electric field is up to 20 kV_{rms}/cm, this percentage decreases to 14.0%.

Table 4-1: Rime Weights on Conductor Surface at Different AC Electric Field Strengths with Wind Velocity of 2 m/s.

	0 kV_{rms}/cm	**5 kV_{rms}/cm**	**10 kV_{rms}/cm**	**15 kV_{rms}/cm**	**20 kV_{rms}/cm**	**25 kV_{rms}/cm**
Ice Weight (g/cm)	3.67	3.74	3.93	4.29	5.79	5.15

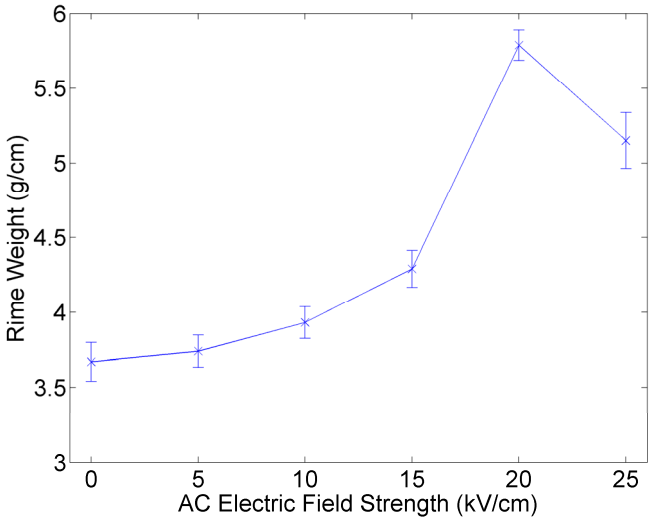

Figure 4-3: Weight of rime under various energized conditions.

Table 4-2: Glaze Weights at Different AC Electric Field Strengths with Wind Velocity of 2 m/s.

	Surface Weight (g/cm)	**Icicle Weight (g/cm)**	**Total Weight (g/cm)**	**Percentage of Icicle Weight (%)**
0 kV_{rms}/cm	3.83	4.05	7.88	51.4
5 kV_{rms}/cm	4.09	2.06	6.15	33.5
10 kV_{rms}/cm	4.46	2.33	6.79	34.3
15 kV_{rms}/cm	4.65	1.20	5.85	20.5
20 kV_{rms}/cm	5.35	0.87	6.22	14.0
25 kV_{rms}/cm	4.60	0.78	5.38	14.5

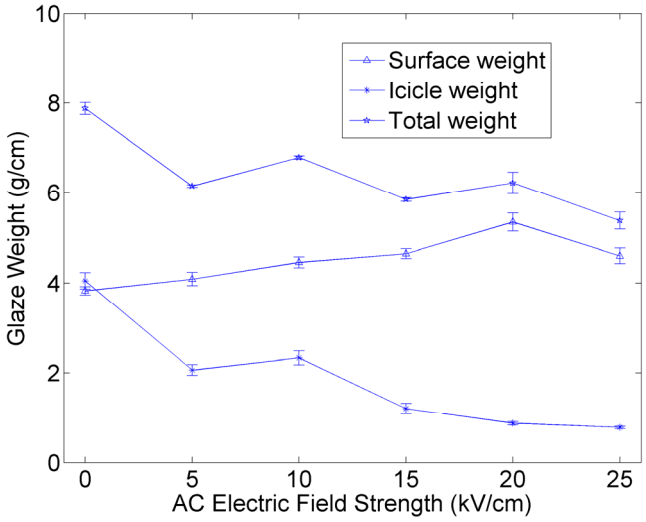

Figure 4-4: Weight of glaze ice under various energized conditions.

As ice accretion is significantly influenced by collision water droplet efficiency which is determined by the net force imposed on the water droplets approaching the conductor, the analysis of each force was made as follows to further explain the above results.

When the test conductor is energized during ice accretion, the water droplets approaching the conductor are distorted by the electric field. If the distortion is small, the water droplet can be approximated by an ellipsoid of revolution with semi-major axis A, in the direction of the electric field, and with semi-minor axis B. The degree of this distortion can be expressed by eccentricity e which is defined in [98]

$$e = \sqrt{1 - \frac{B^2}{A^2}} \tag{4.1}$$

When the background electric field is $\boldsymbol{E}$, eccentricity e of water droplet in the field can be expressed as [98]

$$e = \frac{3|\boldsymbol{E}|(\varepsilon_2 - \varepsilon_1)(\varepsilon_0 \varepsilon_1 a / \gamma)^{1/2}}{2(\varepsilon_2 + 2\varepsilon_1)} \tag{4.2}$$

where $\boldsymbol{E}$ is in V/m, a (m) is equal to the radius of the spherical water droplet with the same volume, ε_0 is the vacuum permittivity which is 8.854×10^{-12} F/m, ε_1 and ε_2 are dimensionless dielectric constants of air and water droplet respectively, and γ is the surface tension which is 0.076 N/m at 0 ℃. As ε_2 is much higher than ε_1 (the ratio of the dielectric constant between water and air is 87 at 0 ℃ [99-100] in the presence of static or low frequency under 100 MHz), thus, (4.2) can be simplified as

$$e = \frac{3|\boldsymbol{E}|(\varepsilon_0\varepsilon_1 a/\gamma)^{1/2}}{2} \tag{4.3}$$

For water droplets with diameters $D = 2a = 59$ μm and 38 μm at 0 ℃, the critical electric fields for rupture of the water droplets ($e = 1$) are 113.7 kV/cm and 141.7 kV/cm respectively, namely effective values of 80.4 kV_{rms}/cm and 100.2 kV_{rms}/cm, both of which are sufficiently higher than the breakdown field strength for air (about 30 kV_{rms}/cm). Thus, these two sizes of water droplets will not break up when they are approaching the conductor. When the water droplets are placed under various background electric fields from 5 to 25 kV_{rms}/cm, values of eccentricity e and ratio A/B at peak electric strength calculated by (4.1) and (4.3) are shown in Table 4-3.

Table 4-3: Distortion of Water Droplets by Background Electric Fields.

		0 kV_{rms}/cm	**5 kV_{rms}/cm**	**10 kV_{rms}/cm**	**15 kV_{rms}/cm**	**20 kV_{rms}/cm**	**25 kV_{rms}/cm**
D = 59 μm	e	0.06	0.12	0.19	0.25	0.31	0.06
	A/B	1.002	1.007	1.019	1.033	1.052	1.002
D = 38 μm	e	0.05	0.10	0.15	0.20	0.25	0.05
	A/B	1.001	1.005	1.011	1.021	1.033	1.001

From Table 4-3, it can be seen that when the background electric field is 5 kV_{rms}/cm, the ratio A/B is equal to 1.002 and 1.001 for water droplets with diameters of 59 μm and 38 μm respectively. Thus, the water droplets can be considered as perfect spheres. When the background electric field is increased to 25 kV_{rms}/cm, the ratios A/B of two types of water droplets are 1.052 and 1.033 respectively. It means that the water droplets can still be approximated by spheres. For a liquid sphere placed in an external electric field $\boldsymbol{E}$, a dipole moment p will be generated. As the sphere is very small, it can be

assumed that background electric field around the sphere is uniform. Hence, p can be expressed as in [101]

$$\boldsymbol{p} = \frac{\varepsilon_2 - \varepsilon_1}{\varepsilon_2 + 2\varepsilon_1} 4\pi\varepsilon_0\varepsilon_1 a^3 \boldsymbol{E} \approx 4\pi\varepsilon_0\varepsilon_1 a^3 \boldsymbol{E} \tag{4.4}$$

The dielectrophoretic force $\boldsymbol{F}_{DEP}$ on the polarized droplet then can be calculated by

$$\boldsymbol{F}_{DEP} = \boldsymbol{p} \cdot \nabla \boldsymbol{E} = 4\pi\varepsilon_0\varepsilon_1 a^3 \boldsymbol{E} \cdot \nabla \boldsymbol{E} \tag{4.5}$$

To simplify the analysis, it is assumed that there is no ice accreted on the conductor yet. By symmetry, the electric field is everywhere radially inward or outward, perpendicular to the axis of conductor. This means that in terms of cylindrical polar coordinates, $E_\theta = Ez = 0$ kV/cm and $F_\theta = F_z = 0$ N. Thus, the electric field at any point between the conductor and the meshed cylinder can be expressed as

$$\boldsymbol{E} = E_r \frac{\boldsymbol{r}}{|\boldsymbol{r}|} = \frac{U_{app}}{r \ln(R/r_c)} \frac{\boldsymbol{r}}{|\boldsymbol{r}|} \tag{4.6}$$

where r is the shortest distance from the axis of the conductor to the water droplet, $\boldsymbol{r}$ is a vector pointed radially outward.

Substituting (4.6) into (4.5), the following equation can be obtained:

$$\boldsymbol{F}_{DEP} = F_r \frac{\boldsymbol{r}}{|\boldsymbol{r}|} = 4\pi\varepsilon_0\varepsilon_1 a^3 E_r \frac{\partial E_r}{\partial r} \frac{\boldsymbol{r}}{|\boldsymbol{r}|} = -4\pi\varepsilon_0\varepsilon_1 a^3 \frac{U_{app}^2}{\ln^2(R/r_c)} \times \frac{1}{r^3} \frac{\boldsymbol{r}}{|\boldsymbol{r}|} \tag{4.7}$$

The minus sign of equation (4.7) indicates that the dielectrophoretic force $\boldsymbol{F}_{DEP}$ on the polarized droplet always attracts the droplet toward the conductor, which is the direction from a lower electric field pointed to a higher electric field. The acceleration component generated by the dielectrophoretic force can be obtained as

$$\boldsymbol{a}_{DEP} = \frac{\boldsymbol{F}_{DEP}}{\frac{4}{3}\pi a^3 \rho_{water}} = -\frac{3\varepsilon_0 \varepsilon_1}{\rho_{water}} \times \frac{U_{app}^2}{\ln^2(R/r_c)} \times \frac{1}{r^3} \frac{\boldsymbol{r}}{|\boldsymbol{r}|} \tag{4.8}$$

From (4.8), it can be seen that when the water droplet is small, the acceleration a_e is independent of the water droplet dimension. When the conductor is energized with various surface electric field strengths, from 5 to 25 kV_{rms}/cm, and the water droplets are approaching the conductor at different distances away from the conductor surface, the acceleration component induced by electric field, as calculated by (4.8), is shown in Table 4-4.

Table 4-4: Acceleration (m/s^2) Component Induced by Electric Force at Various Distances from Conductor Surface.

Distance	5 kV_{rms}/cm	10 kV_{rms}/cm	15 kV_{rms}/cm	20 kV_{rms}/cm	25 kV_{rms}/cm
0 cm	-0.83	-3.32	-7.47	-13.27	-20.75
1 cm	-0.19	-0.77	-1.74	-3.09	-4.84
5 cm	-0.01	-0.05	-0.11	-0.19	-0.30

In addition to the dielectrophoretic force applied on water droplets, water droplets moving with the air are also subjected to a viscous drag force. When the relative velocity is slow, the resulting expression for the drag, known as Stokes' drag [102], is expressed as

$$\boldsymbol{F}_d = -6\pi\eta a \boldsymbol{V} \tag{4.9}$$

where a is the radius of the droplet in m, η is the fluid viscosity with a value of 1.66×10^{-5} Pa·s for air at -15 ℃, and $\boldsymbol{V}$ is the relative velocity between droplet and fluid in m/s. The acceleration component $\boldsymbol{a}_d$ generated by the drag force can be obtained as

$$\boldsymbol{a}_d = \frac{\boldsymbol{F}_d}{\frac{4}{3}\pi a^3 \rho_{water}} = -\frac{9\eta \boldsymbol{V}}{2a^2 \rho_{water}} \tag{4.10}$$

Since the diameters of water droplets are very small, it is generally assumed that the water droplets are moving with the same velocity as the air [103]. Due to their mass, droplets ejected from

nozzles need a certain time to adapt to sudden changes in local air velocity. The characteristic time scale for adaptation to such changes is the so-called relaxation time τ which is expressed as

$$\tau = \frac{mv}{F_d} = \frac{\frac{4}{3}\pi a^3 \rho_{water} v}{6\pi\eta a v} = \frac{2a^2 \rho_{water}}{9\eta} \tag{4.11}$$

The time required for the droplet to reach a fraction β of wind velocity was determined in [103] as

$$t_\beta = -\tau \ln(1-\beta) \tag{4.12}$$

Thus, it takes 81 ms and 33 ms respectively for the droplets with diameters of 59 μm and 38 μm to reach 99.9% of the wind velocity. This computation shows that when the droplet is small, the droplet can reach to wind velocity in a very short time. However, because of gravity, there is still a slight difference between the speed of water droplets and the wind. When the wind velocity is 1.22 m/s and the water droplet is in a range of 20-100 μm, the relative velocity between wind and water droplet is less than 0.8% of the wind velocity [99]. Assuming that the water droplets are moving with the air at a relative velocity of 0.02 m/s when the wind velocity is 2 m/s, the accelerations caused by the drag force are 1.72 m/s^2 and 4.14 m/s^2 for droplets with diameters of 59 and 38 μm respectively. From Table 4-4, it can be seen that when the water droplets are less than 1 cm from the conductor surface, the accelerations caused by the dielectrophoretic force and the drag force are comparable.

Dielectrophoretic force attracts water droplets to the conductor surface as indicated by equation (4.8). Thus, the collision efficiency increases with an increase in conductor surface electric strength, leading to an increasing weight of rime and glaze ice accretion, as shown in Tables 4-1 and 4-2. However, when the electric strength is higher than 20 kV_{rms}/cm, corona wind is generated. The generated corona wind blows the air away from the conductor. As the airflow is diverted by the corona wind, the water droplets moving toward the conductor are deflected more, leading to a decrease in collision efficiency. Therefore, when the conductor surface electric strength is increased further to 25 kV_{rms}/cm, weights of

rime and glaze ice accretion decrease. When the electric strength is less than 20 kV_{rms}/cm, water droplets are subjected to dielectrophoretic and drag forces. As water droplets are ejected from the nozzles, they are initially moving at the same velocity as the air, and their trajectories are determined by acceleration. From Equation (4.8), it can be seen that the acceleration due to dielectrophoretic force is independent of water radius *a*. However, from equation (4.10), it can be seen that water droplets with a larger radius *a* (for glaze ice accretion) have a smaller acceleration due to drag force, so that larger water droplets are more likely to keep their previous moving direction than be deflected by the drag force. Thus, the collision efficiency for glaze ice accretion is higher than that for rime accretion when the electric strength is less than 20 kV_{rms}/cm. Although the frozen coefficient (the fraction of the accreted water droplets which freezes) is less than one unit for glaze ice accretion and equal to one unit for rime accretion, the weight of glaze ice is still higher than that of rime when the conductor surface electric strength is in a range of 0-15 kV_{rms}/cm. When the conductor surface electric strength is higher than 15 kV_{rms}/cm, the weight of rime surpasses that of glaze ice. Two reasons may explain that. Firstly, as conductor surface electric strength is increased, the frozen coefficient of glaze ice accretion drops due to the increasing Joule heat by corona discharge. For rime accretion, however, the water film on the windward of the conductor is negligible compared with the whole of ice accretion. Thus, the frozen coefficient of rime accretion is still nearly equal to one unit even if the electric strength is 25 kV_{rms}/cm. Secondly, since the density of rime is smaller than that of glaze ice, the diameter of the rime accreted conductor will be larger than that of the glaze ice accreted conductor if same masses are accreted on the conductor surface. A larger diameter means that more water droplets will be captured by the conductor.

4.3 The influence of electric field strength on icicle spacing

When enough precipitation is captured by the conductor and temperature is appropriate, pendant drops are formed on the lower surface of the conductor and freeze. As water film flows along the drop tip due to gravity, icicles are formed as shown in Figure 4-2. As icicles grow further, the unfrozen water film flows along the surface of the icicles to the icicle tip, resulting in unchanged icicle

spacing during the whole ice accretion process [104]. Thus, the spacing of icicles is decided by the spacing of the pendant drops frozen in the beginning, namely the diameter of the unfrozen drops.

The experiment results are given in Table 4-5. The spacing of icicles in the table is an average value of length measured divided by the number of spacings contained in that measured length. Two precipitation rates of 15 and 8 mm/h were carefully tested in the experiments. When the precipitation rate (PR) was 15 mm/h, there was significant precipitation captured by the conductor and considerably large pendant water drops were observed before they were frozen. When PR was 8 mm/h, the ice accretion was just over the transition between rime and glaze ice accretion and the pendant drops were frozen immediately in the initial stage. The results in Table 4-5 show that the icicle spacings are between 14.7 and 20.2 mm when PR is 15 mm/h. As electric field strength is increased, icicle spacing decreases. This is obvious since as electric field increases, the pendant water drops get elongated, leading to a smaller spacing. When PR is 8 mm/h, icicle spacing seems constant and independent of the electric field when electric field strength is less than 20 kV_{rms}/cm. However, when the electric strength is increased further, icicle spacing decreases.

Table 4-5: Spacings of Icicles (mm) at Different Electric Field Strengths.

	0 kV_{rms}/cm	**5 kV_{rms}/cm**	**10 kV_{rms}/cm**	**15 kV_{rms}/cm**	**20 kV_{rms}/cm**	**25 kV_{rms}/cm**
PR = 8 mm/h	20.8	20.5	21.2	20.6	17.8	16.3
PR =15 mm/h	20.2	19.5	18.6	17.7	16.5	14.7

In order to analyze the spacing of icicles or the diameter of the initial pendant drop on the surface of an energized conductor, a quasi-equilibrium state can be assumed. The equilibrium profile of a pendant drop under the electric field can be determined by the surface tension, gravity, and electrical pressure induced by the electric field strength. The former force tends to attract the water drop back to the surface of the conductor while the latter two forces tend to pull it downward.

The pressure results from the electric field at the surface of the drop can be calculated by the following equation from [105]

$$P_e = \frac{1}{2}[\varepsilon^{(a)} E_n^{(a)2} - \varepsilon^{(b)} E_n^{(b)2} + (\varepsilon^{(b)} - \varepsilon^{(a)}) E_t^2] \tag{4.13}$$

where P_e is in Pa, E_n and E_t are the normal and tangential components of the electric field $\boldsymbol{E}$ at the drop surface in V/m, ε is the permittivity of the fluid in F/m, and superscripts a and b refer to the air and the water drop liquid, respectively. When the water drop is conductive, it can be assumed that there is no electric field inside the drop and that the electric field is normal to the drop surface. Thus, the governing equation for conducting drops can be simplified as

$$P_e = \frac{1}{2}\varepsilon^{(a)} E_n^{(a)2} \tag{4.14}$$

The profile of the pendant drop is symmetrical about the z-axis and its cylindrical coordinates are shown in Figure 4-5. Let z be the ordinate, γ the surface tension, $\Delta\rho$ the density between water and air, and g the acceleration of gravity. For the convenience of the force analysis, an imaginary cylinder was used. Its axis is exactly z and has a radius of r.

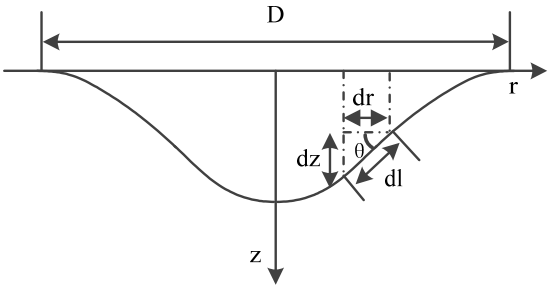

Figure 4-5: Cross-section of a pendant drop.

The part of pendant drop contained in the imaginary cylinder is supported by the vertical component of the surface tension at the intersection between the drop surface and coaxial cylinder r, i.e.

$$F_\gamma^v = 2\pi r\gamma \sin\theta \tag{4.15}$$

Considering the water between the two coaxial imaginary cylinders r and r + dr, the vertical force due to gravity and buoyance of air is

$$F_g = \Delta\rho g 2\pi r z dr \tag{4.16}$$

and the downward force due to electrical pressure can be expressed as

$$F_e = 2\pi r dl \cos\theta P_e = 2\pi r P_e dr \tag{4.17}$$

Integrating from 0 to r, the equilibrium equation can be obtained as follows

$$2\pi r\gamma \sin\theta + \int_0^r \Delta\rho g 2\pi r z dr + \int_0^r 2\pi r P_e dr = 0 \tag{4.18}$$

As the drop grows very slow and is considerably flat in its initial stage, E_n can be assumed constant and equal to the magnitude of conductor surface electric strength E_0 before precipitation. Thus,

$$P_e = \frac{1}{2}\varepsilon_0 E_0^2 \tag{4.19}$$

Taking the derivative of (4.18) yields

$$\frac{d(\gamma r \sin\theta)}{dr} + \Delta\rho g r z + P_e r = 0 \tag{4.20}$$

According to the geometry,

$$\tan\theta = \frac{dz}{dr} \tag{4.21}$$

$$\sin\theta = \frac{\tan\theta}{\sqrt{1+\tan^2\theta}} \tag{4.22}$$

Substituting (4.19), (4.21) and (4.22) into (4.20) yields

$$\gamma \frac{d\left(\dfrac{r\dfrac{dz}{dr}}{\sqrt{1+\left(\dfrac{dz}{dr}\right)^2}}\right)}{dr} + \Delta\rho r g z + \frac{1}{2}\varepsilon_0 E_0^2 r = 0 \tag{4.23}$$

Since the drop is formed very slowly and we are only interested in its initial stage, the term $(dz/dr)^2$ is very small and can safely be neglected in (4.23). Then (4.23) can be simplified as

$$\frac{d^2 z}{dr^2} + \frac{1}{r}\frac{dz}{dr} + \frac{\Delta\rho g z}{\gamma} + \frac{\varepsilon_0 E_0^2}{2\gamma} = 0 \tag{4.24}$$

Let

$$\eta = \frac{\Delta\rho g z}{\gamma} + \frac{\varepsilon_0 E_0^2}{2\gamma},\ \ \lambda = \sqrt{\frac{\gamma}{\Delta\rho g}},\ \ \xi = \frac{r}{\lambda} \tag{4.25}$$

then (4.24) is reduced to

$$\frac{d^2\eta}{d\xi^2}+\frac{1}{\xi}\frac{d\eta}{d\xi}+\eta=0 \tag{4.26}$$

which is the Bessel equation of zero order. The appropriate boundary conditions for the present problem are

$$\frac{d\eta}{d\xi}=0 \qquad \text{at } \xi=0 \text{ and } \xi=\alpha \tag{4.27}$$

where α is the first characteristic value of (4.26) and can be taken as the dimensionless radius of the rim of the drop. The value of α = 3.83 can be found in tabulated values of Bessel function. By (4.25) and Figure 4-5, the spacing of icicles, or diameter of the initial pendant drop is given as $D = 2\lambda\alpha$ = 21.3 mm.

As λ is not related to electric strength, it can be concluded that the spacing of icicles is independent of the electric strength of the conductor surface. This value of D is a theoretical calculation of icicle spacing and some assumptions to simplify the problem are assumed. The actual value of icicle spacing may differ from the theoretical value. Firstly, the growth of pendant drop is assumed to be slow and the pendant drop is frozen in its initial stage. If PR is high, pendant drops cannot be frozen in their initial stages and big pendant drops are formed before they are frozen. Thus, the equilibrium equation is reached in a more developed stage, making the diameter of the drop rim smaller. This is confirmed by the experimental results, so that when PR=15 mm, the measured D = 20.2 mm is smaller than the theoretical result. When electric strength is applied, the spacing can be further narrowed. This can be explained by the fact that, as the drop profile is changed by gravity, the electrical pressure is also changed. When the pendant drop is considerable, the actual drop surface electric field E_n cannot be assumed as E_0 anymore. Taking a hemispherical pendant drop as an example, the analytical solution for the drop surface electric field is $E_n=3E_0\cos(\theta)$. Then, the downward electrical pressure component can be expressed as

$$P_{ed}=P_e\cos(\theta)=\frac{9}{2}\varepsilon_0 E_0^2\cos^3(\theta) \tag{4.28}$$

From (4.28), it can be seen that the additional drop surface downward electrical pressure component increases from the drop rim (θ=0) to the drop tip (θ=π/2) and reaches its highest value at the

drop tip with a value of $9/2\varepsilon_0 E_0^2$. Therefore, if the electric field is applied, water moves from near the rim to the center of the drop and narrows the diameter of the drop further. This is consistent with the experimental results shown in Table 4-5 that when PR=15 mm/h, the spacing of icicles decreases from 19.5 to 14.7 mm with an increase in electric strength. When PR = 8 mm/h, the pendant drop is frozen in its initial stage and the spacing of icicles can be assumed constant at 20.8 ± 0.6 mm and independent of electric field when its strength is less than 20 kV_{rms}/cm. As the strength of the electric field increases further, corona discharge is very intensive and the heat generated by corona discharge power is significant. Thus, the pendant drops cannot be frozen in their initial stage and the spacing of icicles decreases with an increase in electric field when it is higher than 15 kV_{rms}/cm. Secondly, the roughness of the conductor surface is not considered. The theoretical value only applies to conductors with smooth surface. If the surface roughness is too high, the flowing of unfrozen water may be determined by the roughness dimension rather than the equilibrium equation (4.18). Thirdly, the effect of wind drag is neglected in the force analysis. It is very difficult to theoretically quantify the significance of wind as air flow is unknown. However, it is observed from our experiments that when wind velocity is less than 3 m/s, the wind drag seems has no effect on the spacing of icicles. As the wind drag tends to remove the pendant drop from the conductor surface, the effect of wind velocity may not be neglected if the wind velocity is very high.

The diameter of icicles at their roots was also measured after ice accretion as depicted in Figure 4-6. The results are presented in Table 4-6. From Table 4-6, it can be seen that the diameter of icicles at the root decreases with the increase of electric field. When the electric field is 25 kV_{rms}/cm, the diameter is just about half of the condition when there is no voltage applied.

Table 4-6: Diameters of Icicles at Root at Different Electric Fields.

	0 kV_{rms}/cm	**5 kV_{rms}/cm**	**10 kV_{rms}/cm**	**15 kV_{rms}/cm**	**20 kV_{rms}/cm**	**25 kV_{rms}/cm**
Experimental values (mm)	12.10	11.01	9.64	8.23	7.05	6.77

Figure 4-6: Diameter measurement of icicles.

4.4 The influence of AC electric field strength and wind velocity on length of icicles

After ice accretion, the lengths of accreted icicles were measured. The measured values are plotted in Figure 4-7. From this figure, it can be seen that icicle length is greatly influenced by conductor surface electric field. As the strength of electric field is increased, icicle length decreases. As the curvature of icicle tip is very high, the electric field near the icicle tip is severely distorted under energized conditions. At sufficiently high electric field strength, complex ionization processes take place in the air surrounding icicle tips, resulting in discharge phenomena known as corona. Corona discharge at the icicle tip is the major factor suppressing the growth of the icicles.

Since the length of icicles decreases with an increase in electric field as shown in Figure 4-7, the weight of icicles should be expected to have a monotone decreasing trend with an increase in electric field strength, as shown in Table 4-2. However, the weight of icicles per meter is not only due to the weight of individual icicles but also by the number of icicles per meter which is the reciprocal of icicle spacing. As the spacing of icicles decreases with an increase of electric field when PR = 15 mm/h, the total icicle weight is even higher at a conductor surface electric field of 10 kV_{rms}/cm than that of 5 kV_{rms}/cm.

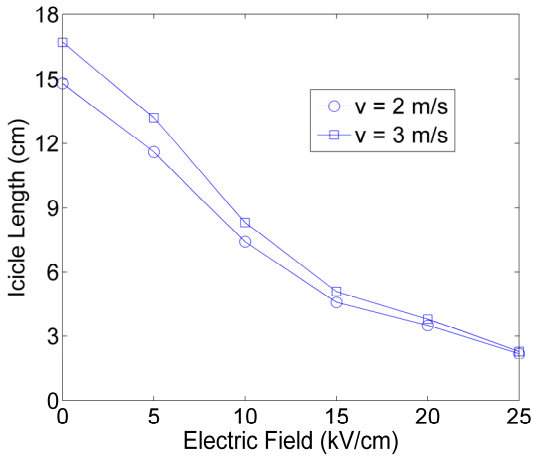

Figure 4-7: Icicle lengths at different electric fields and wind velocities when PR=15 mm/h.

It can also be seen from Figure 4-7 that wind velocity under tested conditions tends to favor the growth of icicles. For the growth of icicles, heat should be dissipated from the pendant drop and water film on icicle surface by means of convection, radiation, and evaporation. It was concluded that the heat dissipated by convection played a decisive role in the icicle growth process [106]. The convective heat transfer q_{conv} (W) is defined as

$$q_{conv} = hA(t_s - t_a) \tag{4.29}$$

where h is the convective heat transfer coefficient in W/(m^2·K), A is the heat transfer area of the surface in m^2, t_s and ta are the temperatures of water on icicle surface and ambient temperature respectively, in Celsius (℃). The convective heat transfer coefficient of air is approximately equal to [107]

$$h = 10.45 - v + 10v^{1/2} \tag{4.30}$$

where v is the wind velocity in m/s. Equation (4.30) is an empirical equation and can be used for velocities from 2 to 20 m/s. This equation is plotted in Figure 4-8. It can be seen that convective heat transfer coefficient increases with an increase of wind velocity. Thus, with the same electric strength, lengths of icicles are longer when the wind velocity is 3 m/s compared with that of 2 m/s.

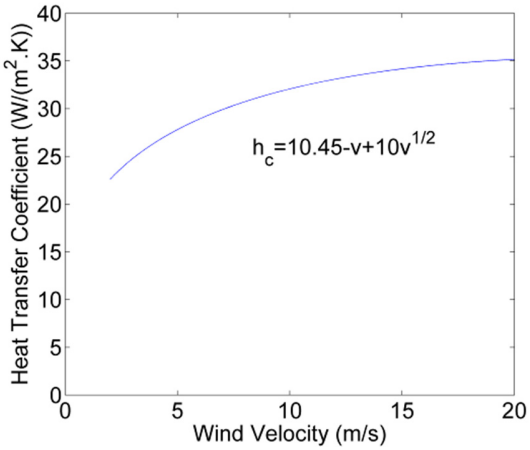

Figure 4-8: Convective heat transfer coefficient vs. wind velocity.

4.5 The influence of electric field strength on angle between adjacent icicles

Under windy conditions, the drops were blown toward the lee side of the conductor. In the absence of electric field, it was observed that the icicles were bent in a range of 6 to 10 degrees when the wind velocity was between 2 to 3 m/s. This is consistent with the empirical equation [108]

$$\varphi = 0.684v^2 + 0.14v + 4 \tag{4.31}$$

where φ is the bent angle of icicles and v is the wind velocity in m/s.

When conductor surface electric field strength was less than 25 kV_{rms}/cm, icicles were not growing perfectly straight. It is worth noting that there was an angle θ between adjacent icicles in the direction perpendicular to the conductor axis, as shown in Figure 4-9. This angle θ was small when the icicles were just forming and then kept increasing as the icicles were growing.

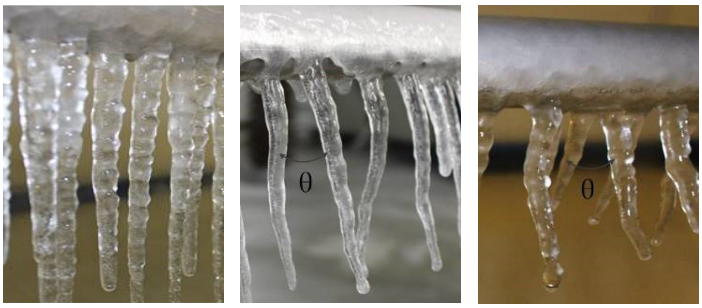

(a) 0 kV_{rms}/cm (b) 5 kV_{rms}/cm (c) 10 kV_{rms}/cm

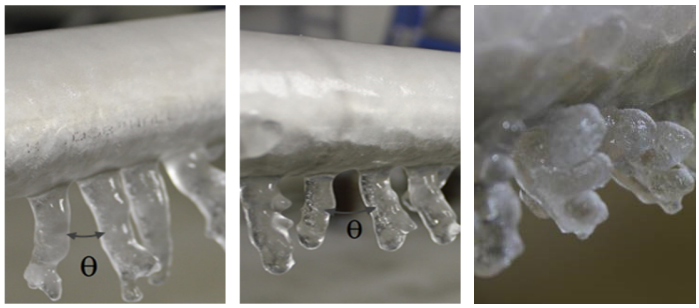

(d) 15 kV_{rms}/cm (e) 20 kV_{rms}/cm (f) 25 kV_{rms}/cm

Figure 4-9: Icicle deviation angle at different electric fields.

To represent this deviation angle of icicles at the end of ice accretion, angle Φ was defined. It is the angle measured from the tips of adjacent icicles to their roots as shown in Figure 4.10a. The measured average angles Φ are plotted in Figure 4-11. From Figure 4-11, it can be seen that angle Φ increases with an increase of electric field. When the conductor surface electric strength is equal to 25 kV_{rms}/cm, there is no obvious angle between adjacent icicles. However, there are many small branches in each icicle as shown in Figure 4-9f. According to the model proposed by Makkonen [109], the liquid water on icicles has three parts: i) water film on icicle surface, ii) the water trapped inside the icicle, and iii) the hemispherical pendant drop at icicle tip. The water film on the icicle surface is very thin and the elongation rate of the tip of an icicle is typically 20-60 times the radial growth rate of the walls. Therefore, icicle growth mainly depends on the freezing direction of the water droplet at the icicle tip.

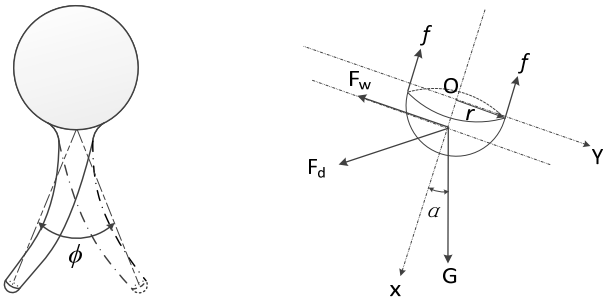

(a) Lateral view of the conductor (b) Forces imposed on the pendant drop

Figure 4-10: Diagram of icicles and force analysis of the icicle tip.

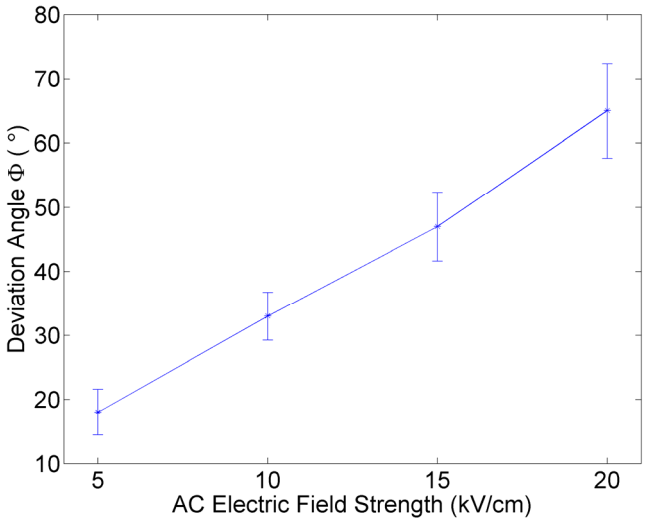

Figure 4-11: Angles between adjacent icicles at different electric fields

For a brief discussion of icicle growth, a lateral view of the conductor and a diagram of the forces imposed on the icicle tip are shown in Figure 4-10b. There are four forces acting on the pendant drop at the icicle tip, namely gravity (G), surface tension (f), wind (F_w), and electric (F_d) forces. The first two forces are represented as follows:

$$G = \iiint_V \rho_{water} dV \tag{4.32}$$

$$f = 2\pi r\gamma \tag{4.33}$$

where V is the domain of the pedant drop, and r is the radius of the interface as shown in Figure 4-10b. F_w can be expressed as determined in [110]

$$F_w = \iint_{\Sigma} P_w ds = \iint_{\Sigma} \frac{1}{2} \rho_{air} v^2 ds \tag{4.34}$$

where P_w is the wind pressure (Pa), $\sum$ is the windward of pendant drop, and v is the wind velocity in m/s. Since the water film is conductive, it can be assumed that there is no charge inside the icicle and that all the charges are distributed on the surface of the icicle. As the relationship between surface charge density and electric field is

$$\sigma = \varepsilon_0 E \tag{4.35}$$

Then, the electric force on the pendant drop of the icicle can be calculated as

$$\boldsymbol{F}_d = \iint_S \boldsymbol{E} dq = \iint_S \boldsymbol{E} \cdot \sigma ds = \iint_S \boldsymbol{E} \cdot \varepsilon_0 E ds \tag{4.36}$$

where S is the surface of the pendant drop. Assuming that all icicles have the same shape and curve toward left and right alternatively as shown in Figure 4-10a, it can be expected that the component of F_d along the conductor axis direction is canceled because of symmetry, and that F_d is only perpendicular to the conductor axis. As the water film is conductive, all charges accumulated on every pendant drop and on the icicle surface always have the same polarity. Thus, the pendant drops expel each other, leading to F_d pointing away from the conductor. If the pendant drop at the left icicle tip is taken as an example, the water droplet shown in Figure 4-10b is in equilibrium and is elongated in the direction making an angle α from the vertical when the conductor surface electric field is at a certain level. When the conductor surface electric field increases, the charge and the electric force F_d on the drop also increases according to (4.35) and (4.36). Thus, F_d pulls the pendant droplet left and increases angle α, leading to an increased Φ at the end of ice accretion. When there is enough charge accumulated on the drop surface and the electric field is sufficiently high, the drop is split and branches are formed, as shown in 4-9f.

4.6 Conclusion

A number of experiments were carried out to study the influence of electric field strength on ice formation. From the results obtained under the test conditions, the following conclusions can be drawn:

(1) Under both rime and glaze ice conditions, the weight of ice accreted increases with electric field strength up to 20 kV_{rms}/cm and then decreases as it is increased further.

(2) Under non-energized conditions and for a precipitation rate of 15 mm/h, about half of the total weight of glaze ice may be caused by icicle accretion. Under energized conditions, the weight percentage of icicles decreases with the increase of conductor surface electric field. When the electric field is higher than 20 kV_{rms}/cm, the weight percentage of icicles is lowered to 14%.

(3) When the precipitation rate is at a value close to ice accretion transition between rime and glaze, the icicles grow very slowly and the icicle spacing becomes independent of the conductor surface electric field. When the precipitation rate is sufficient, icicle spacing decreases as the electric field at the surface of the conductor is increased.

(4) AC electric field has a significant influence on the length of icicles. Corona discharge generated at the icicle tip suppresses the growth of the icicles.

(5) Under the energized conditions, there is an angle between adjacent icicles accreted on the conductor. The repulsion of the pendant drop at the icicle tip results in an increasing deviation angle as the electric field at the surface of the conductor is increased. When the electric field is higher than 20 kV_{rms}/cm, the pendant drop may split and lead to the formation of icicle branches.

CHAPTER 5

THE INFLUENCE OF ELECTRIC FIELD STRENGTH ON CORONA CHARACTERISTICS

CHAPTER 5

THE INFLUENCE OF ELECTRIC FIELD STRENGTH ON CORONA CHARACTERISTICS

5.1 The equivalent circuit representing the corona process

Figure 5-1 shows the appearance of rime and glaze ice accreted conductors and their corona discharge when applied voltage was beyond the corona onset voltage. It can be seen from these figures that accreted ice greatly changes the roughness of the conductor. The ice treeing of the rime and the tips of glaze icicles became strong corona sources when the conductor was subjected to enough high voltage.

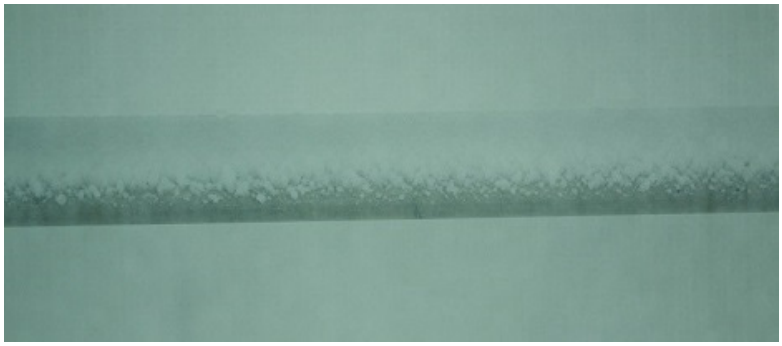

(a) Appearance of rime ice accreted with an electric field of 25 kV_{rms}/cm.

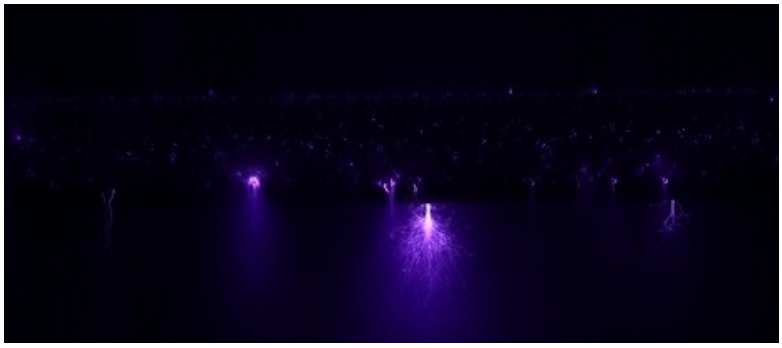

(b) Corona discharge of rime ice accreted conductor.

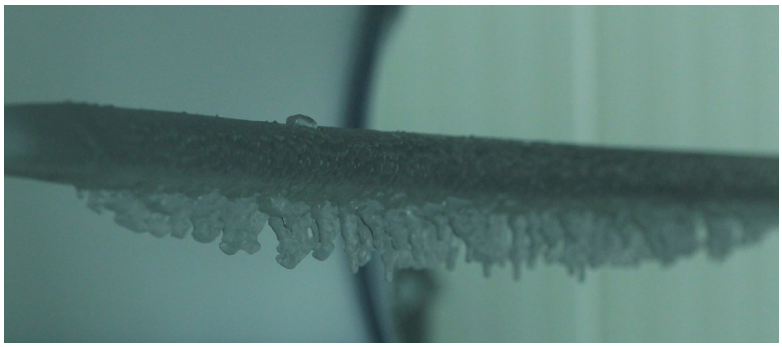

(c) Appearance of glaze ice accreted with an electric field of 25 kV_{rms}/cm.

(d) Corona discharge of glaze ice accreted conductor.

Figure 5-1: Appearance of accreted ice and its corona discharge.

The corona process as well as the capacitance and conductance of the conductor configuration due to corona discharge can be represented by an equivalent circuit, as shown in Figure 5-2. The elements in the equivalent circuit representing the conductor in corona are: C_g, the geometric capacitance of the conductor-cage configuration; C_n, the additional non-linear capacitance caused by the presence of corona; and G_c, the non-linear leakage conductance mainly contributing the corona loss. When the applied voltage is below the corona onset voltage, $C_n = 0$ F and $G_c = 0$ S, theoretically.

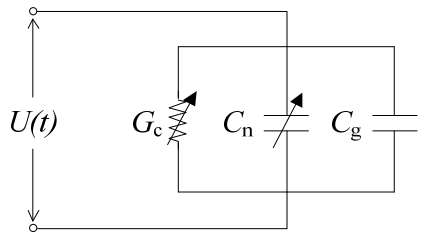

Figure 5-2: The equivalent circuit representing the corona process from the conductor-cage configuration.

5.2 The influence of electric field strength on corona loss

When the transmission line is covered with ice, its surface becomes rough. This gives a decreased corona onset voltage and makes the CL significant even if the transmission line is running under operating voltage. As the electric field on and near the ice treeing and glaze tips is much higher than that in fair weather condition, ice treeing and glaze become strong corona discharge sources.

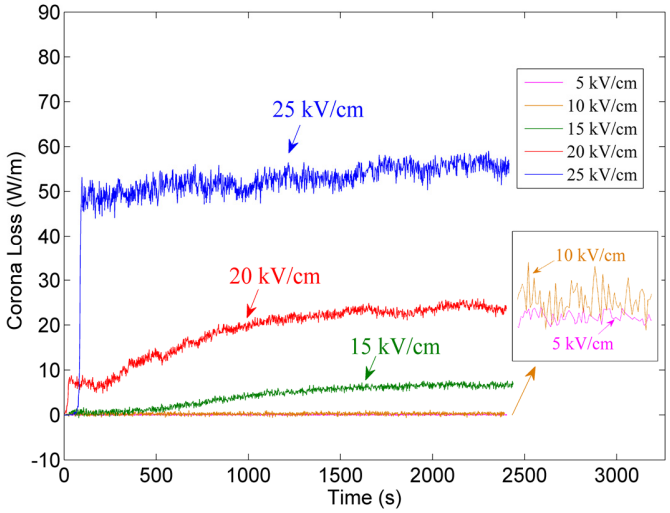

Figure 5-3: Corona losses at different electric field strengths during rime accretion with wind velocity of 2 m/s and conductivity of 50 µS/cm.

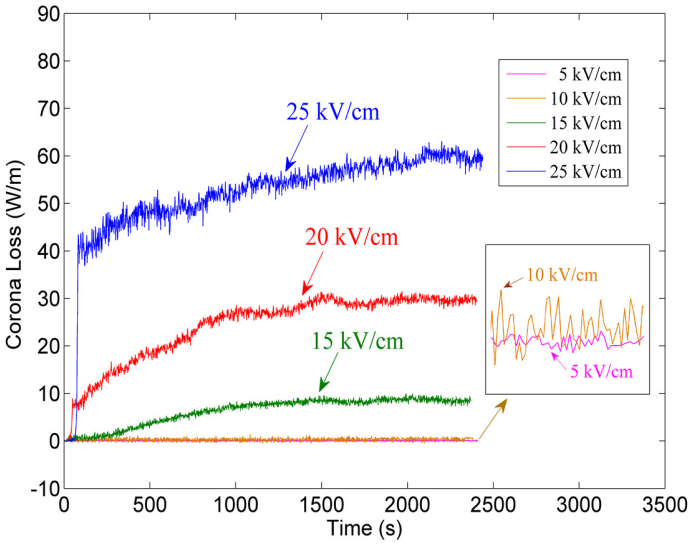

Figure 5-4: Corona losses at different electric field strengths during rime accretion with wind velocity of 3 m/s and conductivity of 50 µS/cm.

Figures 5-3 and 5-4 show CL with the conductor energized by various electric field levels ranging from 5 to 25 kV_{rms}/cm during rime accretion at different wind velocities. From both figures, it can be seen that when the surface electric field is less than 10 kV_{rms}/cm, CL is negligible during the whole accretion period. When the surface electric field is higher than 15 kV_{rms}/cm with a wind velocity of 2 m/s, CL is increasing gradually and then becomes stable after 30 minutes of accretion. This can be explained by the fact that when a water droplet is exposed to an electric field, it becomes polarized. This polarization induces an electric force on the dipole which always points to a higher electric field [101]. From equation (4.7), it can be derived that the electric field near the conductor is proportional to $1/r$ which means that the electric force always tends to attract a droplet moving toward the conductor. As the conductor surface is smooth at the beginning, the surface roughness of the conductor will be dramatically increased with accreted rime, leading to an increasing CL during the first 30 minutes. With the time is elapsed further, the surface roughness will increase very slowly. With higher surface roughness, the CL should also increase slowly. However, if rime is accreted, the equivalent radius of the conductor is also increased, making the electric field surface decrease with time. The mixture of these two opposite effects leads to a stable CL after 30 minutes of rime accretion.

At a wind velocity of 3 m/s, the collision efficiency of water droplets is increased compared with a 2 m/s velocity. Collision efficiency is a dominant factor for rime accretion as higher collision efficiency leads to a higher rime accretion speed and a rougher surface in the windward of the conductor. This is exhibited from the comparison of Figures 5-3 and 5-4. Before the stabilization of CL, with a higher wind velocity, the CL increases with a higher slope in Figure 5-4 than in Figure 5-3, with the same surface electric field. When CL becomes stable, CL with wind velocity of 3 m/s is also higher. CLs at the end of 40 minutes of rime accretion are shown in Table 5-1. In Table 5-1, CL_1 and CL_2 are the CL when the wind velocity is 2 m/s and 3 m/s respectively. When the electric field is 5 kV_{rms}/cm, both CLs are negligible. With the surface electric fields increases, CL increases dramatically. However, the ratio of CL_2 and CL_1 is decreasing. When the surface electric field is 25 kV_{rms}/cm, CL_2 is only 6.9% percent higher than CL_1. This can be explained by the fact that when the electric field is near or above the corona onset gradient, corona wind is generated. As the trajectory of water droplets is determined by the

combination of corona wind and external wind velocities, thus, the effect of higher external wind velocity, which tends to increase the collision efficiency, is weakened by the generated corona wind which expels the water droplets and decreases the collision efficiency.

Table 5-1: Comparison of Corona Losses after 40 Minutes of Rime Accretion at Different Wind Velocities

	5 kV_{rms}/cm	**10 kV_{rms}/cm**	**15 kV_{rms}/cm**	**20 kV_{rms}/cm**	**25 kV_{rms}/cm**
CL_1 (W/m) V = 2 m/s	0.03	0.35	6.7	23.5	55.4
CL_2 (W/m) V = 3 m/s	0.06	0.48	8.5	29.6	59.2
SD_1 (W/m) V = 2 m/s	0.08	0.28	0.43	0.62	1.09
SD_2 (W/m) V = 3 m/s	0.10	0.32	0.44	0.62	1.37
CL_2/ CL_1 (%)	200	137	127	126	107

The standard deviations (SD) of CLs are also shown in Table 5-1. It can be seen that SD increases with an increase of electric field. With the electric field the same, SD is higher when the velocity is 3 m/s compared with that of 2 m/s.

It was observed that the conductivity has little effect on CL during rime accretion. CL curves with accretion time are almost identical when conductivities are 50 and 200 μS/cm with all other parameters the same. This is reasonable as rime is dry-grown ice, high water conductivity will not intensify the corona discharge.

Glaze ice accretion was also investigated in this paper as shown in Figure 5-5 with wind velocity of 2 m/s. From this figure, it can be seen that when the surface electric field is 10 kV_{rms}/cm, CL cannot be neglected anymore.

For glaze ice, in contrast to rime ice, freezing water conductivity had a moderate influence on CL. With all other parameters kept the same during glaze accretion, CL increases as conductivity is increased. The CL measurements at the end of 40 minutes of glaze ice accretion are shown in Table 5-2. In Table 5-2, CL_3 and CL_4 are the CL when the water conductivity is 50 μS/cm and 200 μS/cm, respectively. It can be seen from this table that the ratio of CL_4 and CL_3 is decreasing with an increase

of surface electric field. When the surface electric field is 25 kV_{rms}/cm, CL_4 and CL_3 are almost the same. The CLs are also compared between rime and glaze ice conditions. When the electric fields are in a range of between 10 and 25 kV_{rms}/cm, the CL under glaze condition is 2.44 to 23.1 time higher than that of rime condition at the same surface electric field level. Thus, it can be concluded that the transmission line experiences higher CL in the condition of glaze ice than rime. The SD for glaze ice is also listed in Table 5-2. CL and SD of glaze ice have the same trend with that of CL for rime when the electric field is increased. With an electric field strength higher than 5 kV_{rms}/cm, CL and SD for glaze ice with water conductivity of 200 µS/cm are higher than that of 50 µS/cm.

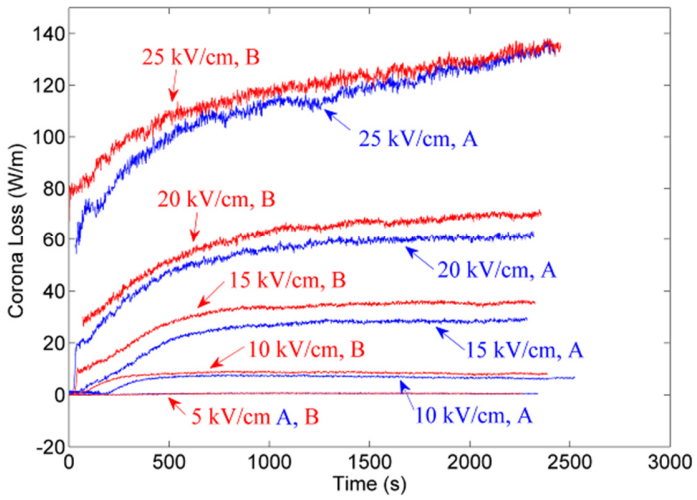

Figure 5-5: Corona losses at different electric field strengths during glaze accretion with wind velocity of 2 m/s and conductivity of 50 and 200 µS/cm (A and B stand for conductivities of 50 and 200 µS/cm).

Table 5-2: Comparison of Corona Losses after 40 Minutes of Glaze Ice Accretion at Different Wind Velocities

	5 kV_{rms}/cm	**10 kV_{rms}/cm**	**15 kV_{rms}/cm**	**20 kV_{rms}/cm**	**25 kV_{rms}/cm**
CL_3 (W/m) 50 µS/cm	0.54	6.5	29.0	61.4	133.7
CL_4 (W/m) 200 µS/cm	0.73	8.1	35.7	69.9	135.2
SD_3 (W/m) 50 µS/cm	0.11	0.20	0.42	0.81	1.49
SD_4 (W/m) 200 µS/cm	0.10	0.23	0.47	0.82	1.79
CL_4/ CL_3 (%)	135	125	123	114	101

As CL is closely related to the configuration of the transmission line, it is difficult to compare the CL level with different transmission lines or corona cage setups directly, even with the same environmental parameters and conductor surface electric field. To convert CL of one configuration to that of another configuration, the equivalent CL must be adjusted by a reduction coefficient *K*

$$CL_b = K_b CL_n = K_b \frac{CL_a}{K_a} \tag{5.1}$$

where subscripts *a* and *b* denote the two different configurations.

Reduction coefficient K is defined in [6]

$$K = \frac{f}{50\,Hz}(nr_{sc}\beta)^2 \frac{\log(R/R_b)\cdot\log(\rho/R_b)}{\log(R_z/\rho)} \tag{5.2}$$

where *f* is the frequency (60 Hz), *n* is the number of subconductors in the bundle, r_{sc} is the subconductor radius (cm), β equals to $1+0.301/\sqrt{\delta r_{sc}}$, δ is the relative air density, R_z is the equivalent zero-potential cylinder radius (cm), R_b is the equivalent radius of the bundle (cm), and ρ is defined as $18\sqrt{r_{sc}}$ for single conductors and $18\sqrt{nr_{sc}+4}$ for bundle conductors with r_{sc} in cm.

The test results using the corona cage are compared with those measured on a full-scale test line. The test line is a single circuit operating at 1000 kV and consists of 8 Aluminium Conductor Steel Reinforced (ACSR) cable LGJ-500/35 per bundle [19]. The schematic diagram of the tower is illustrated in Figure 5-6. The average height of phase A and C is 30 m and the conductor surface electric field strength for the side phases and middle phase are 14.19 kV_{rms}/cm 14.67 kV_{rms}/cm, respectively.

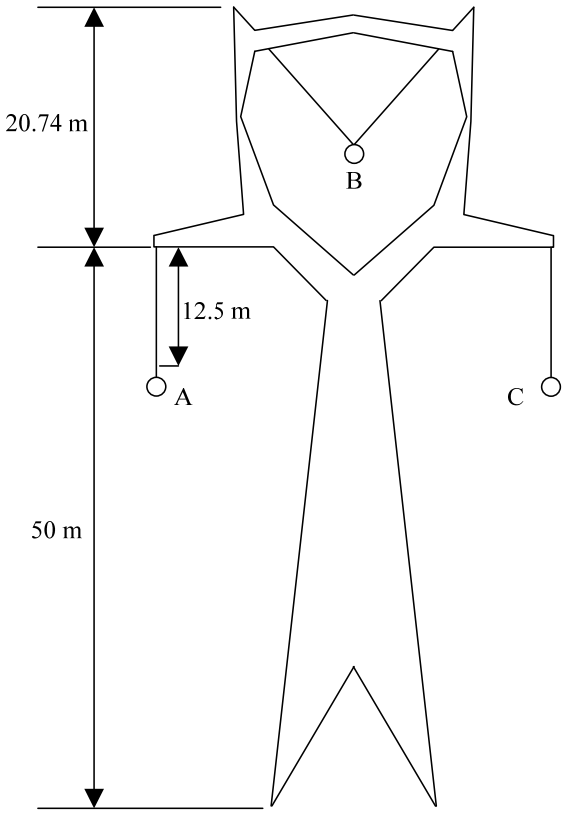

Figure 5-6: The schematic diagram of the test line tower

Based on the values in Table 5-2, the relationship between *CL* and conductor surface electric field *E* is fitted. As the conductor surface electric field is normally higher than 10 kV_{rms}/cm, *CL* only in the range of 10 kV_{rms}/cm and 25 kV_{rms}/cm is considered.

For conductivity of 50 μS/cm

$$CL = 0.04 \times E^3 - 1.602 \times E^2 + 25.55 \times E - 128.8 \quad (5.3)$$

For conductivity of 200 μS/cm

$$CL = 0.032667 \times E^3 - 1.338 \times E^2 + 23.453 \times E - 125.3 \quad (5.4)$$

Substituting 14.19 kV_{rms}/cm into (5.3) and (5.4) yields 25.5 W/m and 31.4 W/m respectively. Table 5-3 gives a comparison between the calculated equivalent CL_{eqs} on this transmission line originating from CL results of the present study and the measured CL_{ls} on the side phase of the AC test line under wet snow condition. The measured CL_{ls} on the side phase of the test line is 53.5 W/m and the reduction coefficients K_{ls} and K_c of the transmission line side phase and the corona cage are 54.9 and 23.3, respectively. As shown in Table 5-3, the ratio of CL_{eqs} and CL_{ls} is 112.1% and 137.9% when the water conductivity is 50 μS/cm and 200 μS/cm, respectively. Consider the conductor surface roughness is rougher under glaze condition than that under wet snow, the higher CLs are reasonably expected.

Table 5-3: Comparison of Corona Losses Measured on a Transmission Line and Calculated Equivalent CLs Originated from Corona Cage.

CL_c (W/m)	K_{ls}/K_c	CL_{eqs} (W/m)	CL_{ls} (W/m)	CL_{eqs}/CL_{ls}
25.5 (50 μS/cm)	2.35	60.0	53.5	112.1%
31.4 (200 μS/cm)	2.35	73.8	53.5	137.9%

There are many sources of power loss in transmission systems: substation loss, resistive or ohmic loss, and corona loss, etc. The power losses affect mainly the operating costs and should therefore be optimized with regard to investment cost of the line conductors at the given voltage level. According to the Department of Energy, California lost about 19.7×10^9 kWh of electrical energy through transmission/distribution in 2008 [111]. This amount of energy loss was equal to 6.8% of total amount of electricity used in the state throughout that year. At the 2008 average retail price of $0.1248/kWh, this amounts to a loss of about $2.4B worth of electricity in California, and a $24B loss nationally. In a comparative analysis of operational losses of EHV and UHV transmission system [112], Geng concluded that, for 1000 kV AC transmission systems, the substation loss is about 0.06%~0.09% of the total capacity and the resistive loss normally consists of 35%~75% of the total loss.

Due to the importance of power loss in transmission lines, a comparison of resistive loss and corona loss is discussed below based on the test line configuration mentioned above. It may give a picture of corona loss on UHV transmission line under glaze ice condition and some guidelines on the design of the transmission line in cold region.

Table 5-4 shows the calculated equivalent corona loss on the side phase (CL_{eqs}), equivalent corona loss on middle phase (CL_{eqm}) and the total equivalent corona loss (CL_t) of the 1000 kV AC test line. In Table 5-4, the calculation is based on the test results in Table 5-2 when the water conductivity is 200 μS/cm. When the side phase is subjected to conductor surface electric field E_{ls}, the conductor surface electric field applied on the middle phase is $1.03 \cdot E_{ls}$ due to tower configuration [19]. To calculate CL_{eqm}, we assume that the reduction coefficient of the middle phase K_{lm} is the same as that of the side phase K_{ls}. Then, CL_{eqm} can be obtained by substituting $1.03 \cdot E_{ls}$ into (5.4) and then multiplying it by K_{lm}/K_c. As the corona loss when the conductor surface electric field was subjected to 5 kV_{rms}/cm is negligible, only equivalent corona losses from 10 kV_{rms}/cm to 25 kV_{rms}/cm on the 1000 kV AC test line are calculated.

Table 5-4: Corona Loss Conversion from Corona Cage to a 1000 kV AC test line when the side phase is subjected to various electric field strengths.

E_{ls}	10 kV_{rms}/cm	15 kV_{rms}/cm	20 kV_{rms}/cm	25 kV_{rms}/cm
CL_c (W/m)	8.1	35.7	69.9	135.2
CL_{eqs} (W/m)	19.0	83.9	164.3	317.7
CL_{eqm} (W/m)	23.5	89.6	177.7	350.6
CL_t (W/m)	61.5	257.4	506.3	986.0

The total resistive loss (P_{RL}) of the transmission line can be calculated as follows

$$P_{RL} = 3mI_p^2 R_p \tag{5.5}$$

where m the number of circuit, I_P is the phase current in A, and R_P is the phase resistance in Ω. I_P can be expressed as

$$I_P = \frac{P_P}{U_P} = \frac{\frac{P_0}{3m}}{\frac{\sqrt{3}}{3}U_0} = \frac{P_0}{\sqrt{3}mU_0} \tag{5.6}$$

R_P can be calculated by

$$R_P = R_{UP}L = \frac{R_{USub}}{n}L \tag{5.7}$$

where R_{UP} is the phase resistance per meter in Ω/m, R_{USub} is sub-conductor resistance per meter in Ω/m, n is the number of sub-conductors in the bundle, and L is the length of the transmission line in m.

Substituting (5.6) and (5.7) into (5.5) yields

$$P_{RL} = R_{UP}L = \frac{P_0^2 R_{USub} L}{mnU_0^2} \tag{5.8}$$

For the LGJ-500/35, the sub-conductor resistance per unit meter is 0.05812 Ω/km [113]. Then, the resistive loss can be obtained by replacing the variables in (5.8) by the parameters of the transmission line and power capacity. The resistive loss and its comparison with corona loss under glaze condition are listed in Table 5-5 for different power capacities and distances. It can be seen that the percent of corona loss in transmission line decreases with increasing power capacity. When the conductor surface electric field is 10 kV_{rms}/cm, the corona loss is 11.9%~27.1% of the resistive loss. This percentage of corona loss is not a big problem for the transmission lines. When the electric field is increased to 15 kV_{rms}/cm, the ratio of corona loss and resistive loss is 1.13 and 0.50 at power capacities of 5600 MV and 8400 respectively. The sum of corona loss and resistive loss can be up to 9.16% of the total capacity distributed when the distance is 1000 km. This is close to the average line losses on most US grid which is in the range of 6% to 10%. When the electric field is 20 kV_{rms}/cm, the corona loss is higher than resistive loss for all power capacities listed in Table 5-5. When the electric field is 25 kV_{rms}/cm, the combined loss by resistance and corona is 10.7%~21.7% of the distributed energy for distance longer than 400 km. Thus, in cold region where glaze ice happens often, the conductor surface electric field should be chosen carefully for long distance transmission lines due to economical reason.

Table 5-5:. Resistive and Corona Loss Percentage of 1000 kV AC Single-circuit Three-phase Transmission Lines under glaze condition

***L* (km)**	***P*₀ (MV)**	**Resistive Loss**		**Corona Loss (%)**			
		(W/m)	**(%)**	**10 kV_{rms}/cm**	**15 kV_{rms}/cm**	**20 kV_{rms}/cm**	**25 kV_{rms}/cm**
400	5600	227.8	1.63	0.44	1.84	3.62	7.04
	7200	376.6	2.09	0.34	1.43	2.81	5.48
	8400	512.6	2.44	0.29	1.23	2.41	4.70
600	5600	227.8	2.44	0.66	2.76	5.42	10.56
	7200	376.6	3.14	0.51	2.15	4.22	8.22
	8400	512.6	3.66	0.44	1.84	3.62	7.04
800	5600	227.8	3.25	0.88	3.68	7.23	14.09
	7200	376.6	4.18	0.68	2.86	5.63	10.96
	8400	512.6	4.88	0.59	2.45	4.82	9.39
1000	5600	227.8	4.07	1.10	4.60	9.04	17.61
	7200	376.6	5.23	0.85	3.58	7.03	13.69
	8400	512.6	6.10	0.73	3.06	6.03	11.74

5.3 The influence of electric field strength on corona onset voltage

When the wind velocity is 2m/s and freezing water conductivity is 50 μS/cm, CL curves against voltage are shown in Figures 5-7 and 5-8 for the rime and glaze accretion. According to Peek and Harding's researches, CL throughout the higher range of applied voltage follows a quadratic law [13][43]

$$CL = k(V - V_0)^2 \tag{5.9}$$

where CL is in kW/km or W/m, k is a coefficient determined by given weather and surface condition, V is the applied voltage on the test conductor in kV, and V_0 is the corona onset voltage for given weather and surface conditions in kV.

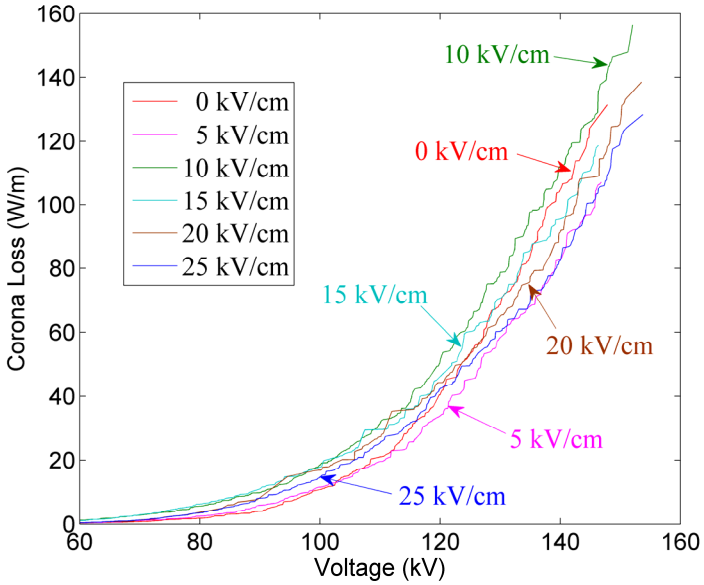

Figure 5-7: Corona losses vs. voltage at different electric field strengths for rime accretion.

From equation (5.9), it can be seen that onset voltage is a very important factor for conductor corona performance. To find out the onset voltage for each curve, (5.9) can be rewritten as

$$\sqrt{CL} = \sqrt{k}\,|V - V_0| \tag{5.10}$$

Thus, $\sqrt{CL}$ is in a linear relationship with applied voltage V at the higher range of applied voltage.

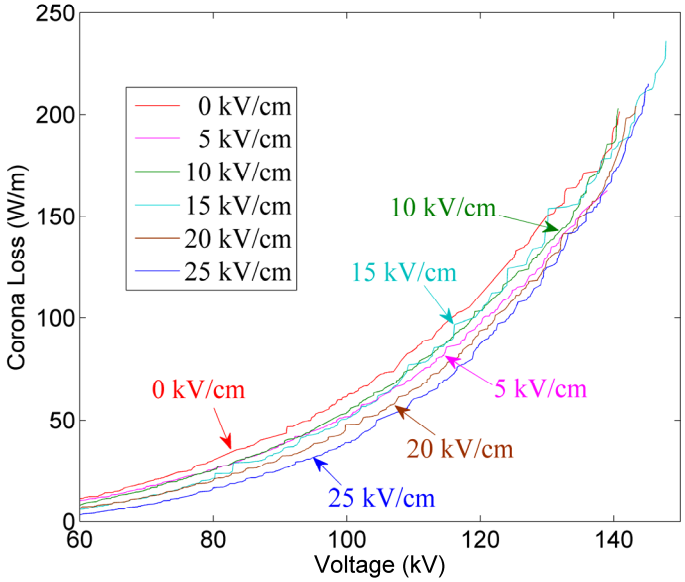

Figure 5-8: Corona losses vs. voltage at different electric field strengths for glaze accretion.

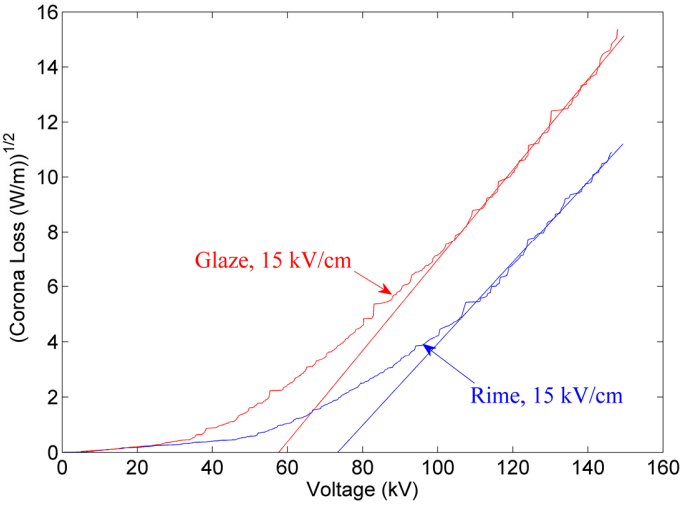

Figure 5-9: Corona losses – quadratic analysis.

To illustrate how to get onset voltage, $\sqrt{CL}$ is plotted with V in Figure 5-9 where the straight lines in the higher range of voltages demonstrates that the quadratic law applies to onset voltage as shown by the intercept for zero CL, indicated in the figure.

Table 5-6: Comparison of Corona Onset Voltages (V_0) after 40 Minutes of Rime Accretion.

	0 kV_{rms}/cm	**5 kV_{rms}/cm**	**10 kV_{rms}/cm**	**15 kV_{rms}/cm**	**20 kV_{rms}/cm**	**25 kV_{rms}/cm**
V_0 (kV)	83.7	80.5	75.6	73.3	72.2	74.0
k	0.032	0.023	0.027	0.022	0.021	0.020

Table 5-7: Comparison of Corona Onset Voltages (V_0) after 40 Minutes of Glaze Accretion.

	0 kV_{rms}/cm	**5 kV_{rms}/cm**	**10 kV_{rms}/cm**	**15 kV_{rms}/cm**	**20 kV_{rms}/cm**	**25 kV_{rms}/cm**
V_0 (kV)	48.9	51.5	52.7	57.6	62.3	67.4
k	0.023	0.021	0.023	0.027	0.028	0.032

The calculated onset voltages for rime and glaze accretion are given in Tables 5-6 and 5-7, respectively. From Table 5-6, it can be seen that onset voltage is highest when there is no voltage applied during the rime accretion process. As the electric field increases, more rime is accreted on the windward side of the conductor because of the dielectrophoretic force on the polarized water droplets, leading to a decrease of onset voltage. However, when the electric field is increased further from 20 kV_{rms}/cm to 25 kV_{rms}/cm, onset voltage increases. This is because the corona wind velocity generated by the high electric field strength is comparable with wind velocity. This corona wind expels the water droplets, thus decreasing the collision efficiency. While onset voltage is to shift the curve, k can be used to describe the change of the shape. It can be seen from Table 5-6 that k decreases with an increase in electric field. It means that when the test voltages are beyond their corona onset voltages, the CL of rime accreted at lower electric field strength during accretion increases faster than that accreted at higher electric field strength. As shown in Figure 4-1, there are many protuberances visible growing on the surface of rime 4-1(a). Although rime 4-1(a) has a higher onset voltage, when the test voltage is beyond its onset voltage, all the protuberances are potential corona discharge sources, leading to a higher k. When the rime is accreted in the presence of an electric field, it can be seen from (b) to (f) of Figure 4-1 that there exists

an increasing belt of water film in the windward side of the conductor because of Joule heat. This water film reduces the protuberances and decreases the corona discharge sources, thus leading to a lower *k*.

For glaze ice accretion, as shown in Table 5-7, onset voltage increases as electric field is increased during the accretion over the whole range of electric field strength. This is evident as the length of icicles is decreasing with an increase of electric field because of Joule heat as shown in Figure 5-5. With a conductive water film present on the surface, the tips of longest icicles have the most deformed electric fields. It can also be seen from Table 5-7 that the coefficient *k* has an increasing trend as electric field is increased.

There are two reasons for that. The first reason is the change in surface roughness. From the appearance of the glaze in Figure 4-2, it can be seen that when the accretion electric field strength is lower, the conductor and icicle surface is smoother and the conically-shaped icicles are the only major corona discharge sources. As the electric field increases, the electric field on and near the conductor influences the accumulation of ice and makes the conductor surface much rougher. When the electric field is higher than 20 kV_{rms}/cm, the icicles are not conically-shaped any more. They become flat and are fan-shaped with many tips in the windward direction as shown in Figure 4-2f. Conductor surfaces and icicle tips are all potential corona discharge sources as shown in Figure 5-1d. The second reason is the spacing of icicles. The spacing results are shown in Table 4-5. The results show that the icicle spacings decrease as electric field increases. As the spacing becomes smaller, more icicles will be formed for the same conductor length, leading to increasing sources of corona discharge.

In [40], Hegy concluded that the corona loss against the voltage curve is shifted in the voltage direction by variations in pressure and temperature, for a smooth conductor with unchanged curve shape. However, with onset voltage and *k* changing, the present paper shows that when rime or glaze is accreted, not only the curve is shifted but also the shape is changed as well.

For a given conductor and ice shape, onset voltage varies for different dimension parameters such as conductor diameter and cylindrical corona cage. It is also different in real transmission lines for single and bundle configurations. To further describe the influence of electric field strength on onset voltage, the surface irregularity is calculated.

Surface irregularity results from overall effects of corona behavior during various weather conditions. It not only reflects the actual change of conductor surface as it is wet by water droplets or covered by rime or glaze, but also reflects the effects of ambient environment. For example, it also takes into account those corona discharges that originate from the water droplets in the immediate vicinity of conductor without actually touching it.

In the present study, onset voltage V_o (kV) of a cylindrical conductor placed in another coaxial cylindrical cage can be derived from Peek's formula and equation (2.1)

$$V_o = 21.1 \times r_c \times \ln(R / r_c) \times m \times \delta \times (1 + \frac{0.308}{\sqrt{\delta r_c}}) \tag{5.11}$$

where m is a conductor surface irregularity factor which is the ratio of corona onset gradient of contaminated, iced or wetted conductor to that of a dry smooth conductor with the same diameter, δ is the relative air density. The latter is given as a function of atmospheric pressure P (kPa) and ambient temperature T (℃) by

$$\delta = \frac{P}{P_0}(\frac{273+T_0}{273+T}) \tag{5.12}$$

where P_0 is the pressure at sea level of 101.3 kPa, P in kPa can be obtained from meteorological stations in the vicinity of the laboratory, and T_0 is the reference temperature of 25 ℃.

Given the radii of the conductor and the meshed cylinder r_c = 1.6 cm and R = 50 cm and corona onset voltage from Tables 5-6 and 5-7, surface irregularity m can be calculated by equations (5.11) and (5.12). Calculated values of m are given in Tables 5-8 and 5-9. For rime accretion, m ranges between 0.44 and 0.52. The most severe condition happens under glaze ice condition. In this case, with the icicles on the conductor surface, the surface irregularity m can be as low as 0.30.

Table 5-8: Calculated Values of Surface Irregularity (*m*) after 40 Minutes of Rime Accretion (-15 °C).

	0 kV_{rms}/cm	5 kV_{rms}/cm	10 kV_{rms}/cm	15 kV_{rms}/cm	20 kV_{rms}/cm	25 kV_{rms}/cm
P (kPa)	99.6	100.0	100.5	100.8	100.3	100.1
m	0.52	0.49	0.46	0.45	0.44	0.45

Table 5-9: Calculated Values of Surface Irregularity (*m*) after 40 Minutes of Glaze Accretion (-8 °C).

	0 kV_{rms}/cm	5 kV_{rms}/cm	10 kV_{rms}/cm	15 kV_{rms}/cm	20 kV_{rms}/cm	25 kV_{rms}/cm
P (kPa)	101.6	99.8	100.2	98.5	100.5	101.3
m	0.30	0.32	0.33	0.37	0.39	0.42

5.4 The influence of electric field strength on leakage conductance

The non-linear leakage conductance per unit length G_{uc} of the conductor-cage configuration can be defined as

$$G_{uc} = \frac{G_c}{l} = \frac{P_{CL}}{U_m^2} \tag{5.13}$$

where l is the length of the measurement section of the corona cage in m, P_{CL} (W/m) is the corona loss, and U_m (V) is the voltage applied on the conductor.

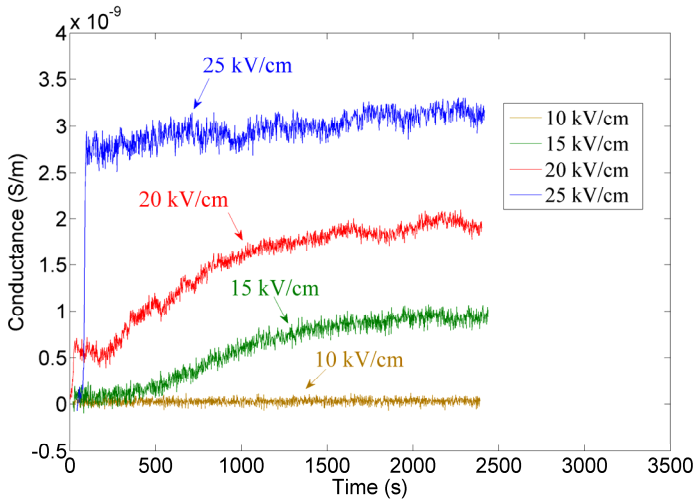

Figure 5-10: Measured G_{uc} during rime accretion process at different conductor surface electric field strengths.

The non-linear leakage conductance per unit length G_{uc} during ice accretion on the conductor is shown in Figures 5-10 and 5-11. Under both rime and glaze ice conditions, with increasing electric field, corona discharge activity intensifies and conductance increases. As shown in Table 5-6, under rime condition, the corona onset voltages are 75.6 kV and 73.3 kV after 40 minutes of rime accretion when the conductor is energized at electric fields of 10 kV_{rms}/cm and 15 kV_{rms}/cm respectively, which corresponds to conductor surface electric fields of 13.7 kV_{rms}/cm and 13.3 kV_{rms}/cm. Therefore, G_{uc} is almost zero when the electric field is 10 kV_{rms}/cm and is appreciable when the electric field is 15 kV_{rms}/cm, as shown in Figure 5-10. With the electric field increased up to 25 kV_{rms}/cm, G_{uc} is increased to 3.12 nS/m.

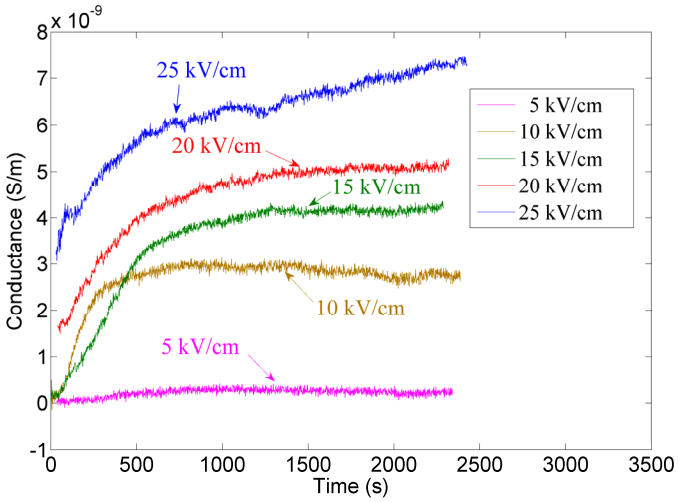

Figure 5-11: Measured G_{uc} during glaze ice accretion process at different conductor surface electric field strengths.

Under glaze ice condition, the corona onset voltages are 51.5 kV and 52.7 kV after 40 minutes of glaze ice accretion at electric fields of 5 kV_{rms}/cm and 10 kV_{rms}/cm respectively, which are equivalent to conductor surface electric fields of 9.3 kV_{rms}/cm and 9.5 kV_{rms}/cm. This is confirmed by the calculated G_{uc}, as shown in Figure 5-11. When the conductor is energized at 5 kV_{rms}/cm during ice accretion, which is far below the corona onset strength, G_{uc} is zero. However, when the conductor is energized at 10 kV_{rms}/cm, which is a little higher than its corona onset strength, G_{uc} increases sharply at the beginning of the glaze ice accretion to reach a value of 2.51 nS/m after 5 minutes of ice accretion. When the electric

field is increased up to 25 kV_{rms}/cm during ice accretion, G_{uc} is 7.34 nS/m. It can be seen from the above discussion that the Measured G_{uc} results are consistent with the measured corona onset voltages.

A comparison of G_{uc} after 40 minutes of rime and glaze ice accretion under different conductor surface electric field strengths is displayed in Table 5-10. With the given applied voltage, G_{uc} is proportional to corona loss as indicated by (5.13). Therefore, the trend of G_{uc} in Table 5-10 is identical with that of corona loss, as shown in Tables 5-1 and 5-2.

Table 5-10: Comparison of Measured G_{uc} under Different Icing Conditions.

	5 kV_{rms}/cm	**10 kV_{rms}/cm**	**15 kV_{rms}/cm**	**20 kV_{rms}/cm**	**25 kV_{rms}/cm**
Rime (nS /m)	0.01	0.14	0.97	1.93	3.14
Glaze ice (nS /m)	0.74	2.72	4.26	5.16	7.30

5.5 The influence of electric field strength on capacitance

The geometry capacitance C_g in Figure 5-2 is composed of two parts. One part, denoted as C_t, comes from the geometry capacitance between the conductor and outer metallic mesh cylinder over the measurement section of the corona cage. The other part which is called stray capacitance C_s, or parasitic capacitance, comes from the capacitance between the conductor in the measurement section and surrounding objects such as the guard sections, the ground, etc.

The conductor, corona cage, and the surrounding air can be regarded as an electrode system and modeled as a capacitor. For an infinite long corona cage, the theoretical geometry capacitance per unit length C_{ut} can be expressed as

$$C_{ut} = \frac{C_t}{l} = \frac{2\pi\varepsilon_0\varepsilon_r}{\ln(R/r_c)} \tag{5.14}$$

where ε_0 is the vacuum permittivity which is 8.854×10^{-12} F/m, ε_r is a dimensionless dielectric constant of air, and l (m) is the length of the measurement section of the corona cage. Given the values of R and r_c at 50 cm and 1.6 cm, respectively, the C_{ut} of the present corona cage is 16.16 pF/m.

As indicated in previous studies [38], with the presence of corona discharge, the apparent value of the total current could be increased by the presence of harmonic current components. However, if the corona loss remains the same, the capacitance can be approximated by the fundamental component. As the third harmonic is negligible in the applied voltage in the present study which will be discussed in section 5.7, the corona loss is mainly contributed by the fundamental part. Therefore, the total capacitance C_a can be calculated by

$$C_a = C_g + C_n = C_t + C_s + C_n = \frac{I_m \sin(\varphi)}{2\pi f U_m} \tag{5.15}$$

where I_m and U_m are the magnitudes of the fundamental current and voltage, φ is the power factor angle between the fundamental components of voltage and current, and f is the fundamental frequency with a value of 60 Hz.

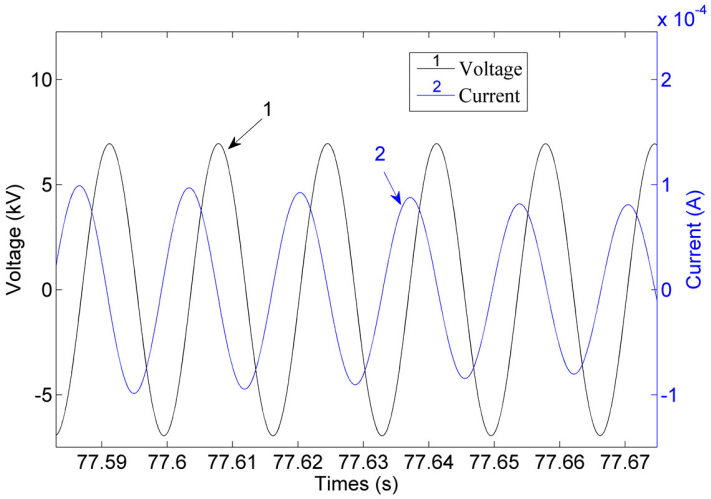

Figure 5-12: Fundamental components of applied voltage and the induced corona current.

When the applied voltage on the conductor is far below its corona onset voltage under fair condition, the additional non-linear capacitance C_n = 0 F. Therefore, the geometry capacitance C_g can be obtained by applying a voltage below corona onset voltage on the conductor. When the applied

fundamental voltage U_m is equal to 4.91 kV, as shown in Figure 5.12, the fundamental current I_m and φ are 7.02×10^{-5} A and 89.5º, respectively. Then, the capacitance C_g is 37.91 pF by (5.15). There is no available formula to calculate the stray capacitance C_s. However, its value can be obtained by the difference of C_g and $l\cdot C_{ut}$. With the measured C_g and calculated C_{ut} above, it can be derived that the stray capacitance C_s is equal to 5.59 pF for the present corona cage.

The ice accretion or water drops on the conductor surface can cause an increase of capacitance when the applied voltage is beyond the corona onset voltage. With an increase of electric field, increase of capacitance can occur even with very low liquid water content (LWC). Increase in capacitance is mainly contributed by two components. The first component is the additional non-linear capacitance C_n due to the space charge phenomenon adjacent to the conductor rather than the change in dielectric constant between conductor and the outer cylinder. The other component C_t is caused by the increase of the equivalent conductor radius because of ice accretion or water drops on the conductor. To focus on the capacitance over the measurement section, the conductor capacitance per unit length C_{ut}, or $(C_t + C_n)$ $/l$ per unit length during the rime and glaze ice accretion is shown in Figures 5-13 and 5-14.

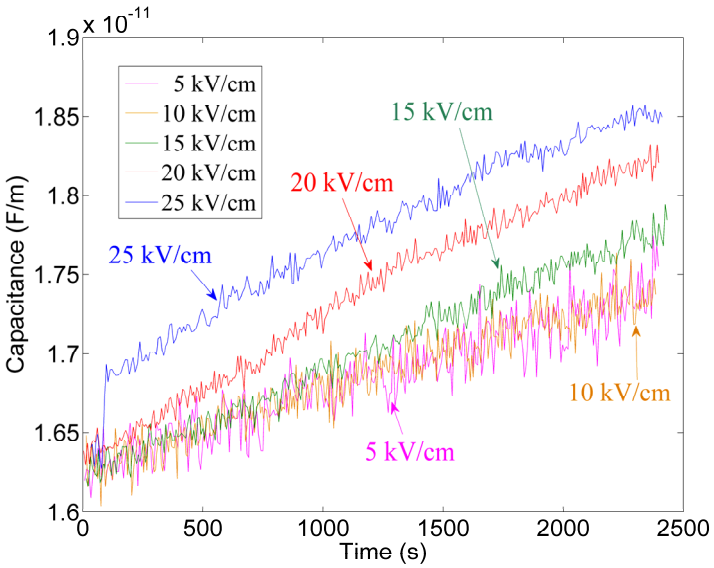

Figure 5-13: Measured C_{uc} during rime accretion at different conductor surface electric field strengths.

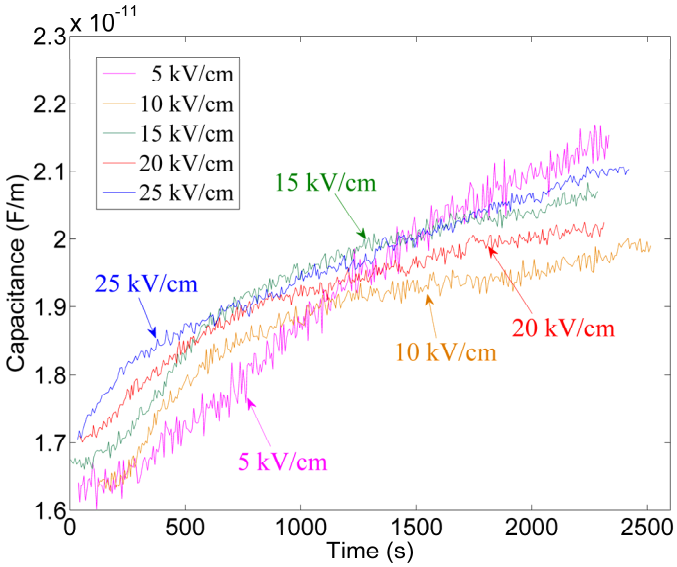

Figure 5-14: Measured C_{uc} during glaze ice accretion at different conductor surface electric field strengths.

From Figure 5-13, it can be seen that when the electric field is less than 20 kV_{rms}/cm, the capacitance per unit length C_{ut} is almost the same as the theoretical value of 16.16 pF/m at the beginning of rime accretion, which means the C_n is negligible. This is expected since corona loss is nearly zero when electric field strength is less than 20 kV_{rms}/cm in the initial stage of rime accretion, as shown in Figure 5-3. As the conductor surface electric field is increased further, the additional non-linear capacitance C_n increases due to corona discharge. The capacitance per unit length C_{ut} also increases during rime accretion as the conductor becomes rougher over time. Under glaze condition, the capacitance per unit length C_{ut} is identical to the theoretical value at the beginning when electric field is less than 15 kV_{rms}/cm. As electric field is increased to 25 kV_{rms}/cm, capacitance per unit length is increased to 1.71 pF/m. However, the change of capacitance per unit length over time is more complex, as shown in Figure 5-14. On one hand, a higher conductor surface electric field leads to a shorter icicle length due to Joule heat, as shown in Table 5-11, leading to a decrease of geometric capacitance. On the other hand, a higher electric field intensifies the corona discharge activity and increases the additional non-linear capacitance C_n.

Table 5-11: Icicle length after 40 minutes of glaze ice accretion when the wind velocity is 2 m/s at different conductor surface electric fields.

	5 kV_{rms}/cm	10 kV_{rms}/cm	15 kV_{rms}/cm	20 kV_{rms}/cm	25 kV_{rms}/cm
l (cm)	11.9	7.4	4.6	3.5	2.2

The corona discharge effectively makes the coronal conductor vary in diameter. The capacitance of an equivalent coronal conductor, which is assumed to be a cylinder, concentrically located with respect to the bare conductor, can be calculated by (5.15). The radii of equivalent coronal conductors after 40 minutes of rime and glaze ice accretion condition at different conductor electric field strengths are plotted in Figure 5-15. Keeping in mind that the actual radius of the bare conductor is 1.6 cm, it can be seen that the radius of equivalent coronal conductor is 1.26 to 1.55 times the radius of the bare conductor under rime condition, as shown in Figure 5-15. Under glaze ice condition, this ratio is 1.91 to 2.32.

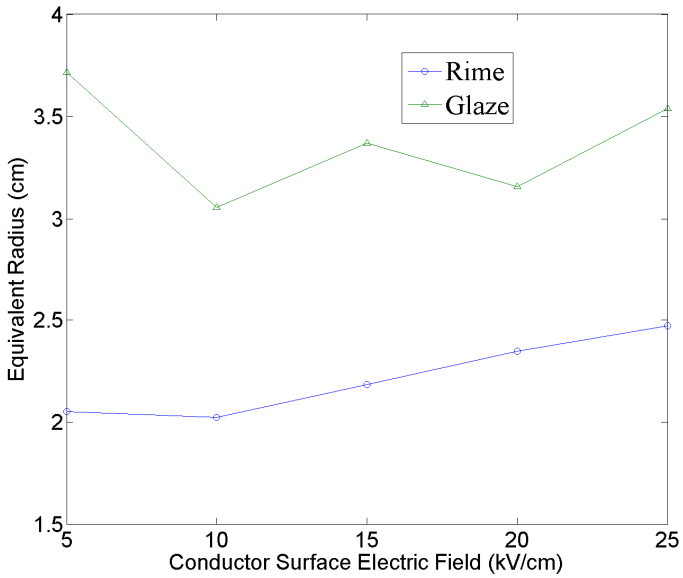

Figure 5-15: Radius of equivalent coronal conductor at different conductor surface electric field strengths.

From the foregoing discussion, it can be concluded that the conductor-cage configuration is mainly characterized by its capacitive nature before the corona onset. When the corona discharge occurs,

the corona cage exhibits a resistive-capacitive nature. With the increase of applied voltage, the configuration becomes more resistive.

5.6 The investigation of harmonics distortion

In harmonic analysis, any wave form can be described mathematically as a series of pure sine waves. These sine waves consist of a fundamental frequency and multiples of that frequency, called harmonics. The absolute values of the harmonic components depend on the magnitude and quality of the applied voltage. The applied voltage and the induced corona current can be expressed as

$$u(t) = \sum_{m=1}^{\infty} U_m \cos(m\omega t + \theta_m) \tag{5.16}$$

$$i(t) = \sum_{n=1}^{\infty} I_n \cos(n\omega t + \varphi_n) \tag{5.17}$$

where U_m, I_n are the magnitudes of the m^{th} and j^{th} harmonic components of voltage and current respectively, and where θ_m and φ_n are the corresponding phase shifts.

Using the FFT method, the harmonic spectrums of voltage and current waveforms can be obtained. Examples of harmonic spectrums are plotted in Figures 5-16 and 5-17.

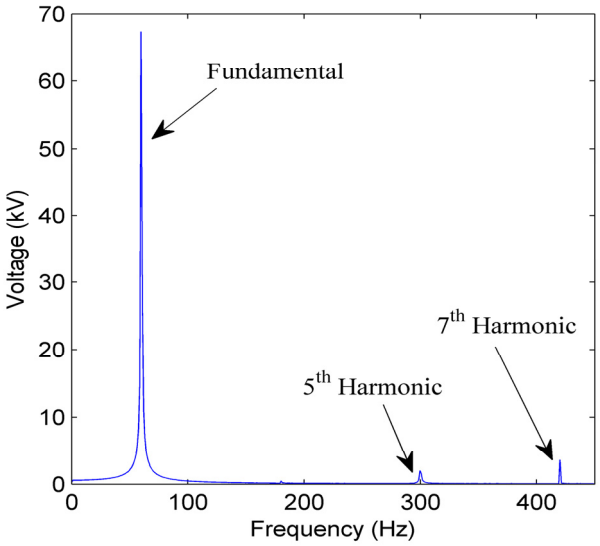

(a) Harmonic spectrum of voltage

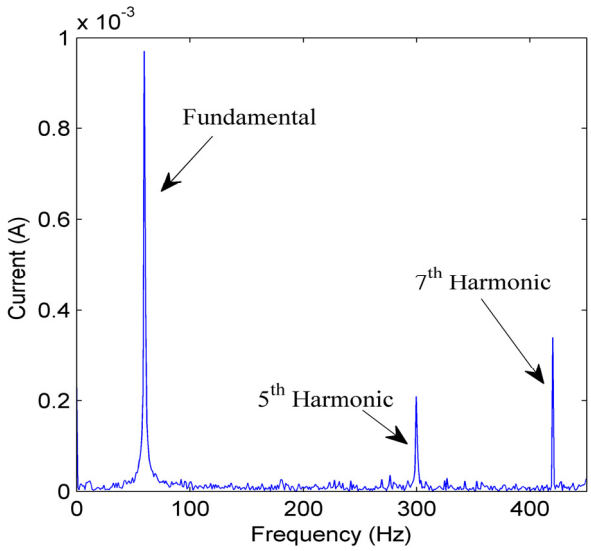

(b) Harmonic spectrum of current

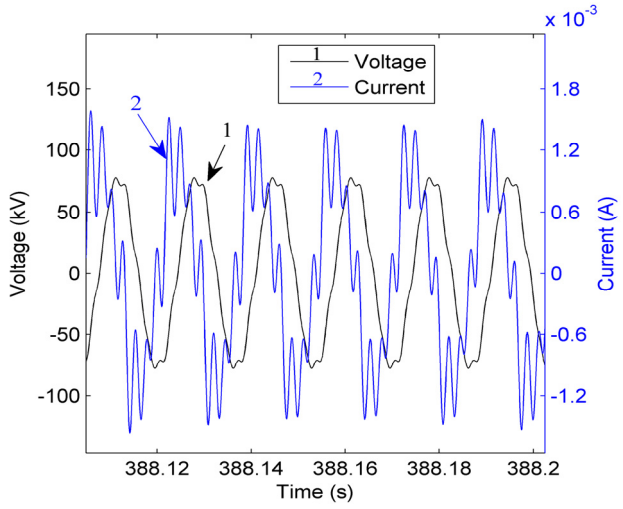

(c) Composite waveforms of voltage and current

Figure 5-16: Voltage and current harmonic spectrums and their composite waveforms after 40 minutes of rime accretion with V = 55.1 kV.

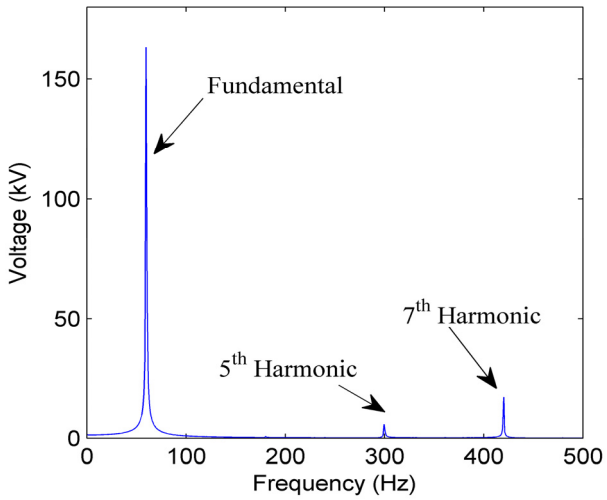

(a) Harmonic spectrum of voltage

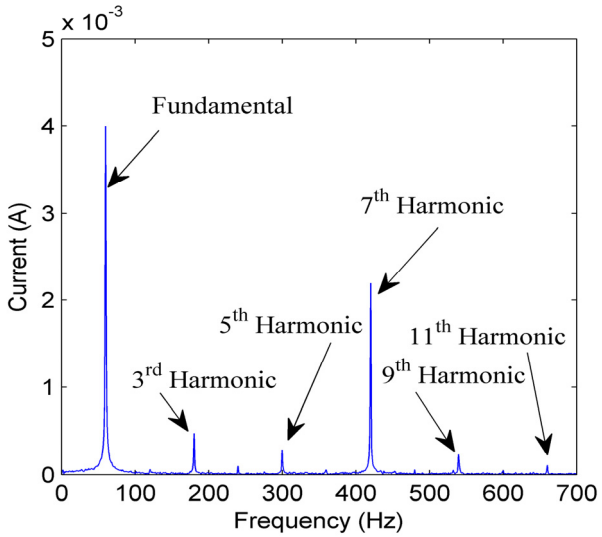

(b) Harmonic spectrum of current

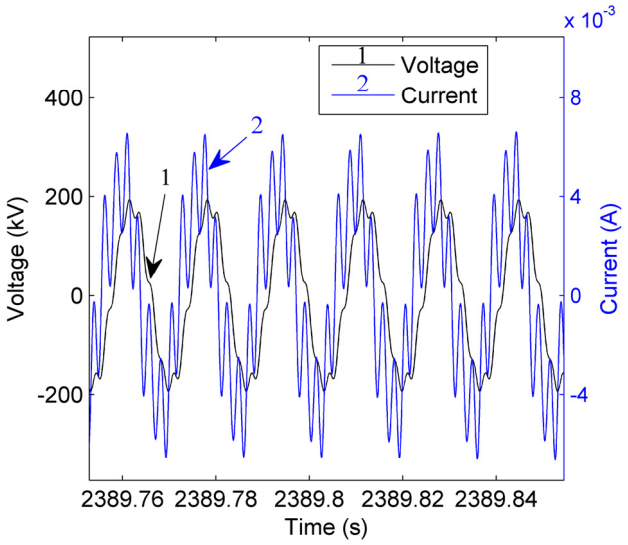

(c) Composite waveforms of voltage and current

Figure 5-17: Voltage and current harmonic spectrums and their composite waveforms after 40 minutes of glaze ice accretion with V = 137.7 kV.

For both voltage and current, the shapes of their positive and negative half waveforms are the same. Therefore, only odd harmonics are contained in the harmonic spectrums. In Figure 5-16, as the

applied voltage is below its corona onset voltage, the magnitude of the 3rd harmonic current component is unnoticeable due to the insignificant 3rd harmonic voltage component presented in the applied voltage. However, when the applied voltage is beyond its corona onset voltage, the 3rd harmonic current component is significant even if the 3rd harmonic voltage component is minor, as shown in Figure 5-17. It can also be seen from harmonic analysis that except for the 5th and 7th harmonic components which are already contained in the voltage waveform, noticeable odd harmonic components of 9th and 11th are also founded in the corona current when the applied voltage is beyond the corona onset voltage. With the existence of harmonic components in both voltage and current, their composite waveforms are obviously not sinusoidal. Due to the significant 5th and 7th harmonic components, the induced corona current has many humps.

As the magnitudes of voltage and current are different in each condition, a good way to compare the decomposition of harmonic components is to use the relative values. Thus, it is assumed that the magnitudes of the fundamental components are one unit and then these of the harmonic components are represented by their ratios. The rime and glaze ice accretion as shown in Figures 5-16 and 5-17 were taken as examples. Table 5-12 lists the percentage of their harmonic components to the fundamental.

Table 5-12: Harmonic components to the corresponding fundamental (%) under rime and glaze ice conditions.

		3rd	**5th**	**7th**	**9th**	**11th**
Rime	Voltage	0.5	3.7	5.1	0.0	0.0
V = 55.1 kV	Current	1.2	21.1	35.7	0.0	0.0
Glaze	Voltage	0.3	3.8	10.1	0.1	0.0
V = 137.7 kV	Current	12.9	8.2	53.5	7.9	3.6

When rime was accreted at 55.1 kV which was below its corona onset voltage, as indicated in Table 5-6, it can be seen that the ratio of the 5th and 7th harmonic current components to the fundamental current were 5.7 and 7.0 times higher than that of their corresponding harmonic voltage counterparts, respectively. When the glaze ice was accreted at 137.7 kV, it is worthy to notice that the introduction of 7th harmonic component which is 10.1% of the fundamental in voltage can lead to a harmonic current component up to 53.5% of the fundamental. Except for the 7th harmonic component which is already

significant in the applied voltage waveform, the magnitude of each individual current harmonics decreases with an increase of harmonic order, dominated by the 3rd, and followed by the 5th, 9th, and 11th harmonics.

To evaluate the harmonic distortion presented and to further characterize the power quality of electric power systems, total harmonic distortion, or THD, is introduced. THD is defined as the ratio of the sum of the powers of all harmonic components to the power of the fundamental frequency, as given by:

$$THD = \frac{\sqrt{A_2^2 + A_3^2 + A_4^2 + \cdots}}{A_1} \tag{5.18}$$

where A_n is the RMS value of voltage or current of n^{th} harmonic and $n = 1$ is the fundamental frequency.

The THD of voltage (THDV) and current (THDC) measured in the experiments are listed in Table 5-13. As the quality of the applied voltage offered is related to many factors such as voltage level, external nonlinear loads, and so on, the THDs of the applied voltages cannot be expected to be the same, even for the same voltage level. Thus, it is meaningful to compare their ratio. As illustrated in Figure 5-18, the ratio of THDC and THDV decreases with an increase of applied voltage, or conductor surface electric field, under rime ice and glaze ice conditions tested.

Table 5-13: *THDV* and *THDC* at different conductor surface electric field strengths under different weather conditions.

	5 kV_{rms}/cm	**10 kV_{rms}/cm**	**15 kV_{rms}/cm**	**20 kV_{rms}/cm**	**25 kV_{rms}/cm**
THDV (rime)	0.0506	0.0632	0.0622	0.0488	0.0895
THDC (rime)	0.3413	0.4149	0.3984	0.3005	0.5393
THDV (glaze)	0.0487	0.0759	0.0437	0.0583	0.1082
THDC (glaze)	0.3188	0.4674	0.2495	0.3312	0.5604

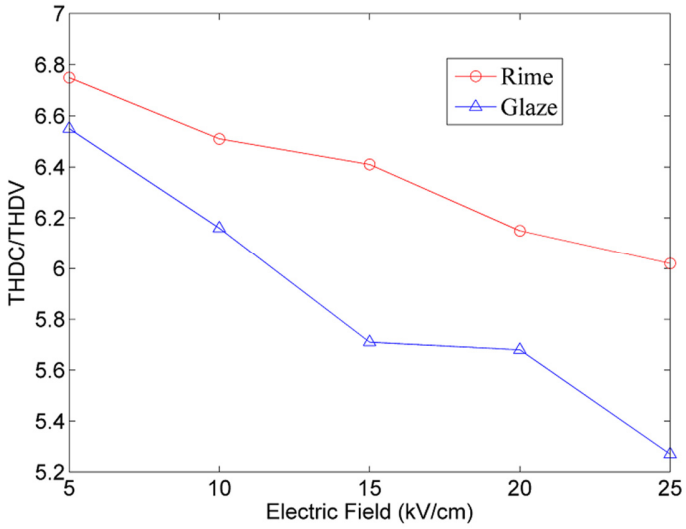

Figure 5-18: Ratio of THDC and THDV at different conductor surface electric strengths under different weather conditions.

5.7 The effect of harmonics on corona loss

As sometimes THDC may approach up to 0.56, as shown in Table 5-13, it is meaningful to investigate the effects of harmonics on corona losses. Ideally, when the harmonics in the supply voltage are filtered before it is applied to the conductor in the absence of corona phenomena, the applied voltage and produced current waves are pure sinusoidal functions. Assuming that the voltage and the corresponding current waves are represented by $u(t) = U_m\cos(\omega t+\varphi_1)$ and $i(t) = I_m\cos(\omega t+\varphi_2)$ respectively, where U_m and I_m are the amplitude of voltage and current, φ_1 and φ_2 are the phase angles of the voltage and current, $\omega = 2\pi f$ is the angular frequency, and f is the power frequency (60 Hz in the present paper). Then, the corona loss is given by the following formula

$$P = \frac{1}{T}\int_0^T u(t)i(t)dt \tag{5.19}$$

where term T is the period with a value of 1/60 s. By averaging the product of $u(t)$ and $i(t)$, which is a sinusoidal function, over period T, corona loss P can be expressed as

$$P = \frac{1}{2} U_m I_m \cos\varphi = UI \cos\varphi \tag{5.20}$$

where U and I are the root mean square (RMS) values of voltage and current, φ is the phase angle between the voltage and current, also called power factor angle, and $\cos\varphi$ is the power factor.

However, voltage waves on any actual transmission lines contain harmonics even within a well-designed power system. Substituting (5.16) and (5.17) into (5.19), total corona loss P can be computed. By averaging the product $u(t)\cdot i(t)$ over period T and employing the orthogonality relationships of the sine and cosine functions, total corona loss P can be expressed as

$$\begin{aligned} P = \sum_{i=1}^{i=n} P_i = U_1 I_1 \cos\varphi_1 + U_2 I_2 \cos\varphi_2 + U_3 I_3 \cos\varphi_3 + \\ \cdots + U_i I_i \cos\varphi_{i\,+\cdots+} U_n I_n \cos\varphi_n = U_c I_c \cos\varphi_c \end{aligned} \tag{5.21}$$

where U_i and I_i are the RMS values of i^{th} harmonic components of voltage and current respectively, φ_i is the phase angle between U_i and I_i, $\cos\varphi_i$ is the power factor of the i^{th} harmonic component, U_c and I_c are the complex RMS values of voltage and current, φ_c is the overall phase angle, and $\cos\varphi_c$ is the overall power factor.

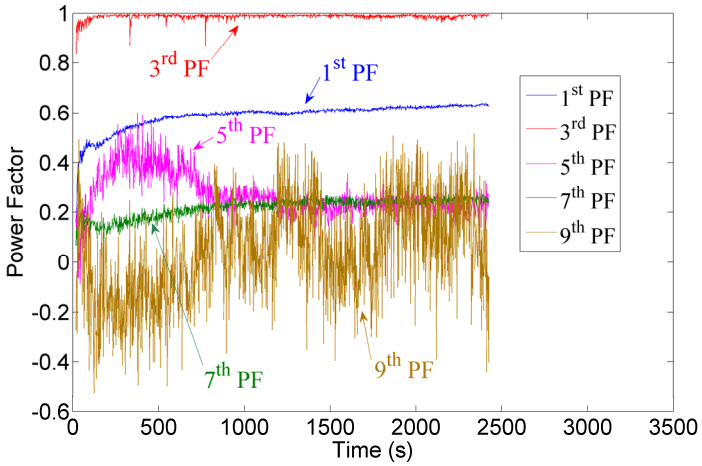

Figure 5-19: Power factors during the glaze ice accretion process with an applied voltage of 137.7 kV

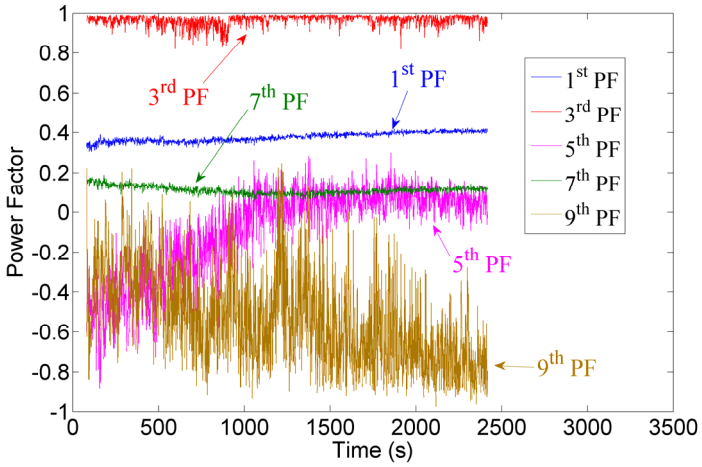

Figure 5-20: Power factors during the rime accretion process with applied voltage of 137.7 kV.

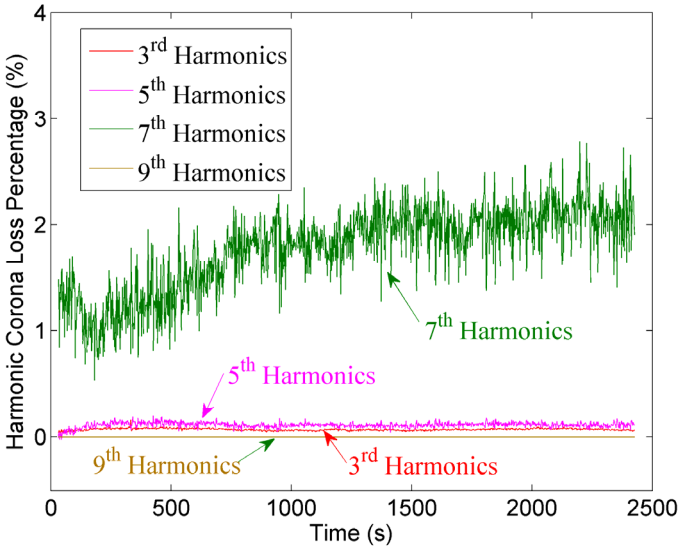

Figure 5-21: Harmonic corona loss in percentage of total corona loss of the glaze ice accretion with an applied voltage of 137.7 kV.

Figures 5-19 and 5-20 show the calculated power factors of glaze and rime ice accretion tests with an applied voltage of 137.7 kV. In Figure 5-21, harmonic corona losses in percentage of total corona loss for glaze ice are plotted. From these results, it can be noted that:

1) The power factor of the 9th harmonic component in Figure 5-19 as well as the 5th and 9th harmonic components in Figure 5-20 are negative at times. This is in agreement with Foley's study who concluded that the 3rd harmonic power factor can be negative [114]. In fact, generally the energy is

transferred from the power source to the load, but it can sometimes be transferred in an opposite direction, namely from the load to the power. In such a case, the power factor can be considered as negative as indicated in McEachern's correction to IEEE Standard 1459-2010 [115]. When the voltage applied to the conductor is a pure sine wave, some energy may be transformed from the fundamental to a harmonic state by the nonlinear mechanism induced by corona discharge. However, without the presence of harmonics in the applied voltage, the contribution of the harmonics to corona loss is zero according to (5.21) and this transformed energy is dissipated in the conductor. When the applied voltage contains harmonics, the harmonic energy can flow in both directions depending on whether the source of the harmonics is in the power source or in the nonlinear mechanism associate with the corona discharge. If it is from the nonlinear mechanism, the harmonic energy can be transferred back to the power source, leading to a negative power factor of the harmonic component. In the harmonic energy which is sent back along the line toward the line excitation source, some of it is dissipated in the line and some in the real component of impedance in the line excitation source.

2) The fundamental component contributes to most of the corona loss. In Figure 5-21, at least 97% of the total corona loss is contributed by the fundamental component. The contribution of other harmonic components to corona loss can be neglected, except for the significant harmonic component which is already contained in the applied voltage. Although the 7^{th} harmonic current is 53.5% of the fundamental component in magnitude, its contribution to corona loss is less than 3%. This is due to fact that the 7^{th} harmonic voltage component is only 10.1% of the fundamental and the power factor of this harmonic component is relative low, which is about 0.25 after 40 minutes of icing as shown in Figure 5.19.

3) The 3^{rd} harmonic component has a power factor close to 1 when the applied voltage is beyond its corona onset voltage. In this case, it can be expected that the contribution of the 3^{rd} harmonics to corona loss could be significant if the 3^{rd} harmonic component is appreciable in the applied voltage.

5.8 The dynamic characteristics of the 3rd power factor

As the magnitude of the corona current depends not only on the applied voltage but also on the configuration of the line and its length, it is not possible to conclude whether the conductor is operating below or above the corona onset voltage just by considering the magnitude of the corona current or the corona loss alone. The traditional way to obtain the corona onset voltage is to vary the applied voltage and then record the signals of corona current, photon number, or light emission intensity [42]. Then, the transition point can be obtained by the tangent method or by Peek's law.

However, based on the present experimental results, it was possible to see if the applied voltage is below or above the corona onset voltage by analyzing the power factor of the 3rd harmonics, without varying applied voltage. Based on the overall results in the present study, it can be concluded that if the average power factor of the 3rd harmonics is far less than 0.50, then the conductor is operating below its corona onset voltage. If the average power factor of the 3rd harmonics is higher than 0.50, then, it can be expected that the conductor is operating above its corona onset voltage. Otherwise, if the average power factor of the 3rd harmonics is close to 0.50, the applied voltage is considered to be close to the corona onset voltage in the tested weather conditions.

Figures 5-22 and 5-23 show the 3rd power factor over time and the fundamental, 3rd, and 7th power factors when the applied voltage was varied under glaze and rime ice conditions.

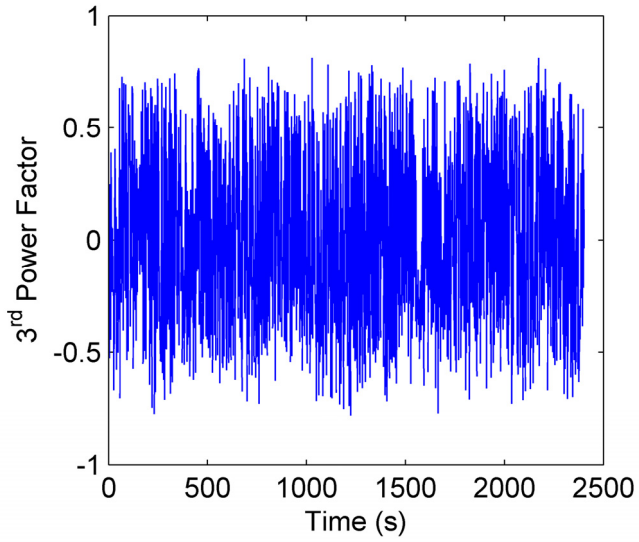

(a)

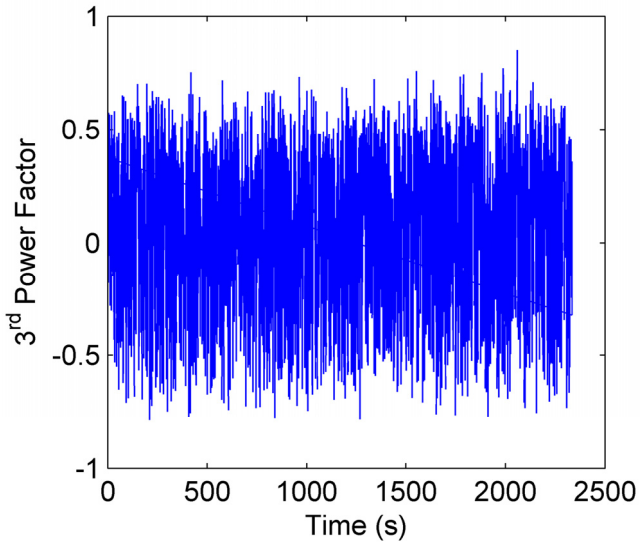

(b) Rime with V = 55.1 kV

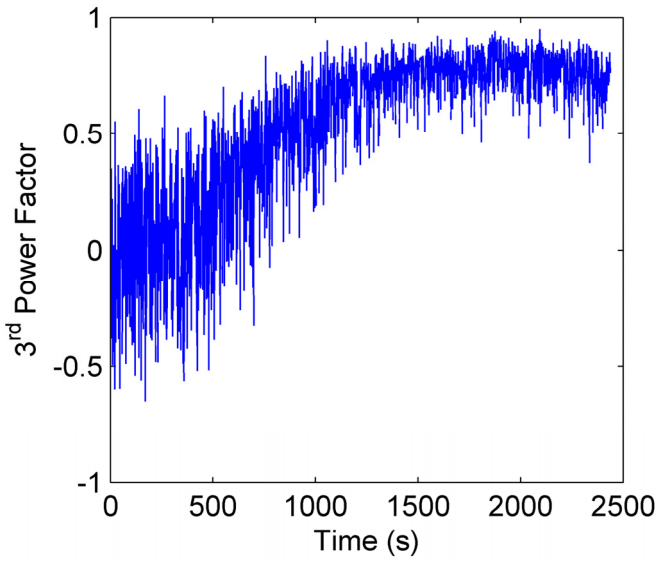

(c) Rime with V = 82.6 kV

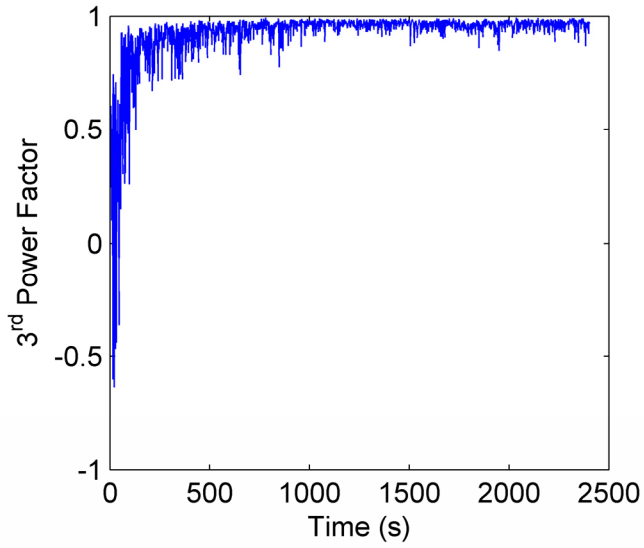

(d) Rime with V = 110.1 kV

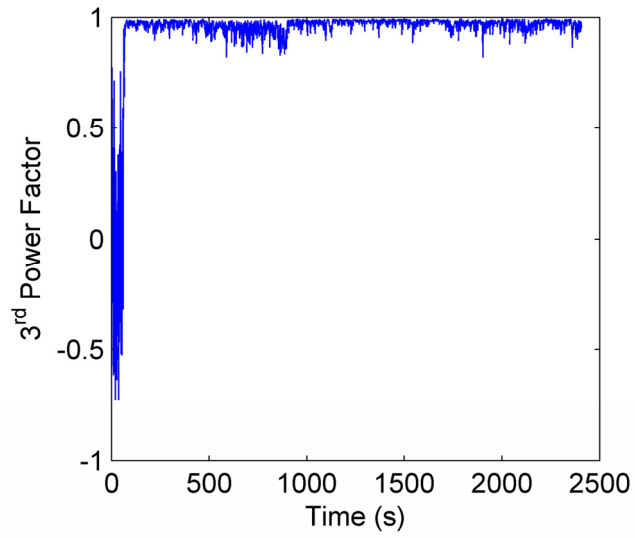

(e) Rime with V = 137.7 kV

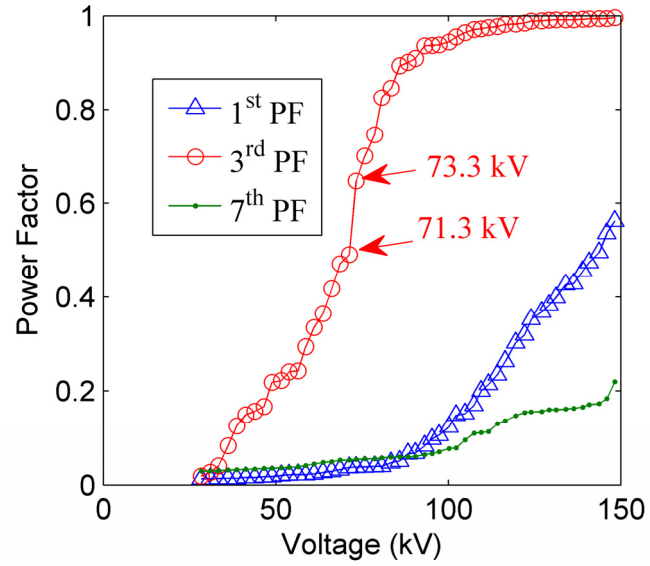

(f) Rime with V = 137.7 kV

Figure 5-22: The power factor vs. time and voltage under rime.

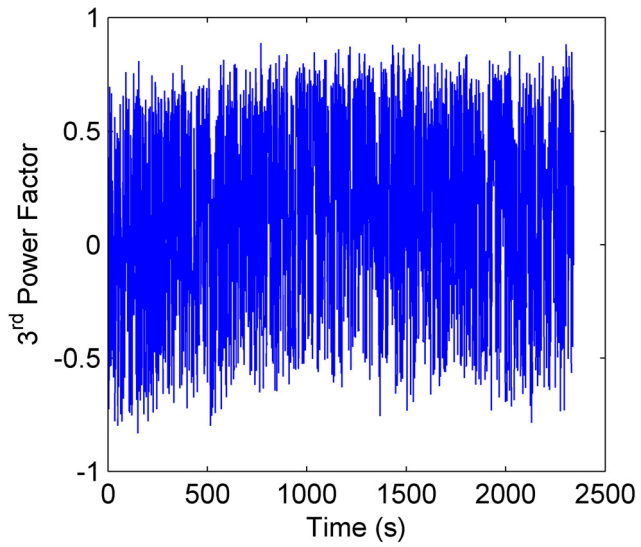

(a) Glaze with V = 27.5 kV

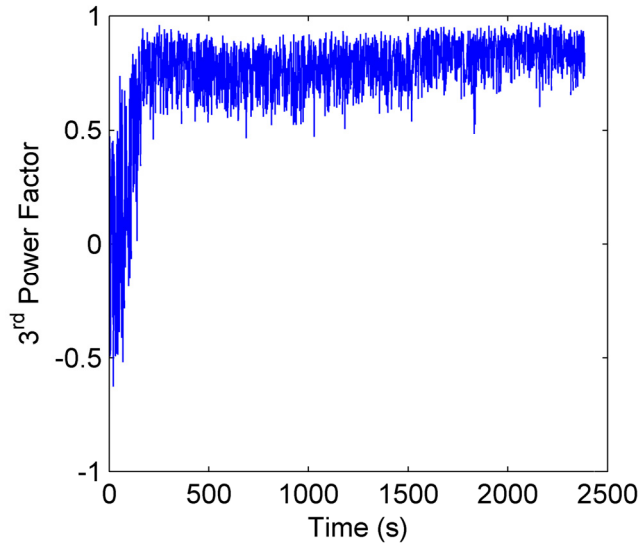

(b) Glaze with V = 55.1 kV

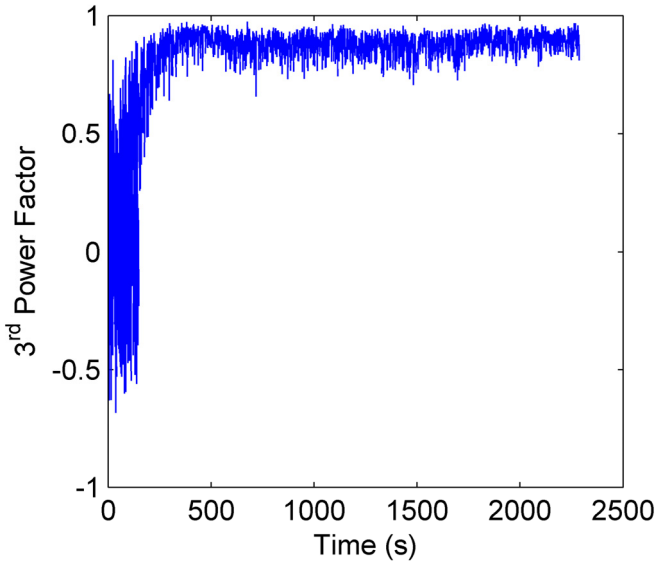

(c) Glaze with V = 82.6 kV

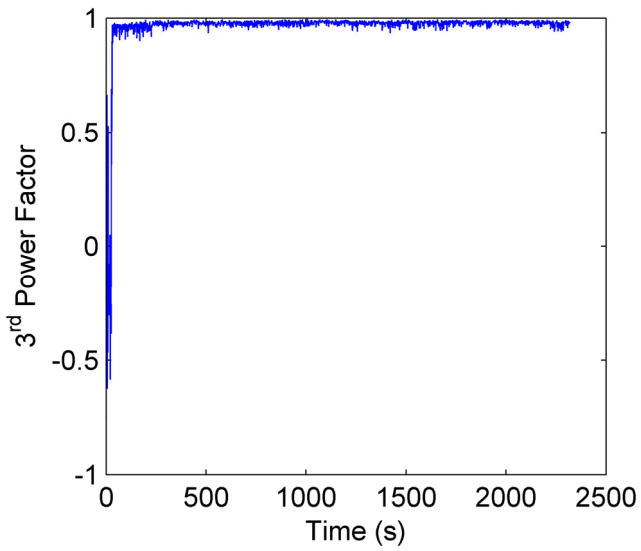

(d) Glaze with V = 110.1 kV

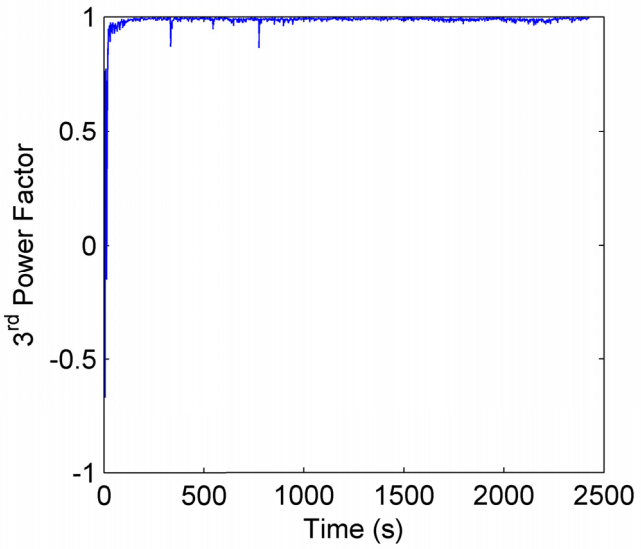

(e) Glaze with V = 137.7 kV

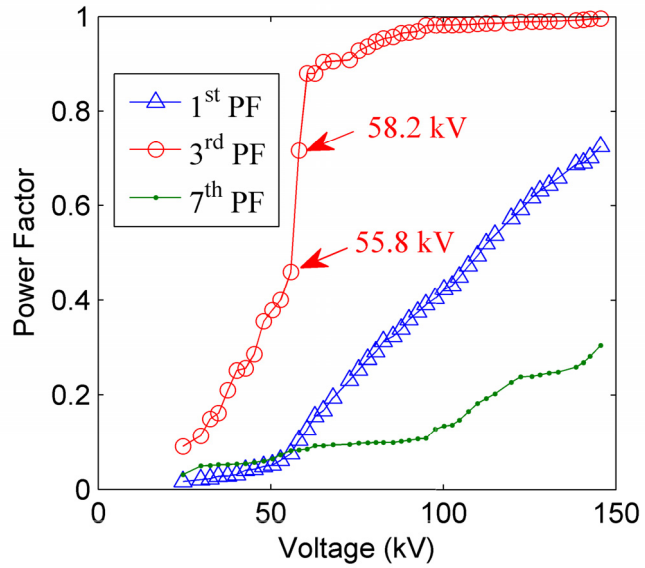

(f) Glaze with V = 82.6 kV

Figure 5-23: The power factor vs. time and voltage under glaze condition.

Taking glaze ice condition as an example, when applied voltage was 27.5 kV, which is below its corona onset voltage, as indicated in Table 5-7, the 3rd power factor varied between -0.83 and 0.89 and had an average value of 0.13. When the applied voltage was increased to 55.1 kV, the 3rd power factor was between -0.74 and 0.80 and had an average of 0.04 in the first 4 minutes of accretion. After

40 minutes of ice accretion, the average 3rd power factor increased to 0.72. This means that the conductor was operating beyond its corona onset voltage, which is 52.7 kV, as shown in Table 5-7. When the applied voltage was 82.6 kV, the 3rd power factor reached an average value of 0.50 after about 2 minutes and had an average value of 0.91 after 40 minutes of accretion. In the cases where the applied voltages were 110.kV and 137.7 kV, corona occurred shortly after the water spraying system was turned on. After 40 minutes of accretion, the average 3rd power factors were 0.98 and 0.99, respectively. It can also be concluded from the foregoing description that the average 3rd power factor significantly increases with the increase of corona discharge.

Figures 5-22f and 5-23f show the average power factor versus voltage after 40 minutes of energized rime and glaze ice accretion. It can be seen from these figures that the average fundamental and the 7th power factors increase slowly with increasing voltage. However, the average 3rd power factors increase abruptly when the applied voltages are close to their corona onset voltages. Using the linear interpolation method, the applied voltages generating an average 3rd power factor of 0.50 for the specific rime and glaze ice conditions are and 71.5 kV and 56.2 kV, respectively. They are almost the same as the values calculated by Peek's law, as shown in Tables 5-6 and 5-7, with relative differences of 3.4% and 2.4%, respectively.

5.9 Conclusion

In this chapter, the influence of electric field strength on corona characteristics are investigated. From the results obtained, the following conclusions can be drawn:

(1) Both rime and glaze ice can cause severe corona loss. The maximum corona losses happened when the temperature was relatively mild, which resulted in glaze ice accretion. With electric field higher than 5 kV_{rms}/cm during ice accretion, corona losses for glaze ice can be 2.44 to 23.1 times more than those for rime.

(2) When rime and glaze ice are accreted in the presence of an electric field, the corona losses increase first and then become stable with time. Wind velocity has an influence on corona loss. With an increase of wind velocity, the collision efficiency of water droplets increases, leading to a rapid increase in corona loss during the initial accretion stage.

(3) Conductivity of freezing water has little effect on corona loss for rime accretion. However, it has a moderate influence on corona loss for glaze ice accretion. This influence decays as the applied electric field increases.

(4) The electric field has a great influence on corona loss against voltage curve for both rime and glaze ice accretion. It will not only shift the corona onset voltage, but also change the shape of the curve. For rime accretion, the corona onset voltage initially decreases with an increase of electric field, and then increases when the electric field is higher than 20 kV_{rms}/cm. For glaze ice accretion, the corona onset voltage increases with an increase of electric field in the whole test field strength range.

(5) The surface irregularity factor of the conductor can be greatly reduced by the presence of rime and glaze. The most adverse condition happens under glaze ice condition where the surface irregularity factor can be lowered to 0.30.

(6) Leakage conductance of a conductor-cage configuration are at their highest under glaze icing condition and at their lowest under rime icing condition for the same conductor surface electric field.

(7) When the applied voltage is below the corona onset voltage, the 3^{rd} harmonic current component is unnoticeable if the 3^{rd} harmonic voltage component is insignificant in the applied voltage. However, when the applied voltage is beyond its corona onset voltage, the 3^{rd} harmonic current component is significant even if the 3^{rd} harmonic voltage component is minor in the applied voltage.

(8) The fundamental applied voltage component contributes to most of the corona loss. The contribution of other harmonic components to corona loss can be neglected, except for the cases where a significant harmonic component is already contained in the applied voltage.

(9) The power factors of the harmonic components can be considered as negative at times as it was the case in the present study for the 3^{rd}, 5^{th}, and 9^{th} harmonics during ice accretion. These results are in support of McEachern's correction to IEEE Standard 1459-2010.

(10) Capacitance of the conductor-cage configuration increases during ice accretion on the conductor. After 40 minutes of rime accretion, the capacitance increases with the applied electric field during icing. With the presence of icicles, however, capacitance under glaze ice accretion is complex.

CHAPTER 6

ICE ACCRETION SIMULATION AND ITS EXPERIMENTAL VALIDATION

CHAPTER 6

ICE ACCRETION SIMULATION AND ITS EXPERIMENTAL VALIDATION

The environmental parameters influence the ice type and the accretion mass. Two types of deposit, namely rime and glaze ice, lead to significant loads on structures [1]. The heat balance is very sensitive in case of glaze ice, because it occurs at the transition of freezing and melting and is therefore considered as wet ice growth. To simplify the simulation, only rime accretion on DC negative energized conductor is simulated in the present study. Under rime condition, ice develops in dry growing and the heat transfer within the system can be neglected as the latent heat of the droplets released during freezing is dissipated without changing the state of the ice and the surface conditions. Hence, no liquid layer arises. As icing condition is the same over the measurement section, the rime accreted is uniform along the conductor. Thus, the simulation can be carried out in 2D.

6.1 Ice accretion model

6.1.1 Model structure

This section provides an overview of the ice accretion model. To investigate the influence of electric field on ice accreted on transmission line, a concentric configuration model is used to generate the required electric field strength. The cross section of this configuration is shown in Figure 6-1. The energized conductor is put in the center and the collector is grounded. The wind blows the freezing water droplets toward the conductor from right. The angle between wind and horizon is 45°. The advantage of this configuration is that the close distance between the tested conductor and grounded collector can replicate the surface electric field of a practical transmission line at a much lower applied voltage. Thus, it is possible to validate the model by comparing the simulation results with laboratory tests. When the conductor is energized, the magnitude of the electric field at the surface of conductor E_{surface} (kV/cm) can be calculated by the following formula:

$$E_{surface} = \frac{U_{app}}{D/2\ln(2R/D)} \tag{6.1}$$

where U_{app} is the applied voltage in kV, R is the radius of the collector in cm, and D is the diameter of the conductor in cm. In this model, R and D are 50 cm and 3.2 cm respectively.

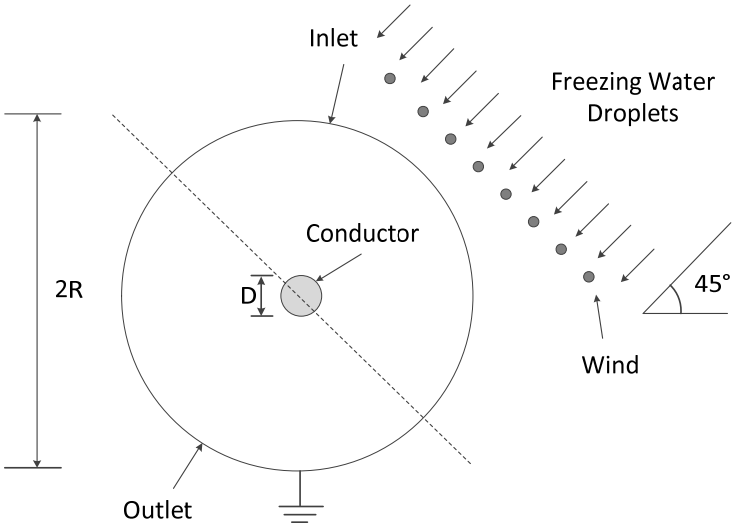

Figure 6-1: Model structure

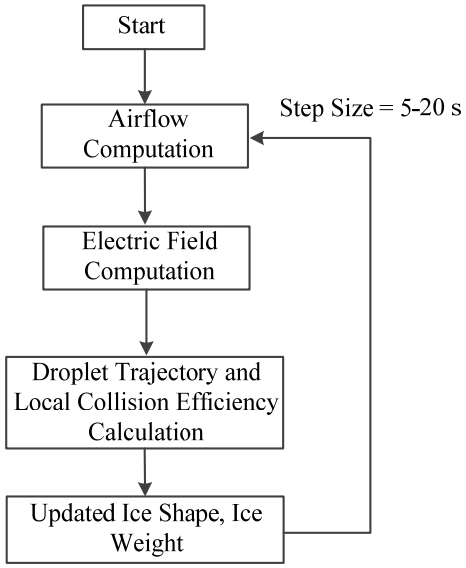

Figure 6-2: Flow diagram of simulation

Figure 6-2 shows the flow diagram of the rime accretion model described in this study. It displays all elements of a single simulation step. Each step assumes steady conditions over a time interval of 5 to 20 seconds. The size of the time steps depends on the accumulated mass on the conductor. A

large flux of icing particles requires smaller time steps than a low flux to adequately describe the ice growth. As consequence of assuming steady conditions during each calculation, the model can not account for transient particle flux.

As can be seen in Figure 6-2, the airflow is computed in each iteration. It is time consuming to calculate the airflow in the whole region between the conductor and collector as shown in Figure 6-1. It is verified that when a small water droplet is at a distance higher than 10xD away from the windward direction, the influence of the electric field is negligible. Thus, the air flow calculation can be limited to a rectangle channel containing the conductor as shown in Figure 6-3. The height and width of the rectangle are respectively 8xD and 15xD, where *D* is the diameter of the conductor. As the trajectory of water droplet in the leeward is not of our interest, only distance of 5x*D* is calculated in this direction.

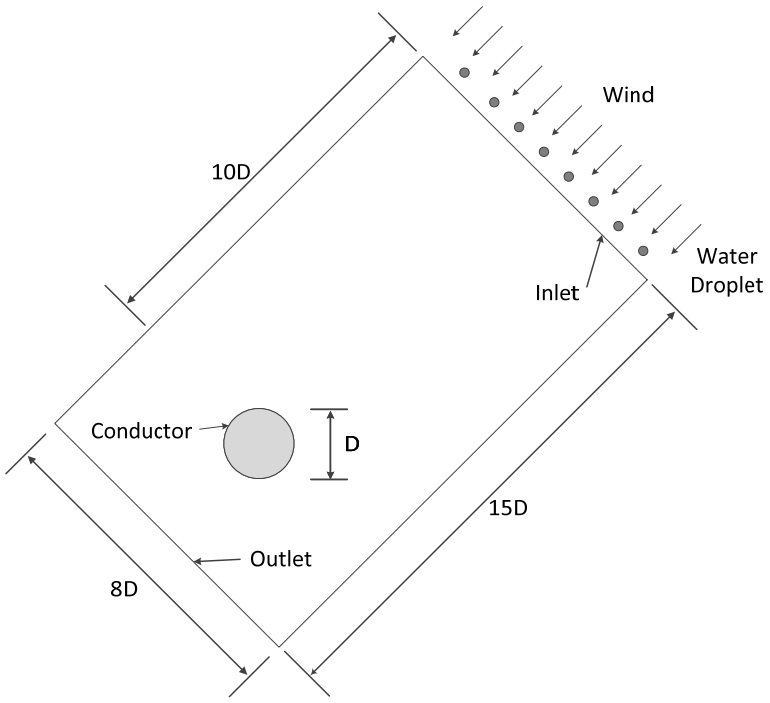

Figure 6-3: Reduced computational zone

6.1.2 Airflow computation

The airflow is described by a set of state equations, namely the continuity, the momentum and the energy equation [116-117]. The term Navier-Stokes equation originally meant only the momentum equation, but in recent literature it is also used for the whole set of state equations. These equations can allow for viscous and thermal effects and therefore they can describe turbulent and compressible flows. For many applications, it is possible to simplify the problem by considering an incompressible flow.

The pattern of flow can be laminar, transitional, and turbulent, depending on the Reynolds number. For the flow past a circular cylinder, there exists a critical Reynolds number $\mathrm{Re}_{\mathrm{crit}} \approx 3 \times 10^5$ [118]. Below this Reynolds number, the motion of the flow is laminar. Above, it undergoes transition to turbulence. When it comes to flow past transmission lines, the Reynolds number has an order of magnitude of 10^4. Therefore, it can be assumed that the airflow is incompressible and laminar in the calculation zone [119]. The Navier-Stokes equations for incompressible airflow assume a constant density, which is a reasonable approach for airflow around the conductor. Assuming an incompressible airflow allows us to decouple the continuity and the momentum equation from the conservation of energy. It also includes assuming the viscosity to be constant. Hence, the continuity equation of an incompressible flow becomes:

$$\nabla \cdot \boldsymbol{u} = 0 \tag{6.2}$$

$$\rho \frac{\partial \boldsymbol{u}}{\partial t} + \rho(\boldsymbol{u} \cdot \nabla)\boldsymbol{u} = -\nabla p + \nabla \cdot \mu(\nabla \boldsymbol{u} + (\nabla \boldsymbol{u})^T) + \boldsymbol{f} \tag{6.3}$$

where u is the air velocity vector in m/s, ρ is the air density in kg/m^3, p is the pressure in N/m^2, μ is the viscosity of air in kg/(m·s), f is the body force acting on the air. As the airflow is assumed stable in each step, equation (6.3) can be reduced to

$$\rho(\boldsymbol{u} \cdot \nabla)\boldsymbol{u} = -\nabla p + \nabla \cdot \mu(\nabla \boldsymbol{u} + (\nabla \boldsymbol{u})^T) + \boldsymbol{f} \tag{6.4}$$

To calculate the airflow, the boundary conditions should be set. The inlet velocity equals to the initial wind velocity, zero pressure is applied to the outlet air boundary, and no-slip conditions are applied to the two long edges of the channel and conductor surface.

6.1.3 Droplet trajectory calculation

With the airflow and the electric field distribution known, it is possible to calculate the cloud droplet trajectory. When the discrete water droplets are present at a fairly low volume fraction, usually less than 10-12 %, the droplet-droplet interactions and the effects of the droplet volume fraction on the air are negligible. In practice, the cloud droplet is small and the order of magnitude of the water content in clouds is very low. Clouds that have high densities, like cumulonimbus clouds, have typical liquid water content (LWC) around 1.0-3.0 g/m^3 according to the study by Leng [120]. Black and Hallett [121] have showed through observations that the LWC for storms are about 3.1-18.0 g/m^3, less than 0.0002% in volume fraction. Thus, it can be reliably assumed that the airflow is not perturbed by the presence of cloud droplets in the present study [122]. The trajectory followed by a cloud droplet, subsequent to its generation and release, depends not only upon its initial velocity, but also upon the external forces exerted on it. The cylinder is assumed to be infinitely long so that the end effects can safely be ignored. Droplet-droplet interaction is not considered here and this study only focused on the motion of an individual cloud droplet. In the presence of electric field, the cloud droplet moving in the airflow is subjected to electric force, drag force, buoyancy force, Brownian force, and gravity. In the present study, cloud droplets of micrometer order in size colliding with the cylinder are considered. Droplets of this size range are relative massive (ρ_d = 1 g/m^3) and therefore the effect of Brownian on collision was disregarded.

1) Dielectrophoretic Force

As discussed in section 4.2, although water droplet is polarized by the external electric field, it can still be treated as a sphere in the range of electric field in the present study. The dielectrophoretic force $\boldsymbol{F}_{DEP}$ exerted on the polarized cloud droplet then can be calculated, using Equation (4.5) as

$$\boldsymbol{F}_{DEP} = \boldsymbol{p} \cdot \nabla \boldsymbol{E} = 4\pi\varepsilon_0\varepsilon_1 a^3 \boldsymbol{E} \cdot \nabla \boldsymbol{E} \tag{6.5}$$

2) Drag Force

In fluid dynamics, drag refers to forces acting opposite to the relative motion of any object moving with respect to a surrounding fluid. This can exist between two fluid layers or a fluid and a solid surface. Drag force depends on the properties of the fluid and on the size, shape, and relative speed of the object to the fluid. With 10×D distance of the cylinder, it is reasonable to assume that the cloud droplet is riding with the speed of the air stream at a horizontal velocity at v_0, i.e., that there is no slip between the cloud droplet and the air. However, as long as the airflow streamlines begin to diverge, they will no longer have the same velocity. Hence, a drag effect comes into play which depends on the vector difference between the cloud droplet and the air velocity. When a cloud droplet of radius a is moving relative to the air, the drag force on the cloud droplet is calculated as [25]

$$\boldsymbol{F}_d = \frac{1}{2}\rho_a C_D A \left|\boldsymbol{V}_d - \boldsymbol{V}_a\right| (\boldsymbol{V}_d - \boldsymbol{V}_a) / C_{sc} \tag{6.6}$$

where $\boldsymbol{F}_d$ is the drag force in N, ρ_a is the density of the air in kg/m^3, $\boldsymbol{V}_d$ and $\boldsymbol{V}_a$ are the velocity vectors of the cloud droplet and airflow respectively in m/s, $A = \pi a^2$ is the cross-sectional area in m^2, C_D is the dimensionless drag coefficient, and C_{sc} is the Stokes-Cunningham slip correction factor which is expressed as [123]

$$C_{sc} = 1 + \frac{2\lambda}{d}(1.257 + 0.4e^{-(1.1d/2\lambda)}) \tag{6.7}$$

where d is the particle diameter in m and λ is the mean free path in m for a typical molecule in the fluid.

For atmospheric pressure, the mean free path λ is determined by [124]

$$\lambda = \frac{\mu}{p}\sqrt{\frac{\pi k_B T}{2m}} \tag{6.8}$$

where k_B is the Boltzmann constant in J/K, T is the temperature in K, and m is the molecular mass in kg. At an ambient temperature of -15 °C, the corresponding λ of air is 55 nm. Substituting d and λ into (6.7), it can be concluded that $C_{sc} \approx 1$ for the particle size range considered in the present study.

The drag coefficient C_D depends on the shape of the object, the circulation within the droplet, and the Reynolds number. For our range of droplet radius, the circulation effects on the drag coefficient were ignored. For the cloud droplet moving in the air, the Reynolds number Re_d of the cloud droplet is expressed as [125]

$$Re_d = 2a\frac{|\boldsymbol{V}_d - \boldsymbol{V}_a|}{\upsilon} \tag{6.9}$$

where a is the cloud droplet radius in m and v is the kinematic viscosity of air in m^2/s. The relationship between C_D and Re_d is based on the experiments carried out by Langmuir and Blodgett [126] and McComber and Touzot [81], as follows

$$\frac{C_D Re_d}{24} = 1 + 0.189 \times Re_d^{0.632} \quad \text{for } 21 < Re_d <= 200 \tag{6.10}$$

$$\frac{C_D Re_d}{24} = 1 + 0.115 \times Re_d^{0.802} \quad \text{for } 2 < Re_d <= 21 \tag{6.11}$$

$$\frac{C_D Re_d}{24} = 1 + 0.102 \times Re_d^{0.955} \quad \text{for } 0.2 < Re_d <= 2 \tag{6.12}$$

$$\frac{C_D Re_d}{24} = 1 + 0.197 \times Re_d^{0.63} + 2.6e^{-4} \times Re_d^{1.38} \quad \text{for the remaining } Re_d \text{ number} \tag{6.13}$$

3) Buoyancy Force

The behavior of an object submerged in a fluid is governed by Archimedes' principle. Buoyancy arises from the fact that fluid pressure increases with depth and from the fact that the increased pressure is exerted in all directions so that there is an unbalanced upward force on the bottom of a submerged object. The definition of this force is

$$\boldsymbol{F}_b = -\rho_a V \boldsymbol{g} \tag{6.14}$$

where V is the volume of the cloud droplet in m^3, $\boldsymbol{g}$ is the gravitational field vector in m/s^2.

4) Gravity

Gravity or gravitation is a natural phenomenon by which all things attract one another including stars, planets, galaxies and even light and sub-atomic particles. For the earth, the classical formula is as follows:

$$\boldsymbol{F}_d = \rho_d V \boldsymbol{g} \tag{6.15}$$

where ρ_d is the density of the water in kg/m^3.

When taking the above electric force, drag force, buoyancy force and gravity into account, the motion of the water droplet can be determined by the motion equation. The complete vector equation describing the accelerated motion of water droplets (having a fixed mass) in dry air can be expressed as:

$$\frac{d\boldsymbol{V}_d}{dt} = \frac{\rho_d - \rho_a}{\rho_d}\boldsymbol{g} - \frac{3C_D\rho_a}{8a\rho_d}\left|\boldsymbol{V}_d - \boldsymbol{V}_a\right|(\boldsymbol{V}_d - \boldsymbol{V}_a) + \frac{3\varepsilon_0\varepsilon_1}{\rho_d}\boldsymbol{E}\cdot\nabla(\boldsymbol{E}) \tag{6.16}$$

$$\frac{dx}{dt} = \boldsymbol{V}_{dx} \tag{6.17}$$

$$\frac{dy}{dt} = \boldsymbol{V}_{dy} \tag{6.18}$$

where (x, y) is a position vector of the cloud droplet. Combined with given initial conditions, the solutions of (6.16) to (6.18) can determine the cloud droplet trajectory. As the density of air is negligible compared with that of water, (6.16) can be simplified to

$$\frac{d\boldsymbol{V}_d}{dt} = \boldsymbol{g} - \frac{3C_D\rho_a}{8a\rho_d}\left|\boldsymbol{V}_d - \boldsymbol{V}_a\right|(\boldsymbol{V}_d - \boldsymbol{V}_a) + \frac{3\varepsilon_0\varepsilon_1}{\rho_d}\boldsymbol{E}\cdot\nabla(\boldsymbol{E}) \tag{6.19}$$

6.1.4 Collision efficiency calculation

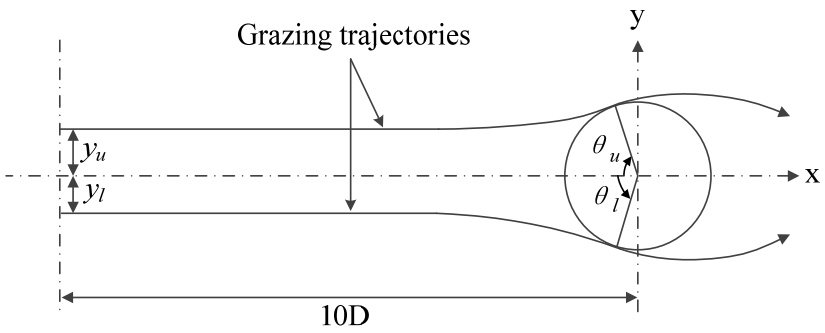

Figure 6-4: Grazing trajectories of water droplets

The grazing trajectories with initial ordinates of y_u and $-y_l$ determine the maximum extent of impingement of water droplets are shown in Figure 6-4. All the water droplets have initial ordinates within y_u and $-y_l$ strike the cylinder while all water droplets have initial ordinates beyond this range will miss the cylinder.

The droplet is assumed to have impinged upon the conductor if any part of it contacts the ice surface. Thus, close to the conductor, the finite size of the droplet is taken into account. This is particularly important for those trajectories just within the envelope of colliding trajectories, where the

angle of incidence from the normal to the conductor surface is close to 90°. Ice loads is formed due to particles in the air colliding with the cylinder. Thus, it is very important to calculate the overall collision efficiency of the particles. The overall collision efficiency η is defined to be the ratio of the number of water cloud droplets impinging the cylinder to the number which would impinge it if the streamlines are not deflected by the cylinder.

$$\eta = \frac{y_u - y_l}{D} \tag{6.20}$$

where D is the diameter of the cylinder.

To get the ice shape, it is necessary to know the local collision efficiency β. When β is multiplied by the LWC and the free stream velocity V_∞, the mass flux of water captured on the specified local surface of the cylinder can be given. To determine the local collision efficiency, as shown in Figure 6-5, the following relationship is used:

$$\beta(L) = \frac{dY}{dL} \tag{6.21}$$

where Y is the ordinate at the starting point of a particular trajectory, L is the distance along the ice surface between the stagnation point and the impact point of the same trajectory. By calculating the trajectories for enough number of droplets, Y may be plotted as a function of L, and the derivative taken to obtain β. The local collision efficiency is used to obtain the distribution of the water on the cylinder surface.

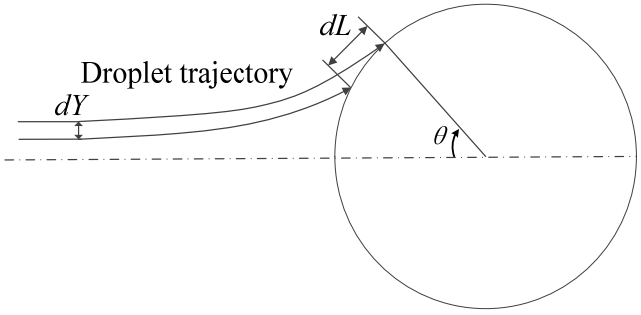

Figure 6-5: Definition of local collision efficiency

6.1.5 Ice growth process

1) Ice density

The ice accretion ratio allows for the density of the precipitation fluxes and the evolving density of ice deposits. The ice density is determined by empirical equations. There are many formulas used for calculating the ice density, most of them are based on the Macklin's parameter [127] which is defined in the following formulation:

$$R = \frac{V_0 d_m}{2t_s} \tag{6.22}$$

where d_m is the median volume diameter of the droplets, V_0 is the impact speed of the droplets at the stagnation point as obtained from droplet trajectory calculations and t_s is the local surface temperature on the ice surface. In the present study, the equations derived by Bain and Gayet are chosen [128]:

$$\rho_i = 110 \cdot R^{0.76} \qquad for \qquad 0 < R \le 10 \tag{6.23}$$

$$\rho_i = \frac{R}{R + 5.61} \cdot 10^3 \qquad for \qquad 10 < R \le 60 \tag{6.24}$$

$$\rho_i = 917 \qquad for \qquad 60 < R \tag{6.25}$$

2) Growth of ice layer

In the model, it is assumed that the ice growth on a particular small segment of the conductor surface is oriented perpendicular to the surface. The accretion thickness is then given by the equation:

$$h(L) = \frac{2R(L)t_A}{\rho_i} \Big/ \left(1 + \sqrt{1 + \frac{2R(L)t_A}{\rho_i r(L)}}\right) \tag{6.26}$$

where $R(L)= V_\infty \omega \beta(L)$ is the icing flux with V_∞ the free stream velocity, ω the liquid water content of the airstream, and $\beta(L)$ the local collision efficiency. t_A is the period of accretion, ρ_i the assumed ice density, and r the radius of curvature of the conductor surface. In the results presented here, we assume that time interval t_A is sufficiently small that the second term under the root in the denominator may be ignored. Then, Eq. (6.26) can be reduced to:

$$h(L) = \frac{R(L)t_A}{\rho_i} \tag{6.27}$$

By plotting the accretion thickness as a function of distance along the conductor surface from the stagnation point, it is possible to determine a new conductor surface layer after it has iced for the specified time interval. The entire procedure can now be repeated, using the new iced conductor surface to determine a new stream function, new droplet trajectories, and ultimately a second accretion layer. By continuing in this manner, it is possible to build up a substantial ice accretion on the conductor as shown in Figure 6-6.

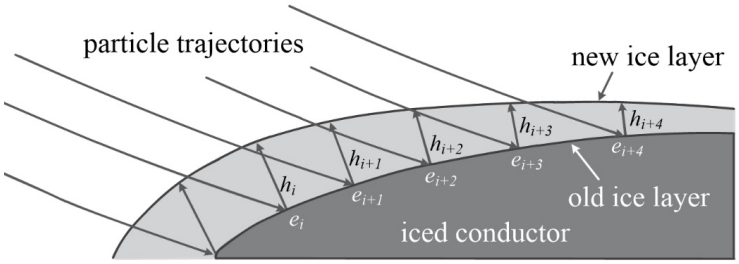

Figure 6-6: Growth of ice surface

6.2 Model simulation and validation

To simplify the computation, only the rime accreted under various DC negative electric field strengths were simulated. Rime ice is formed when the super-cooled water droplets collide with a substrate under conditions in which the droplets freeze upon impact. The environment temperature remains sufficiently below freezing so that no runback of liquid water occurs. The fluid flow and water droplet trajectory calculated in the present study are solved by coupling finite element software

COMSOL Multiphysics with MATLAB. In each iteration, the COMSOL was used to compute the air flow and electric field distribution. With the air flow and electric field known, the MATLAB was used to calculate the trajectory of water droplet and local collision efficiency. After that, the ice layer was updated and iteration was repeated until the simulation time was over. The model parameters chosen in the present study are consistent with experimental parameters and are listed in Table 6-1.

Table 6-1: Simulation Parameters of Rime Accretion

Ambient air temperature (℃)	-15
Water droplet size (μm)	38, 59
Wind velocity (m/s)	2, 4
Liquid water content (g/m^3)	2.1, 1.05

6.2.1 Comparison of accreted rime between experiments and simulations

It is well known that the quality of the numerical solution depends on an appropriate mesh with sufficient mesh density in calculation regions. The mesh of the domain is plotted in Figure 6-7. The meshes shown in Figures 6-7 was used for the two-dimensional computations.

To make a balance between accuracy and computational effort for the modeling. The mesh is set as follows. On the boundary of the cylinder or iced cylinder, the maximum element size is set at 0.008 m. The reduced computational zone is set extremely fine and extra fine for all the rest. The detailed statistics for the meshes are listed in Table 6-2.

Table 6-2: Statistics for the meshes employed

Number of vertex elements	12
Number of boundary elements	258
Number of elements	10052
Minimum element quality	0.7186

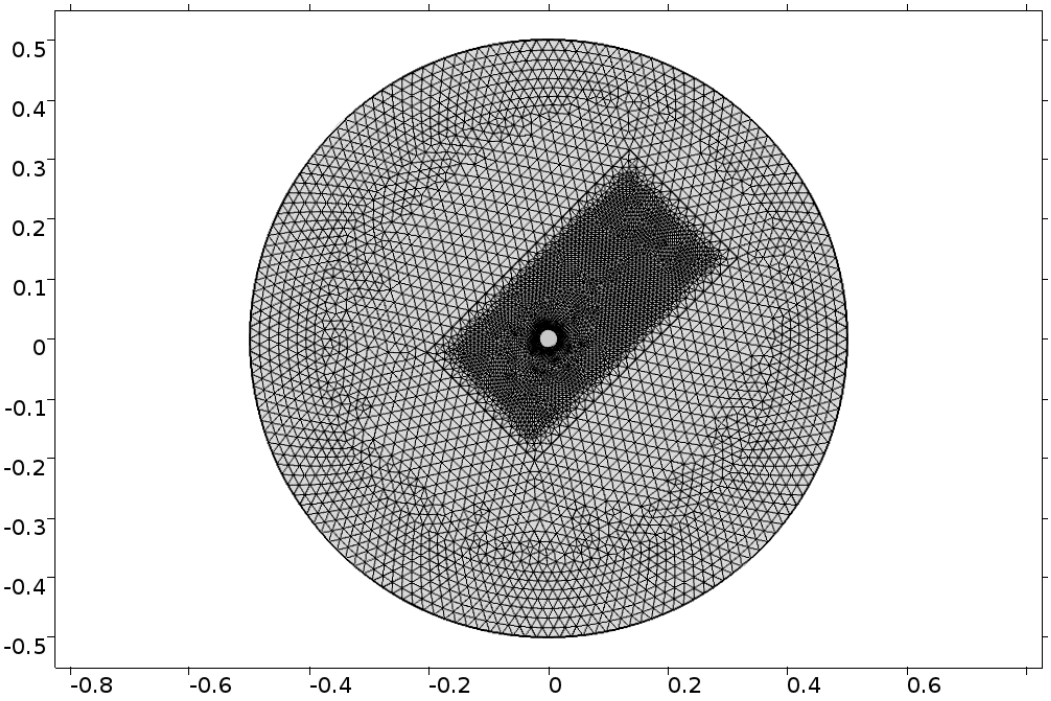

Figure 6-7: Mesh of the domain in the initial stage.

Figure 6-8 illustrate the airflow past the cylinder when the wind velocity is 2 m/s. For the cylinder, the airflow is symmetrical. When the air is passing the cylinder, the velocity is accelerated. In the mean while, there exists a velocity reduced zone in the windward of the cylinder. In the stagnation point, the wind velocity is 0 m/s. As the Reynolds number is 4824 when the wind velocity is 2 m/s which far below Re_{crit}, the laminar boundary layer remains stable.

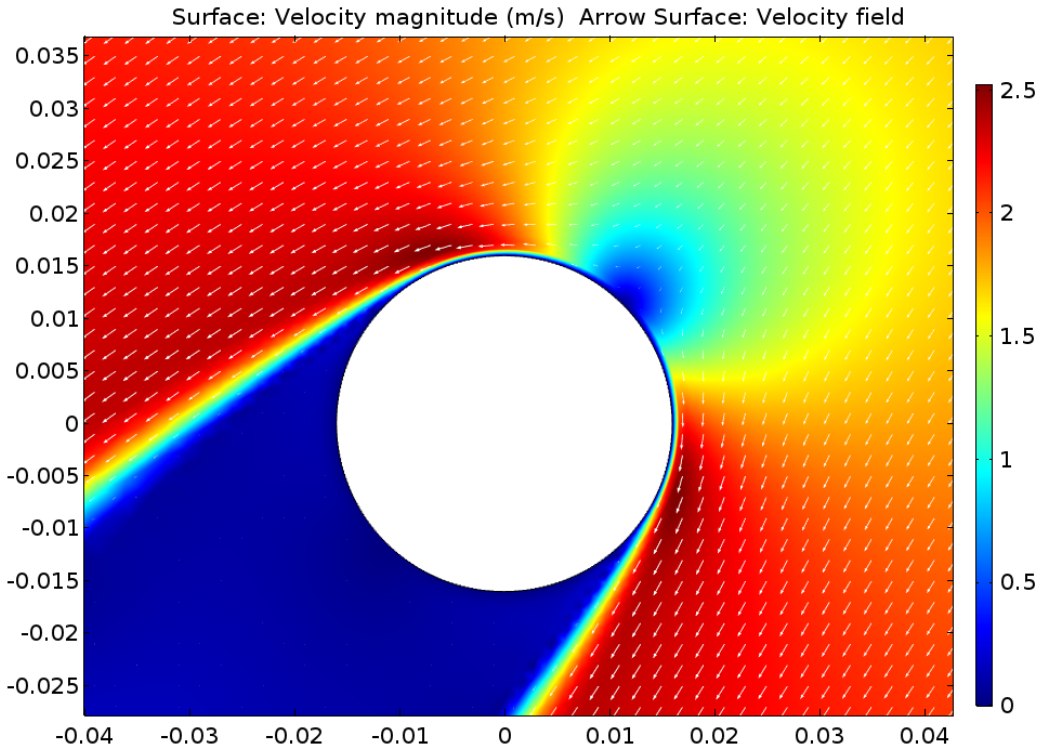

Figure 6-8: Airflow past the cylinder when the wind velocity is 2 m/s.

Figure 6-9 shows the water droplets captured and their impaction velocities when touching the cylinder. In the simulation, the wind velocity is 2 m/s, the voltage applied on the outer cylinder is -137 kV, and the diameter of the water droplets are 59 μm. To make the water droplets visible in Figure 6-9, the water droplets shown are six times of their real size. In Figure 6-9, the first color legend in the right side shows the electric field and the second color legend denotes the impaction velocity of water droplet. It can be seen that the conductor surface electric field is -25 kV/cm. The impaction velocity of the water droplet changes along the conductor surface. It reaches the highest value of 1.59 m/s near the grazing trajectory and gets the lowest velocity of 1.18 m/s at the stagnation point.

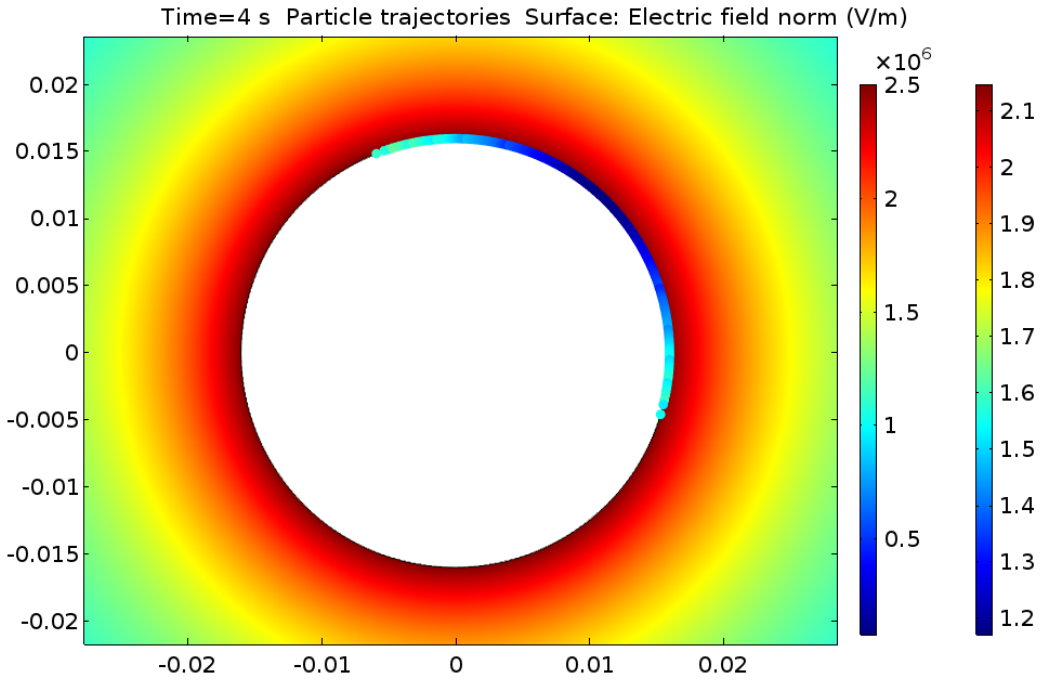

Figure 6-9: Water droplets captured and their impaction velocities (the water droplet is not to scale).

Table 6-3: The Calculated Overall Collision Efficiency of Particles at Different Conductor Surface Electric Field Strengths with a Wind Velocity of 2 m/s.

	Drag Only	**0 kV/cm**	**5 kV/cm**	**10 kV/cm**	**15 kV/cm**	**20 kV/cm**	**25 kV/cm**
d = 38 μm	0.161	0.182	0.183	0.185	0.189	0.192	0.198
d = 59 μm	0.398	0.433	0.434	0.436	0.439	0.443	0.449

With the location of each captured water droplet and its starting position known, the overall collision efficiency and local collision efficiency can be obtained. Table 6-3 lists the calculated overall collision efficiency η of two different particles at various conductor surface electric field strengths when the wind velocity is 2m/s. The "Drag Only" column only considers the drag force while the rest columns consider all the forces in equation (6.19), including the drag, gravity, and the dielectrophoretic force. A comparison of the "Drag Only" column and the column right after it can tell that, when the gravity is included, η increases 0.021 and 0.035 for droplet diameter of 38 μm and 59 μm, respectively. As the gravity was ignored in [79][82], it can be expected the overall collision efficiency was underestimated in their calculations. When the conductor is energized, η increases with an increasing of conductor surface electric field strength. It can also be concluded that the larger the droplet, the greater the η.

To get the local collision efficiency, the function $Y(L)$ should be obtained first as discussed in section 6.1.4. In the present study, the positive directions of Y and L are denoted in Figure 6-10 and θ is the contact angle. Then, $Y(L)$ of Figure 6-9 can be plotted in Figure 6-11. It can been see that the value of Y changes quickly near the centerline ($L = 0$) and its curve becomes flat at both ends.

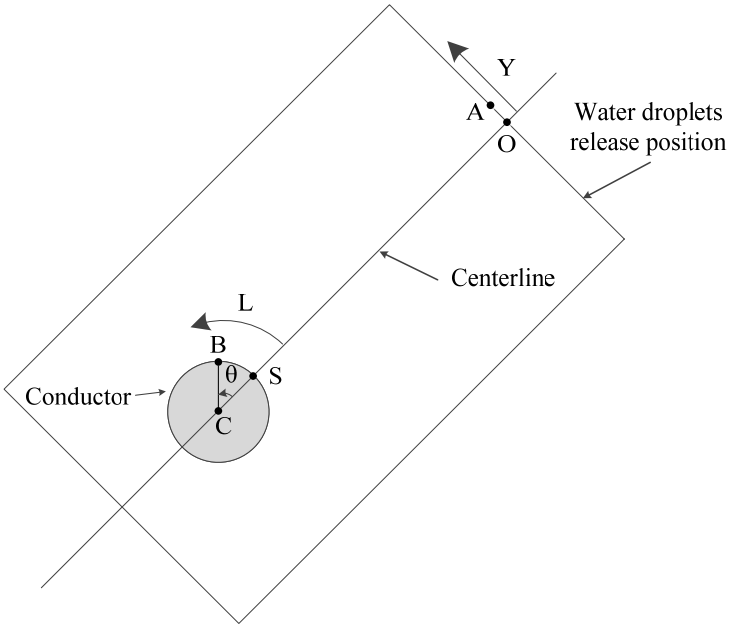

Figure 6-10: The definition of Y and L.

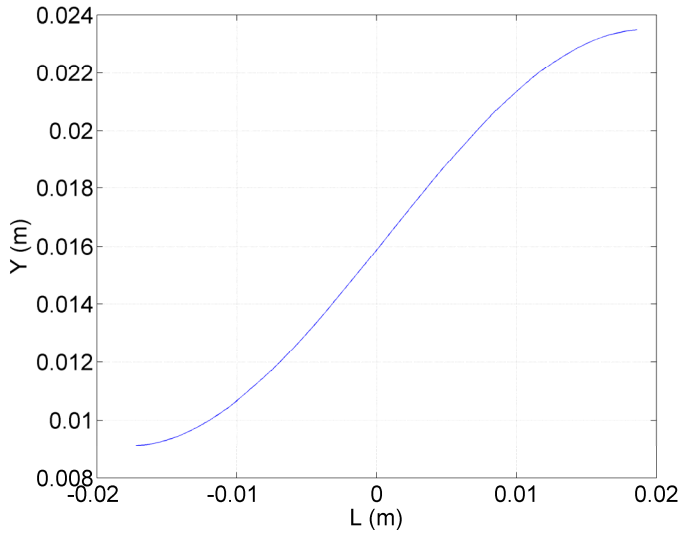

Figure 6-11: The relationship between Y and L.

Take the derivative of Y in Figure 6-11, the local collision efficiency β can be obtained as shown in Figure 6-12. If the gravity is not considered, the curve of β should be symmetric with the symmetry axis at L = 0 m. However, when the gravity is included in the motion equation, it can be seen that the curve is shifted a little bit to the right side in Figure 6-12. This means that the conductor on the upper-left side of the centerline captures more water droplets than on the below-right side of the centerline. Dividing L by the conductor radius r_c can get the contact angle. The maximum contact angles calculated based on Figure 6-12 are 66.6º and 61.6º respectively on the upper-left side and lower-right side of the centerline.

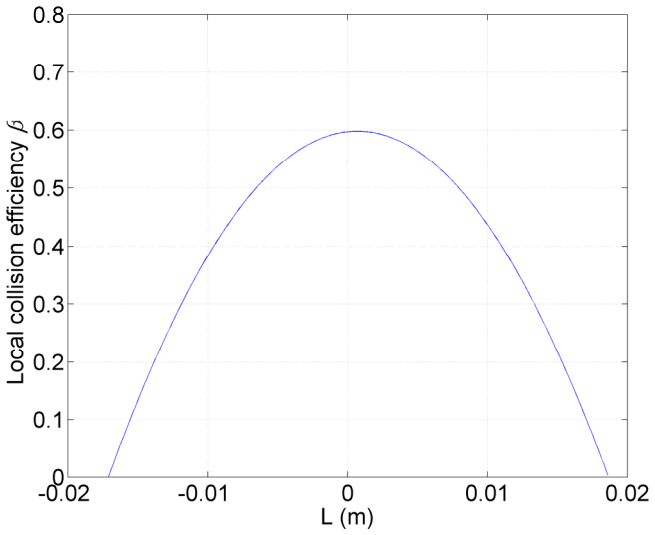

Figure 6-12: The local collision efficiency curves along the conductor surface when the wind velocity is 2 m/s, droplet diameter is 59 μm, and conductor surface electric field is -25 kV/cm.

When the local collision efficiency is known, then the ice accreted in each segment can be calculated by (6.26). Figure 6-13 shows the rime simulated after 40 minutes of accretion when the DC electric field was -5 kV/cm and wind velocity is 2 m/s.

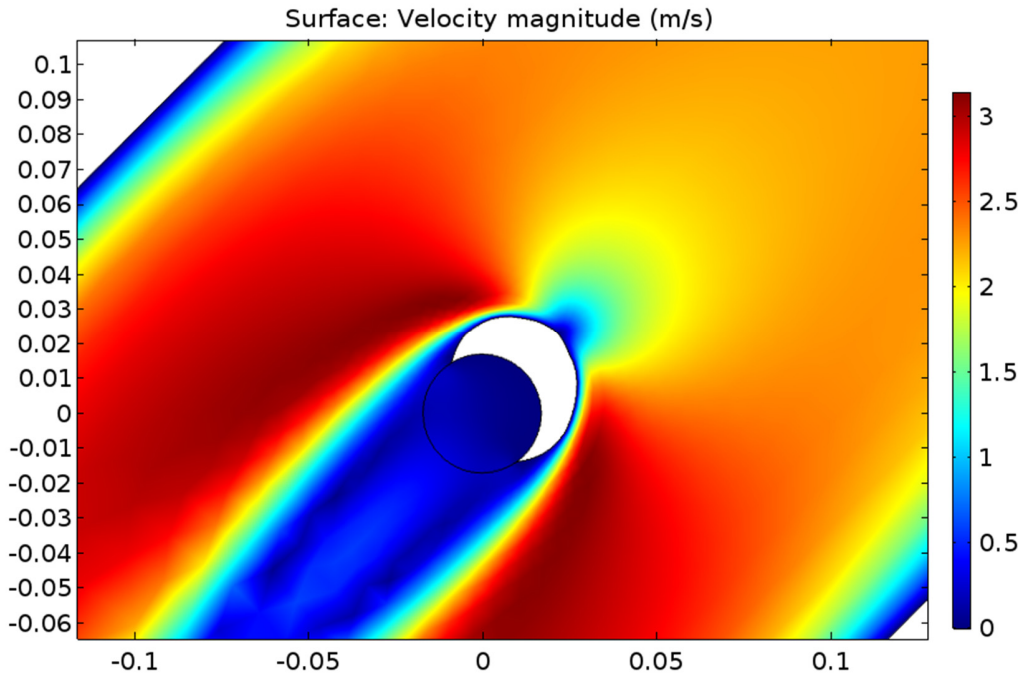

Figure 6-13: Rime accreted after 40 minutes of accretion with electric filed E = -5 kV/cm

After rime accretion, a thin preheated aluminum cutter was used to separate the ice sample from both sides. After that, heat the conductor a little bit to reduce the ice adhesion force and then remove the ice sample from the conductor as shown in Figure 6-14.


Figure 6-14: Ice sample removed from conductor

Figure 6-15 shows six cases which were considered to make a comparison of ice shapes between experimental results and simulations when the wind velocity V = 2 m/s, water droplet diameter D = 38 μm, and LWC = 2.1 g/m^3. By comparison of the ice shapes, it can be observed that the ice shapes obtained from experiments and simulations are in agreement when the electric field is no stronger than -20 kV/cm. However, when the electric field strength increases further, the measured ice shape is smaller than that of the simulation. This is due to the presence of corona wind. As the conductor surface is roughened by icing, when the applied voltage is beyond its corona onset voltage, corona wind is introduced. The corona wind tends to repel the water droplets away from the conductor, change their trajectories, and thus reduce the collision efficiency. It should be noted that in the simulations, the maximum contact angle increases with an increase of electric field. This is fairly expected as the water droplets are polarized when they are approaching the energized conductor and this polarization force attracts the water droplets to the conductor. Because the rim of the rime is easily to be destroyed when removed from the conductor, this increasing maximum contact angle phenomenon may be difficult to tell from the experimental ice shapes shown in Figure 6-15. However, this phenomenon was actually observed in the experiments.

(a) E = 0 kV/cm (b) E = -5 kV/cm

(c) E = -10 kV/cm

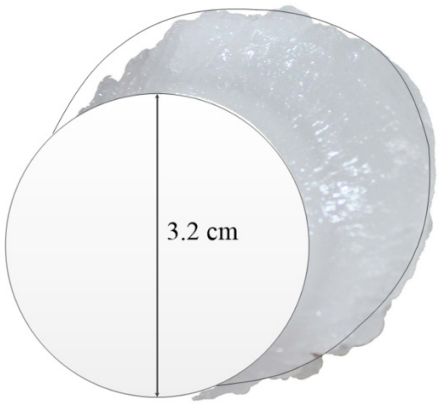

(d) E = -15 kV/cm

(e) E = -20 kV/cm

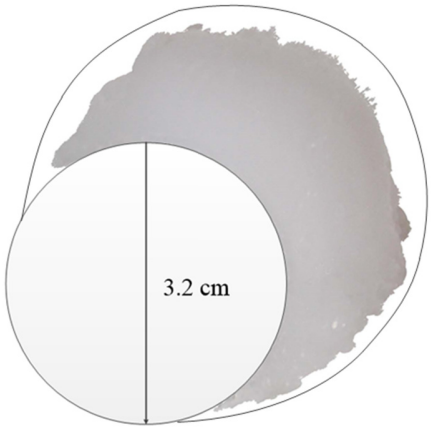

(f) E = -25 kV/cm

Figure 6-15: Comparison of ice shape, V = 2 m/s, and D = 38 μm, LWC = 2.1 g/m^3

The measured and simulated ice weights are plotted in Figure 6-16. When the electric field is low, the difference between experiments and simulation is small. With the electric field increases, the corona wind is generated. As the corona wind is not considered in the simulation, the difference increases.

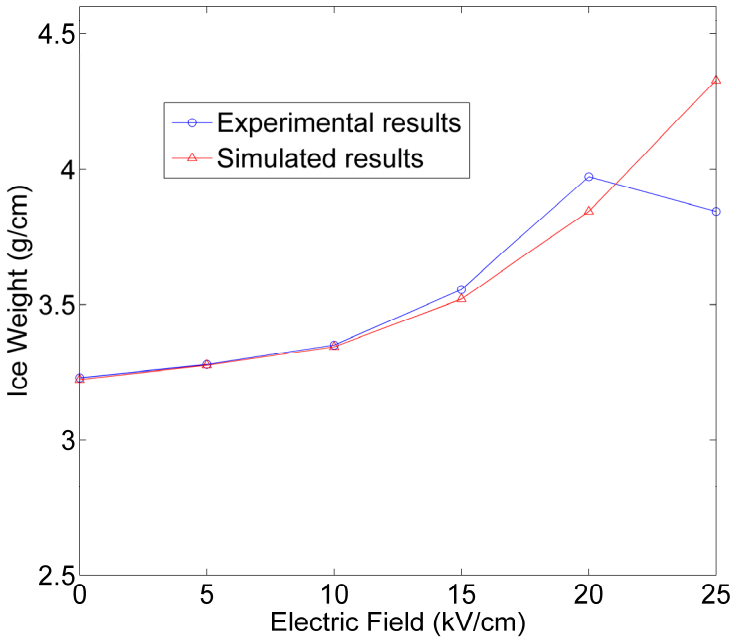

Figure 6-16: Comparison of ice weight

6.2.2 The influence of wind velocity

Figure 6-17: E = -20 kV/cm, V = 4 m/s, and D = 38 μm, LWC = 1.05 g/m^3

Figure 6.17 shows the experimental and simulated ice shapes when the wind velocity is 4 m/s. Compared to Figure 6-15e, it can be seen that the wind velocity increases the ice shape. The wind velocity has significant influence on ice accretion. As the water droplet are moving with wind when they

are far away from the energized conductor, higher fluid velocity means higher inertia of the water droplets, leading to a higher collision efficiency. Moreover, the wind velocity influences rime density. Obviously, a faster airflow increases the particle velocity which then has a higher impact speed. Thus, the Macklin's parameter R which is introduced by (6.22) also increases. With the increasing Macklin's parameter R, the ice density increases accordingly.

6.2.3 The influence of water droplet diameter

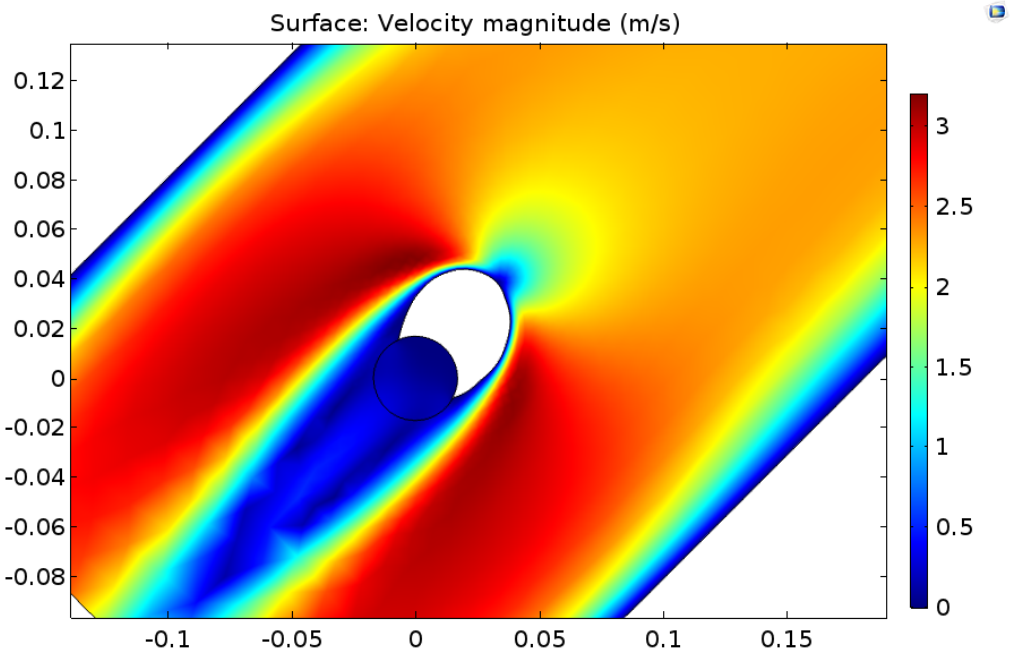

Figure 6-18: Rime accreted after 40 minutes of accretion, E = -10 kV/cm, V = 2 m/s, and D = 59 μm, LWC = 2.1 g/m^3

Figure 6.18 shows the rime accreted after 40 minutes of accretion when the electric field E = -10 kV/cm, wind velocity V = 2 m/s, water droplet diameter D = 59 μm, and LWC = 2.1 g/m^3. Figure 6-19 shows the experimental and simulated ice shapes. It is clear to see that the increasing water droplet diameter increases the ice shape. When the water droplet is small, its trajectory is more streamlined than it is the case for larger water droplet. Like the effect of wind velocity, a bigger water droplet leads to a higher inertia which tends to increase the collision efficiency.

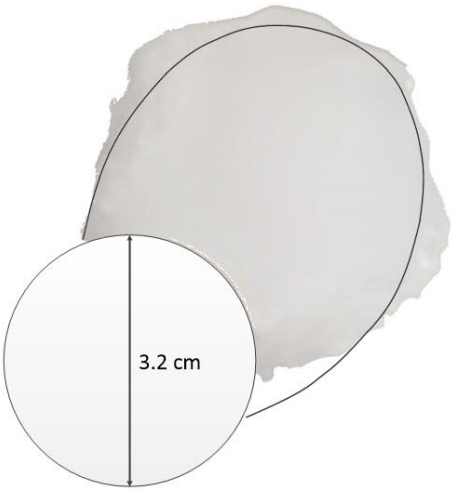

Figure 6-19: Comparison of ice shape, E = -10 kV/cm, V = 2 m/s, and D = 59 μm, LWC = 2.1 g/m^3

6.3 Conclusion

In this chapter, an icing model is provided, including the effect of electric field. After that, the simulated results were compared with experimental ones. When the electric field was low, the simulated values were consistent with the experimental results. However, when the electric field increased further, the difference became significant. Furthermore, both the wind velocity and the diameter of water droplet had positive correlations with ice weight.

CHAPTER 7

CONCLUSIONS AND RECOMMENDATIONS

CHAPTER 7

CONCLUSIONS AND RECOMMENDATIONS

7.1 Conclusions

To investigate the effect of electric field and corona discharge on ice accreted on high-voltage conductor, experiments were carried out in a climate room at CIGELE. Numerical simulation was also performance to simulate the rime accretion process. The following conclusions can be drawn from this study.

1) Under both rime and glaze ice conditions, the weight of ice accreted increases with electric field strength up to 20 kV_{rms}/cm and then decreases as it is increased further. Under non energized conditions and for a precipitation rate of 15 mm/h, about half of the total weight of glaze ice may be caused by icicle accretion. Under energized conditions, the weight percentage of icicles decreases with the conductor surface electric field. When the electric field is higher than 20 kV_{rms}/cm, the weight percentage of icicles is lowered to 14%.

2) When the precipitation rate is at a value close to ice accretion transition between rime and glaze, the icicles grow very slowly and the icicle spacing becomes independent of the conductor surface electric field. When the precipitation rate is sufficient, icicle spacing decreases as the electric field at the surface of the conductor is increased.

3) Under the energized conditions, there is an angle between adjacent icicles accreted on the conductor. The repulsion of the pendant drop at the icicle tip results in an increasing deviation angle as the electric field at the surface of the conductor is increased. When the electric field is higher than 20 kV_{rms}/cm, the pendant drop may split and lead to the formation of icicle branches.

4) The fundamental component contributes most of the corona loss. The contribution of other harmonic components on corona loss can be neglected, except for the significant harmonic component which is already contained in the applied voltage.

5) The weather has the same influence on corona loss and leakage conductance. The corona loss and the leakage conductance are higher under glaze icing condition and lower under rime condition when the conductor surface electric field is the same.

6) The capacitance of conductor increases during the ice accretion. After 40 minutes of rime accretion, the capacitance of the energized conductor is higher if the applied electric field during icing is stronger. However, with presence of the icicles, the capacitance under glaze ice accretion is complex.

7) A method to determine whether the conductor is running below or above its corona onset voltage is put forward. If the average power factor of the 3rd harmonics is far less than 0.50, the conductor is running below its corona onset voltage. Otherwise, if the average power factor of the 3rd harmonics is higher than 0.50, then, it can be expected that the conductor is operating above its corona onset voltage.

8) The finite element method is used to simulate the rime accretion on an energized conductor. It is found that when the electric field is no higher than 20 kV_{rms}/cm, the simulation results are consistent with the experimental results. With the electric field increases further, the difference between them is considerable due to the corona wind.

9) The wind velocity and water droplet diameter have significant influences on icing. Both a higher wind velocity and a bigger water droplet diameter increase the collision efficiency and therefore, increase the ice weight.

7.2 Recommendations

Further research on the modelling and experimental investigation of the effects of electric field and corona discharge on ice accreted on high voltage conductor should consider some of the following aspects.

1) The partial discharges of icicles can influence the onset voltage of the ice conductor. Thus, it would be valuable to study the partial discharge of an individual icicle in the further.

2) Presently, most of energy is transmitted by AC power transmission line. Therefore, it would be significant to simulate the ice accretion under AC condition. Under the constant DC condition, if the voltage is constant, the electric force imposed on a given water droplet only depends on the ice shape and its position with the ice. However, under AC condition, the electric force is also changing with time.

3) The present study only simulated the rime accretion. However, as the glaze ice is more dangerous to the power transmission lines, it will be interesting to simulate the glaze ice accretion on the energized conductor. With the formation of icicles or the inclined orientation of particle flux and transmission line. However, this would require significant computational resources.

4) The present simulation assumes that there is no corona wind generated. This assumption apparently fails when the applied voltage is beyond its corona onset voltage. Therefore, extending the present ice accretion model to take into account the corona wind would be of significance to simulate the rime accretion process accurately.

REFERENCES

[1]. M. Farzaneh, Atmospheric Icing of Power Networks, Springer, 2008.

[2]. G. Foots, Ice and Snow Accretion on Structures, Research Studies Press LTD, 1996.

[3]. S. C. Colbeck, and S. F. Ackley, "Mechanisms for ice bonding in wet snow accretions on power lines", Proceedings of the 1st International Workshop on Atmospheric Icing - IWAIS 1982, pp. 25-30, 1982.

[4]. H.N. Scherer and G.S. Vassell, "Transmission of electric power at ultra-high voltages: Current status and future prospects", Proceedings of the IEEE , Vol. 73, No. 8, pp. 1252-1278, 1985.

[5]. M. Candas and O. Meric, "The Application of Ultra High Voltage in the World", Journal of Power and Energy Engineering, Vol. 3, pp. 453-457, 2015.

[6]. M. Farzaneh, S. Farokhi, and W. A. Chisholm, Electrical Design of Overhead Power Transmission Lines, New York: McGraw-Hill, 2012.

[7]. G. W. Juette and L. E. Zaffanella, "Radio Noise, Audible Noise, and Corona Loss of EHV and UHV Transmission Lines Under Rain: Predetermination Based on Cage Tests", IEEE Trans. Power App. Syst., Vol. 89, No. 6, pp. 1168-1178, 1970.

[8]. H. H. Newell, T. W. Liao, and F. W. Warburton, "Corona and RI Caused by Particles On or Near EHV Conductors: II-Foul Weather", IEEE Trans. Power App. Syst., Vol. 87, No. 4, pp. 911-927, 1968.

[9]. K. Jones, Ice Storms in the St. Lawrence Valley Region Cold Regions, ERDC/CRREL TR-03-110, 130 pp., 2003.

[10]. Ministry of Civil Affairs, 2008: Report on the impact of the recent ice storm and the disaster relief (in Chinese). Ministry of Civil Affairs of the People's Republic of China.

[11]. J. G. Anderson, M. Baretsky, and D. D. Maccarthy, "Corona-loss characteristics of EHV transmission lines based on project EHV research", IEEE Trans. Power App. Syst., Vol. 85, No. 12, pp. 1196-1212, 1966.

[12]. M. Farzaneh, "Ice accretions on high-voltage conductors and insulators and related phenomena", Philosophical Trans. Royal Society of London A: Mathematical, Phys. Eng. Sc., Vol. 358, No. 1776, pp. 2971-3005, 2000.

[13]. C. F. Harding, "Corona Losses Between Wires at High Voltages", AIEE Trans., Vol. 31, No. 1, pp. 1035-1049, 1924.

[14]. M. Farzaneh, J. Kiernicki, “Flashover Performance of IEEE Standard Insulators under Ice Conditions”, IEEE Trans. Power Del., Vol. 12, No. 4, pp. 1602-1613, 1997.

[15]. L. Boulet, L. Cahill, and B. J. Jakubczyk, “Alternating Current Corona in Foul Weather II-Below Freezing Point”, IEEE Trans. Power App. Syst., Vol. 85, No. 6, pp. 649-656, 1966.

[16]. G. W. Juette, and L. E. Zaffanella, “Radio Noise, Audible Noise, and Corona Loss of EHV and UHV Transmission Lines Under Rain: Predetermination Based on Cage Tests”, IEEE Trans. Power App. Syst., Vol. 89, No. 6, pp. 1168-1178, 1970.

[17]. F. C. Lv, S. H. You and Y. P. Liu, “AC Conductors’ Corona-Loss Calculation and Analysis in Corona Cage”, IEEE Trans. Power Del., Vol. 27, No. 2, pp. 877-885, 2012.

[18]. L. Boulet, and B. J. Jakubczyk, “A-C Corona in Foul Weather I-Above Freezing Point”, IEEE Trans. Power App. Syst., Vol. 83, No. 5, pp. 508-512, 1964.

[19]. F. C. Lv, S. H. You and Y. P. Liu, and Q. F., Wan, “Analysis on Corona Loss Measurement of Ultra High Voltage AC Single Circuit Test Line in Rain and Snow Weather Conditions”, High Voltage Eng., Vol. 37, No. 9, pp. 2089-2095, 2011, (in Chinese).

[20]. O. Nigol, and J. G. Cassan, “Corona Loss Research at Ontario Hydro Coldwater Project”, IEEE Trans. Power App. Syst., Vol., 80, No. 3, pp. 304-312, 1961.

[21]. J. S. Carroll, and B. Cozzens, “Corona loss measurements for the design of transmission lines to operate at voltages between 220 kV and 330 kV”, AIEE Trans., Vol. 52, No. 1, pp. 55-62, 1933.

[22]. V. L. Chartier, D. F. Shankle, and N. Kolcio, “The Apple Grove 750-kV Project: Statistical Analysis of Radio Influence and Corona-Loss Performance of Conductors at 775 kV”, IEEE Trans. Power App. Syst., Vol. 89, No. 5, pp. 867-881, 1970.

[23]. R. Wilkins, “Corona loss tests on the 202-mile 60-cycle 220-kV Pit-Vaca transmission line of the Pacific gas and electric company”, AIEE Trans., Vol. 43, No. 12, pp. 1109-1116, 1924.

[24]. N. Giao Trinh, P. S. Maruvada, J. Flamand, and J. R. Valotaire, “A Study of the Corona Performance of Hydro-Quebec's 735-kV Lines”, IEEE Trans. Power App. Syst., Vol. 101, No. 3, pp. 681-690, 1982.

[25]. P. Fu, Modelling and simulation of the ice accretion process on fixed or rotating cylindrical objects by the Boundary Element Method, PhD thesis, Collection des mémoires et thèses de l'Université duQuébec à Chicoutimi. http://theses.uqac.ca/these_18326611.html.2004.

[26]. B. W. Smith, Communication structures, Thomas Telford Publishing, 2007.

[27]. ES ISO 12494:2012, Atmospheric icing of structures, Ethiopian Standards Agency, 2012.

[28]. COST 727, Atmospheric Icing on Structures: Measurements and data collection on icing, State of the Art, Publication of Meteoswiss, 2006.

[29]. P. Admirat, Y. Sakamoto, "Calibration of a wet snow model on real cases in Japan and France", Proceedings of the 4th International Workshop on Atmospheric Icing of Structures (IWAIS 1988), Paris, France, 1988.

[30]. S. M. Fikke, "Modern meteorology and atmospheric icing", Proceedings of the 11th International Workshop on Atmospheric Icing of Structures (IWAIS 2005), Montreal, Canada, 2005.

[31]. B. E. K. Nygaard, J. E. Kristjánsson, and L. Makkonen, "Prediction of In-Cloud Icing Conditions at Ground Level Using the WRF Model". Journal of Applied Meteorology and Climatology, Vol. 50, NO. 12., pp. 2445-2459, 2011.

[32]. C. Shea and B. Jamieson, "The role of moisture in surface hoar growth", The Journal of Canada's Avalanche Community, Vol. 88, Issue Spring, pp. 61-64, 2009.

[33]. K. Lahti, M. Lahtinen, and K. Nousiainen, "Transmission Line Corona Losses under Hoar Frost Conditions", IEEE Trans. Power Del., Vol. 12, No. 2, pp. 928-933, 1997.

[34]. E. Kuffel, W.S. Zaengl, and J. Kuffel, High Voltage Engineering, Second edition, Pergamon Press, 2000.

[35]. John D. Ryder, Donald. G. Fink, Engineers & Electrons: A Century of Electrical Progress, The Institute of Electrical and Electronics Engineers, Inc., New York, 1984.

[36]. R. D. Begamudre, Extra High Voltage AC Transmission, Third edition, New Age International Publishers, 2006.

[37]. M. E. El-Hawary, Electrical Power System: Design and Analysis, IEEE Press, 1995.

[38]. C. F. Harding, "Corona Losses Between Wires at Extra High Voltages- II", Trans. A. I. E. E., vol. XLIII, pp. 1182-1196, 1924.

[39]. P. S. Maruvada, Corona Performance of High-Voltage Transmission Lines. Research Studies Press: England, pp. 91-96.

[40]. L. Hegy, and G. W. Dunlap, "Corona Loss Vs. Atmospheric Conditions", Electr. Eng., Vol. 53, No. 2, pp. 272-273, 1934.

[41]. X. L. Jiang, J. Chen, L. C. Shu, J. L. Hu, Z.J. Zhang, and S. J. Wang, “Studying Corona Onset Characteristics after Rime Ice Accumulation on Energized Stranded Conductors”, IEEE Trans. Dielectr. Electr. Insul., Vol. 20, No. 5, pp. 1799-1807, 2013.

[42]. L. Chen, J.M.K. MacAlpine, X. M. Bian, L. M. Wang, and Z. C. Guan, “Comparison of methods for determining corona inception voltages of transmission line conductors”, Journal of Electrostatics, Vol. 71, No. 3, pp. 269-275, 2013.

[43]. F. W. Peek, “The law of corona and the dielectric strength of air - IV the mechanism of corona formation and loss”, AIEE Trans., Vol. 46, No. 12, pp. 1009-1024, 1927.

[44]. M. Abdel-Salam and D. Wiitanen, “Calculation of Corona Onset Voltage for Duct-Type Precipitators”, IEEE Transactions on Industry Application, Vol. 29, No. 2, 1993.

[45]. Q. Hu, L. Shu, X. Jiang, C. Sun, S. Zhang, and Y. Shang, “Effects of air pressure and humidity on the corona onset voltage of bundle conductors”, IET Generation, Transmission & Distribution, IET Gener. Transm. Distrib., Vol. 5, No. 6, pp. 621–629, 2011.

[46]. K. Yamazaki and R. G. Olsen, “Application of a Corona Onset Criterion to Calculation of Corona Onset Voltage of Stranded Conductors”, IEEE Trans. Dielectr. Electr. Insul., Vol. 11, No. 4, pp. 675-680, 2004.

[47]. M. M. Xu, Z. Y. Tan, and K. J. Li, “Modified Peek Formula for Calculating Positive DC Corona Inception Electric Field under Variable Humidity”, IEEE Trans. Dielectr. Electr. Insul., Vol. 19, No. 4, pp. 1377-1382, 2012.

[48]. F. W. Peek, Dielectric Phenomena in High Voltage Engineering, McGraw-Hill Press: New York, 1920.

[49]. K. S. Iyer, and K. P. P. Pillai, “Analysis of irregularity factor of stranded conductors”, Proc. IEE, Vol. 115, pp. 364-367, 1968.

[50]. M. M. El-Bahy, M. Abouelsaad, N. Abdel-Gawad, and M. Badawi, “Onset voltage of negative corona on stranded conductors”, J. Phys. D: Appl. Phys., Vol. 40, 3094–3101, 2007.

[51]. M. Khalifa and M. Abdel-Salam, “Calculating the surface fields of conductors in corona”, Proceedings of the Institution of Electrical Engineers, Vol. 120, No. 12, pp.1574-1575, 1973.

[52]. J. B. Whitehead, “The electric strength of air, II,” AIEE Trans., Vol. 28, pp. 1857-1887, 1911.

[53]. J. J. Clade and C. H. Gary, “Predetermination of Corona Losses Under Rain: Influence of Rain Intensity and Utilization of a Universal Chart”, IEEE Trans. Power App. Syst., Vol. 89, No. 6, pp. 1179-1185, 1970.

[54]. F. W. Peek, “The law of corona and the dielectric strength of air - II”, Trans. A. I. E. E., vol. 31, no. 1, pp. 1051-1092, 1912.

[55]. W. X. Liu, Q. J. Zhao, H. Zhang, X. Li, L. Kang, and Y. T. Zhao, “Study on the Corona Loss Estimate under the 1000 kV UHVAC Transmission line”, Electric Power Construction, Vol. 32, No. 10, pp. 27-29, 2011, (in Chinese).

[56]. G. Hartmann, “Theoretical Evaluation of Peek’s Law”, IEEE Transactions on Industry Application, Vol. IA-20, No. 6, pp. 1647-1651, 1984.

[57]. M. Farzaneh and I. Fofana, “Experimental study and analysis of corona discharge parameters on an ice surface”, J. Phys. D: Appl. Phys., Vol. 37, pp. 721–729, 2004.

[58]. P. Ortéga, P. Domens, J. Dupuy, A. Gibert, F. Rühling, and F. Heilbronner, “Long air gap discharge under non-standard positive impulses voltages”, 7th Int. Symp. on High Voltage Engineering, Dresden, Germany, pp. 105–108, 1991.

[59]. O. Naef, R. L. Tremaine, and A. R. Jones, “Techniques of Corona Loss Measurement and Analysis”, Electrical Engineering, Vol. 70, No. 5, pp. 423-423, 1951.

[60]. O. Nigol and J. G. Cassan, “Corona Loss Research at Ontario Hydro Coldwater Project”, IEEE Transactions on Power Apparatus and Systems, Vol. 80, No. 3, pp. 304-312, 1961.

[61]. I. Fofana, M. Farzaneh, H. Hemmatjou, and C. Volat, “Study of Discharge in Air from the Tip of an Icicle”, IEEE Trans. Dielectr. Electr. Insul., Vol. 15, No. 3, pp. 730-740, 2008.

[62]. L. N. Li, S. J. Lee, W. J. Kim, and D. J. Kim, “An empirical model for ionic wind generation by a needle-to-cylinder dc corona discharge”, Journal of Electrostatics, Vol. 73, No. 3, pp. 125-130, 2015.

[63]. G. C. Sibilant, N. M. Ljumba, and A. C. Britten, “Studies of DC Conductor Corona in a Small Corona Cage”, IEEE Africon. 6th Africon Conference in Africa, pp. 661-664, 2002.

[64]. Q. Hu, T. Li, L. C. Shu, X. L. Jiang, and B. S. Luo, “Dynamic characteristics of the corona discharge during the energised icing process of conductors”, IET Gener. Transm. Distrib., Vol. 7, No. 4, pp. 366–373, 2013.

[65]. J. Chen, X. L. Jiang, L. C. Shu, J. L. Hu, Q. Hu, and Y. X. Wang, “Study on the Influence of Charged Glaze on the Corona Onset Voltage of Bundle conductor”, IEEE Trans. Dielectr. Electr. Insul., Vol. 21, No. 4, pp. 1592-1599, 2014.

[66]. R. G. Urban, H. C. Reader, and J. P. Holtzhausen, “Small Corona Cage for Wideband HVAC Radio Noise Studies: Rationale and Critical Design”, IEEE Trans. Power Del., Vol. 23, No. 2, pp. 1150-1157, 2008.

[67]. X. M. Bian, D. M. Yu, X. B. Meng, M. MacAlpine, L. M. Wang, and Z. C. Guan, “Corona-generated Space Charge Effects on Electric Field Distribution for an Indoor Corona Cage and a Monopolar Test Line”, IEEE Trans. Dielectr. Electr. Insul., Vol. 18, No. 5, pp. 1767-1778, 2011.

[68]. X. M. Bian, L. M. Wang, Y. P. Liu, Y. J. Yang, and Z. C. Guan, “High Altitude Effect on Corona Inception Voltages of DC Power Transmission Conductors Based on the Mobile Corona Cage”, IEEE Trans. Power Del., Vol. 28, No. 3, pp. 1971-1973, 2013.

[69]. Y. P. Liu, S. H. You, and F. C. Lv, “500-kV EHV Bundle Conductors’ Corona Onset Voltage Calculation and Analysis in Corona Cage at Different Altitudes”, IEEE Trans. Power Del., Vol. 27, No. 4, pp. 2090-2097, 2012.

[70]. Y. P. Liu, L. Zhu, F. C. Lv, X. J. Xie, and S. H. You, “Analysis of the Positive Corona Onset Characteristic of the Bundle Conductors in the UHV Corona Cage”, Transactions of China Electrotechnical Society, Vol. 28. No. 1, pp. 73-79, 2013, (in Chinese).

[71]. Min-wen Peng, Wei-ke Li, and Hua Cui, “Structural Design of Corona Cage of UHV DC Testing Site”, Electric Power Construction, Vol. 29, No. 1, pp. 4-5, 2008.

[72]. J. J. Laforest, C. B. Lindh, and D. D. MacCarthy, “Radio Noise and Corona Loss Results from Project EHV”, IEEE Trans. Power App. Syst., Vol. 82, No. 68, pp. 735-750, 1963.

[73]. Z. Liu, Ultra-High Voltage AC/DC Grids, Academic Press, 2014.

[74]. F. J. Sollerkvist, A. Maxwell, K. Rouden, and T. M. Ohnstad, “Evaluation, Verification and Operational Supervision of Corona Losses in Sweden”, IEEE Trans. Power Del., Vol. 22, No. 2, pp. 1210-1217, 2007.

[75]. E. A. Yahaya, T. Jacob, M. Nwohu, and A. Abubakar, “Power loss due to Corona on High Voltage Transmission Lines”, IOSR Journal of Electrical and Electronics Engineering (IOSR-JEEE), Vol. 8, No. 3, pp. 14-19, 2013.

[76]. Y. P. Liu, S. H. You, Q. F. Wan, and W. J. Chen, “Design and Realization of AC UHV Corona Loss Monitoring System”, High Voltage Engineering, Vol. 34, No. 9, pp. 1797-1801, 2008.

[77]. M. S. Virk, M. Y. Mustafa, and Q. Hamdan, “Atmospheric Ice Accretion Measurement Techniques”, Int. Jnl. of Multiphysics, Vol. 5, No. 3, 2011.

[78]. J. N. Laflamme, G. Periard, “The climate of freezing rain over the province of Quebec in Canada: a preliminary analysis”, Atmospheric Research, Vol. 46, No. 1, pp. 99-111, 1998.

[79]. N. D. Mulherin, “Atmospheric icing and communication tower failure in the United States”, Cold Regions Science and Technology, Vol. 27, No. 2, pp. 91-104, 1998.

[80]. B. Q. Li, Discontinuous Finite Elements in Fluid Dynamics and Heat Transfer, Springer, 2006.

[81]. P. McComber, and G. Touzot, “Calculation of the Impingement of Cloud Droplets in a Cylinder by the Finite-Element Method”, Journal of the Atmospheric Sciences, Vol. 38, May 1981.

[82]. L. Makkonen, “Heat transfer and icing of a rough cylinder”, Cold Regions Science and Technology, Vol. 10, pp. 105-116, 1984.

[83]. L. Makkonen, “Atmospheric Accretion of Ice Loads”, Department of Meteorology University of Helsinki, Report No. 25,1985.

[84]. L. Makkonen, “Modelling of Ice Accretion on Wires”, Journal of Climate and Applied Meteorology, Vol. 23, No. 6, pp. 929-939,1984.

[85]. L. Makkonen, “Modelling Power Line Icing in Freezing Precipitation”, Proceedings of the 7th International Workshop on Atmospheric Icing of Structures, Chicoutimi, QC, pp. 195-200,1996.

[86]. K. Szilder, E. P. Lozowski, “A new method of modelling ice accretion on objects of complex geometry”. Int J Offshore Polar Engin., Vol. 5, pp. 37-42. 1995

[87]. K. Szilder, E. P. Lozowski, “Three-dimensional modelling of ice accretion microstructure”. In:Proc 7th International Workshop on Atmospheric Icing of Structures: pp. 60-63, 1996.

[88]. K. F. Jones, “A Simple Model for Freezing Rain Ice Loads”, Atmospheric Research, Vol. 46, No. 1-2, pp. 87-97,1998.

[89]. M. M. Oleskiw, E. P. Lozowski, “The design and testing of a Lagrangian computer model for simulating time-dependent rime icing on two-dimensional structures”. In: Proc First International Workshop on Atmospheric Icing of Structures, pp. 59-66, 1983.

[90]. C. N. Aliaga, M. S. Aube, G. S. Baruzzi, W. G. Habashi, and S. Nadarajah, “A third-generation in-flighticing code: FENSAP-ICE-Unsteady”, SAE 2007 Aircraft & Engine Icing International Conference, Seville, Paper 2007-01-3339, 2007.

[91]. T. Wagner, U. PEil, and C. Borri, “Numerical investigation of conductor bundle icing”, in EACWE 5. 2009: Florence, Italy.

[92]. Y.Teisseyre and M. Farzaneh, “On the Mechanisms of The Ice Accretion On H.V. Conductors”, Cold Regions Science and Technology, 18 (1990) 1-8.

[93]. Farzaneh, M, and Laforte JL, “Effect of Voltage Polarity on Icicles Grown on Line Insulators”, Int Offshore and Polar Eng (IJOPE), Vol 2, No. 4, pp. 228-233, 1992.

[94]. Farzaneh, M, J.L. Laforte, “Ice Accretion on Conductors Energized by AC or DC: A Laboratory Investigation of Ice Treeing”, International Journal of Offshore and Polar Engineering, Vol.4, No.1, 1994.

[95]. P. Sattari, G. S. P. Castle, and K. Adamiak, “Numerical Simulation of Trichel Pulses in a Negative Corona Discharge in Air”, IEEE Trans. Ind. Appl., vol. 47, no. 4, pp. 1935–1943, 2011.

[96]. GB/T16434-1996, Environmental Pollution Classification and External Insulation Selection for High Voltage Transmission Line, Power Plant and Substation, 1996, in Chinese.

[97]. Q. Li, S. M. Rowland, and R. Shuttleworth, “Calculating the Surface Potential Gradient of Overhead Line Conductors”, IEEE Trans. Power Del., Vol. 30, No. 1, pp. 43-52, 2015.

[98]. C. T. O’Konski, and H. C. Thacher, “The Distortion of Aerosol Droplets by an Electric Field”, J. Phys. Chem., Vol.57, No. 9, pp 955-958, 1953.

[99]. R. Grisso, P. Hipkins, and S. Askew, Nozzles: Selection and Sizing, Virginia Cooperative Extension, Publication 442-032, 2013.

[100]. N. Dayan, and I. Gallily, “On the Collection Efficiency of Water Droplets under the influence of Electric Forces I: Experimental, Charge-Multipole Effects”, J. Atmos. Sci., Vol. 32, pp. 1419-1429, 1975.

[101]. Q. Z. Ye, J. Li, and H. Y. Yang, “A displaced dipole model for spheres in a non-uniform field”, J. Electrostat., Vol. 56, No. 1, pp. 1-18, 2002.

[102]. N. E. L. Haugen and S. Kragset, “Particle Impaction on a Cylinder in a Crossflow as Function of Stokes and Reynolds Numbers”, J. Fluid Mech., Vol. 661, pp. 239-261, 2010.

[103]. P. Wang, and H. R. Pruppacher, “Acceleration to Terminal Velocity of Cloud and Raindrops”, J. Appl. Meteor., Vol. 16, No. 3, pp. 275-280, 1977.

[104]. L. Makkonen, and Y. Fujii, “Spacing of icicles”, Cold Regions Science and Technology, Vol. 21, pp. 317-322, 1993.

[105]. A. W. Neumann, R. David, and Y. Zuo, Applied Surface Thermodynamics, 2ed, CRC Press, Taylor & Francis Group, New York, 2010.

[106]. Y. Deng, Z. Jia, and H. Jiang, "Analysis of Icicle Growth Process of Composite Insulator under Energized Condition and Its Impact Factors", IEEE Trans. Dielectr. Electr. Insul., Vol. 22, No. 3, pp. 1613–1622, 2015.

[107]. F. P. Incropera, D. P. DeWitt, T. L. Bergman, and A. S. Lavine, Fundamentals of Heat and Mass Transfer, 6th Ed., Hoboken, NJ, John Wiley & Sons, 2007.

[108]. N. Maeno, L. Makkonen, and T. Takahashi, "Bent icicles and spikes", Annals of Glaciology, Vol. 19, pp. 138-140, 1994.

[109]. L. Makkonen, "A Model of Icicle Growth", J. Glaciology, Vol. 34, No. 116, pp. 64-70, 1988.

[110]. L. Shu, Z. Yang, and X. Jiang, "A model for calculating deviation angle of icicle buildup on insulators and its experimental validation", Euro. Trans. Electr. Power, Vol. 23, No. 3, pp. 315-329, 2013.

[111]. M. Bowles, "State Electricity Profiles 2008", US Energy Information Administration, DOE/EIA 0348(01)/2, March 2010.

[112]. Q. Geng, Y. Lu, and P. Zhang, "Comparative Analysis of Operation Losses of UHV AC and EHV AC Transmission Systems", Power System Protection and Control, Vol. 44, No. 16, pp. 72-77, 2016.

[113]. GB 1179-83, Aluminium Stranded Conductors and Aluminium Conductors Steel-reinforced, 1983, in Chinese.

[114]. A. H. Foley, and F. Olsen, "Project EHV-preliminary corona investigations: the effect of harmonics on corona losses," Power App. Syst., Part III, Trans. A. I. E. E., vol. 79, no. 3, pp. 310-315, 1960.

[115]. A. McEachern, "On Negative Power and Negative Power Factor in Alternating Current Power Systems," Available: http://powerstandards.com/Shymanski/draft.pdf.

[116]. B. R. Munson, D. F. Young, T. H. Okiishi, and W. W. Huebsch, Fundamentals of Fluid Mechanics, Sixth Edition, USA, 2009.

[117]. J. C. Tannchill, D. A. Anderson, and R. H. Pletcher, Computational Fluid Mechanics and Heat Transfer, Second Edition, Taylor & Francis, United Kingdom, 1997.

[118]. D. J. Tritton, Physical Fluid Dynamics, Second Edition, Oxford Science Publications, United Kingdom, 1988.

[119]. M. S. Virk, “Atmospheric Ice Accretion on Non-Rotating Circular Cylinder”, Journal of Computational Multiphase Flows, Vol. 3, No. 4, pp. 197-205, 2011.

[120]. C. Leng, J. E. Roberts, G. Zeng, Y. Zhang, and Y. Liu, “Effects of temperature, pH, and ionic strength on the Henry’s law constant of trimethylamine”, Geophys. Res. Lett., Vol. 42, pp. 3569-3575, 2015.

[121]. R. A. Black, and J. Hallett, “Rain rate and water content in hurricanes compared with summer rain in Miami, Florida”, J. Appl. Meteorol. Climatol., Vol. 51, pp. 2218-2235, 2012.

[122]. H. G. Norment, “Calculation of Water Drop Trajectories to and About Arbitrary Three-Dimensional Bodies in Potential Airflow”, NASA Report 3291.

[123]. J. D. Anderson, Fundamentals of Aerodynamics, McGraw-Hill, Fifth Edition, New York, USA, 2011.

[124]. G. Vijayakumari, Engineering Physics, Vikas Publishing House, Second Edition, India, 2009.

[125]. W. Licht, “The Movement of Aerosol Particles”, J. Soc. Cosmet. Chem., Vol. 23, pp. 657-678, 1972.

[126]. I. Langmuir and K. B. Blodgett, A mathematical investigation of water droplet trajectories, Collected Works of Irving Langmuir. Pergamon Press, 1946.

[127]. W. C. Macklin, “The density and structure of ice formed by accretion”, Quart. J. R. Met. SOC., Vol. 88, pp. 30-50, 1962.

[128]. M. Bain and J. F. Gayet, “Contribution to the modeling of the ice accretion process: Ice density variation with the impact surface angle”, Annals of Glaciology, Vol. 4, pp. 19-23, 1982.